MAGNONICS IN QUANTUM OPTICAL ARCHITECTURES

A Dissertation

by

JAYAKRISHNAN MUTTATHIL PRABHAKARAPADA NAIR

Submitted to the Graduate and Professional School of
Texas A&M University
in partial fulfillment of the requirements for the degree of

DOCTOR OF PHILOSOPHY

Chair of Committee,	Girish S. Agarwal
Committee Members,	M. Suhail Zubairy
	Aleksei M. Zheltikov
	Waruna Kulatilaka
Head of Department,	Grigory Rogachev

August 2023

Major Subject: Physics

ABSTRACT

The manipulation of light-matter interactions forms the bedrock of quantum optics and information processing. For many years, atoms in conjunction with quantum electrodynamics systems involving high-quality cavities offered a platform to realize strong photon-matter couplings. As a complementary paradigm to cavity-quantum electrodynamics (cavity-QED), waveguide-integrated atomic systems have also emerged as a strong candidate for observing many-body quantum phenomena. However, there exists no-single all-encompassing quantum system, capable of achieving all the requirements of a present-day quantum information processing system. Instead, modern quantum machines require various hybrid quantum systems with multitasking abilities, especially those involving solid-state systems. In this context, hybrid magnonic systems utilizing ferrimagnetic materials like Yttrium iron garnet (YIG) have gained much traction among the optics community, thanks to their high spin density and low damping rates. The collective motion of these spins is embodied in the form of quasiparticles named magnons, which strongly couple with cavity photons. This thesis is dedicated to the theoretical analyses of hybrid magnonic systems coupled with quantum optical elements at the interface between cavity and waveguide QED, particularly in the framework of non-Hermitian physics. More specifically, we studied the ramifications of anti-$\hat{P}\hat{T}$ symmetry in dissipatively coupled two-mode anharmonic systems, demonstrating, for instance, the generation of a bound state in continuum (BIC), which can be exploited for sensing perturbations, especially those of anharmonic nature. Dissipatively coupled systems also offer a significantly low threshold for observing bistability when compared to their coherently coupled counterparts. In the context of cavity magnonics, we illustrated the possibility of achieving dissipative coupling between magnons earmarked by the observation of level attraction. In addition, we also examined the quantum correlations and transfer of excitations between two macroscopic YIG samples placed inside a microwave cavity. In the strong pumping domain, wherein the Kerr-anharmonicities of the YIGs are significant, we predicted the emergence of multi-stability in the spin currents. This was verified by obtaining the shift in polaritonic peaks of the transmission to a weak probe. In the case

of a weak pump of the order of 1μW, we used a two-photon parametric drive to generate a BIC, which could enhance the efficiency in the transfer of excitation between two samples. Recently, our predictions of multistability and ultra-low threshold bistability were verified by experimental data. Experimental activity in the domain of cavity and waveguide-integrated magnonics has flourished of late and the rest of our theoretical proposals are likely to attain experimental implementation in the near future.

DEDICATION

To my parents, Radhika B. Nair, Prabhakarapada Nair and my dear sister Bhavyasree.

ACKNOWLEDGMENTS

This thesis is the culmination of a memorable five years of my life at Texas A&M University. The experience was nothing short of remarkable, filled with several challenges which helped me to become a better person and researcher. This journey could not have been possible without the relentless support of so many people. In particular, the doctoral advisor plays a quintessential role in shaping the career of a PhD student. I would like to begin by thanking Prof. Girish Agarwal for allowing me to work with him. His thoughts have always inspired me and I will forever be grateful for his unparalleled guidance and support. His immense grasp of quantum optics and insights to find connections between apparently unrelated problems have been motivating and they provided me with new perspectives and helped bridge the gaps in my understanding of the subject. His unwavering dedication towards research and diligent pursuit of a problem gave me a feel of the qualities of an exceptional researcher. Working with him, I realized that it is not just about obtaining results but also how one communicates them to the audience that makes a research output truly outstanding. For the majority of my PhD career, I was financially supported by the HEEP fellowship. I would like to express my sincere gratitude to Prof. Agarwal for always supporting me in my eligibility for the fellowship. I would also like to thank him for constantly providing feedback on my calculations, funding my travel to conferences, overseeing the progress towards my dissertation and guiding me in the right direction during the difficult phases.

I am grateful to Prof. M. Suhail Zubairy, Prof. Aleksei M. Zheltikov, and Prof. Waruna Kulatilaka for agreeing to be on my committee and evaluating this work. I am deeply thankful for their useful comments, and questions during my preliminary examination, and thesis defense and for being very supportive whenever I had a chance to interact with them. I would also like to express my gratitude to the Institute for Quantum Science and Engineering and the Department of Physics and Astronomy, Texas A&M University, for providing a wonderful environment for research. I would like to thank the staff, especially, Raechel E. Superville, Sherree Kessler and Emily Berger their constant support as departmental academic advisors. I would also like to thank

Yasa Rathnayaka for helping me set up the HEEP fellowship.

I am also thankful to all my teachers beginning with the exceptional professors from IISER Thiruvananthapuram during my undergraduate studies. In particular, I would like to thank Prof. Anil Shaji who introduced me to quantum optics and Prof. Sudheesh Chethil who advised me on my first scientific research. I would also like to thank all my teachers at Texas A&M, especially, Prof. M. Suhail Zubairy, for providing one of the most intriguing series of lectures on quantum optics. That was one of the most well-organized and thought-provoking courses I have taken at Texas A&M and remarkable for its theoretical rigour. I am truly thankful to Prof. Zubairy who always welcomed me to walk into his office whether it was a question on physics or a casual chat. In addition, I would like to thank Prof. Christopher Pope for two of the best electromagnetic theory courses.

Much of the research in this thesis was performed in collaboration with Dr. Debsuvra Mukhopadhyay. A special thanks to him who has been the soundboard for many of my questions over the past five years. I have learned a lot from the discussions with him and I look forward to our future collaborations. Moving to a new country and getting acclimatized to the environment was never easy. Debs was one of the people who made this transition easier for me. I will always cherish our lunch discussions. I would also like to thank Dr. Zhedong Zhnag, Jiaxuan Wang, Dr. Yusef Maleki and Jiru Liu who were always open to discussions. I am also thankful to all the IQSE members, especially Arash Azizi and Sahar Delfan who were always welcoming whenever I had a chance to interact with them.

Life in the US, especially during the first few years was difficult for me. I am deeply thankful for Nandhu who always had my back during difficult times. He helped me bring balance to my life and the time we were together in College Station were truly some of the best days during the past five years. I am also thankful to Aravind, Aswin, Rafeed, Stephin and Zoheb for making me feel at home. I also would like to extend my gratitude towards long-time friends Abhijit, Abu, Anand, Aromal and Chithran who have constantly supported me over the last decade. Particularly, I would like to thank Abhijit who turned up every week for a phone call which made a lot of difference.

Last but not the least, I would like to express my sincere gratitude towards my family, Acchan, Amma, Chechi, Vyshu and especially Sethu for always standing by my side in difficult phases of my life.

CONTRIBUTORS AND FUNDING SOURCES

Contributors

This work was supported by a dissertation committee consisting of Prof. Girish S. Agarwal (advisor and chair), Prof. M. Suhail Zubairy, and Prof. Aleksei Zheltikov of the Department of Physics and Astronomy, and Prof. Waruna Kulatilaka of the Department of Mechanical Engineering.

Chapter 9 in this dissertation is based primarily on independent research under the supervision of Prof. Girish S. Agarwal. The analyses and the results presented in Chapters 3-8 are based substantially on collaborative research conducted with Dr. Zhedong Zhang, Prof. M. O. Scully and Dr. Debsuvra Mukhopadhyay. This contribution has been duly acknowledged as a footnote at the beginning of each chapter.

Funding Sources

The research presented in this thesis was financially sponsored in part by the Herman F. Heep and Minnie Belle Heep Texas A&M University endowed fund. It was also supported in part by the Department of Physics and Astronomy, Texas A&M University, through Teaching Assistantship, and in part by the advisor's research grant, through Research Assistantship.

ACRONYMS

QED	Quantum electrodynamics
EP	Exceptional point
$\hat{PT}$	Parity-time
BIC	Bound state in continuum
VIC	Vacuum induced coherence
YIG	Yttrium iron garnet
DDI	Dipole-dipole interaction

TABLE OF CONTENTS

Page

ABSTRACT ii

DEDICATION iv

ACKNOWLEDGMENTS v

CONTRIBUTORS AND FUNDING SOURCES viii

ACRONYMS ix

TABLE OF CONTENTS x

LIST OF FIGURES xiii

1. INTRODUCTION 1

2. MAGNONICS 8

2.1 Spin waves in an ordered magnetic system 9
2.1.1 Holtein-Primakoff theory of spin waves 10
2.1.2 Magnon-magnon interactions 13
2.1.3 Dipole-dipole interactions 14
2.2 Cavity and waveguide magnonics 15
2.2.1 Some recent developments and motivation 16
2.2.2 Spin-spin interactions in a YIG 17
2.2.3 Magnon-photon interaction 19
2.3 Summary 21

3. CAVITY MEDIATED TRANSFER OF SPIN CURRENTS 23

3.1 Cavity-magnon system 24
3.2 Spin current in nonlinear magnon polaritons 26
3.3 Spectroscopic detection of nonlinear magnon polaritons 30
3.3.1 Nonlinearity of a single YIG as seen in probe transmission 31
3.3.2 Detection of multistability in spin current via probe transmission 34
3.4 Summary 39

4. QUANTUM AMPLIFICATION OF ENERGY-TRANSFER IN CAVITY MAGNONICS BY A PARAMETRIC DRIVE INDUCED LONG-LIVED MODE 41

4.1 Amplified spin currents 43
4.2 Parametric-drive-induced long-lived mode 49
4.3 Summary 51

5. ANTI-$\hat{PT}$ SYMMETRY IN MAGNONICS 53

5.1 Symmetry properties of two-mode non-Hermitian systems 54
5.2 Possible realizations of anti-$\hat{PT}$ symmetry 56
5.2.1 Anti-$\hat{PT}$ symmetry through dissipative coupling 58
5.3 Summary 60

6. ENHANCED SENSING OF WEAK PERTURBATIONS IN DISSIPATIVELY COUPLED TWO-MODE SYSTEMS 61

6.1 Linear response in a dissipatively coupled two-mode system 62
6.2 Enhanced sensing of weak nonlinear perturbations 64
6.3 Results on enhanced sensing for a dissipatively coupled cavity-magnon system 65
6.4 Summary 69

7. ULTRA-LOW THRESHOLD BISTABILITY AND GENERATION OF A LONG-LIVED MODE 71

7.1 Bistability threshold in dissipatively coupled systems 73
7.2 Dissipatively coupled nonlinear magnonic system 76
7.3 Probes of bistability via the waveguide transmission 79
7.4 Anharmonicity-induced long-lived mode 84
7.5 Summary 88

8. CAVITY-MEDITATED LEVEL ATTRACTION AND REPULSION BETWEEN MAGNONS 90

8.1 Level repulsion and attraction between magnons 92
8.2 Spin currents under the conditions of level attraction and repulsion 98
8.3 Excitation of dark polariton via symmetry-breaking 100
8.4 Dissipative-coupling-induced transparency 102
8.5 Summary 105

9. QUANTUM ENTANGLEMENT BETWEEN MACROSCOPIC FERRITE SAMPLES ... 106

9.1 Quantum Langevin equations of the system 108
9.2 Logarithmic negativity as a measure of quantum entanglement 111
9.3 Experimentally realizable tests for entanglement 114
9.4 Squeezed magnon states 116
9.5 Summary 117

10. SUMMARY AND OUTLOOK 118

REFERENCES 121

APPENDIX A. DERIVATION OF THE MASTER EQUATION FOR A CHAIN OF EMITTERS COUPLED TO A WAVEGUIDE 142

APPENDIX B. ADIABATIC THEORY OF LEVEL ATTRACTION 146

LIST OF FIGURES

FIGURE Page

3.1 Schematic of cavity magnons. Two YIG spheres are interacting with the basic mode of the microcavity in which the right mirror is made of a high-reflection material so that photons leak from the left side. The static magnetic field producing the Kittel mode in YIG1 is along the $\hat{z}$axis, whereas the static magnetic field for YIG2 is tilted with respect to the $\hat{z}$-axis. The microwave field is along the $\hat{y}$ and the magnetic field inside the cavity is along the $\hat{x}$ axis. 25

3.2 Spin current signal obtained from Eq. (3.5) illustrating bistability-multistability transition. (a,b) $\omega_c/2\pi$ = 10.078GHz; (c,d) $\omega_{\rm d}/2\pi$ = 10GHz. Other parameters are $\omega_1/2\pi$ = 10.018GHz, $\omega_2/2\pi$ = 9.963GHz, $g_1/2\pi$ = 42.2MHz, $g_2/2\pi$ = 33.5MHz, $U_1/2\pi$ = 7.8nHz, $U_2/2\pi$ = 42.12nHz, $\gamma_1/2\pi$ = 5.8MHz, $\gamma_2/2\pi$ = 1.7MHz and $\gamma_c/2\pi$ = 4.3MHz. In Fig.3.2(b), for drive power= 30mW, we observe three stable states given by $x = 1.58 \times 10^{14}$, $x = 5.6 \times 10^{14}$ and $x = 8.83 \times 10^{14}$. 27

3.3 Spin current signal against drive power at different values of cavity leakage. (a) $\gamma_c < g_{1,2}$ indicates strong magnon-cavity coupling; (b,c) $\gamma_c \simeq g_{1,2}$ indicates the intermediate magnon-cavity coupling; (d) $\gamma_c > g_{1,2}$ gives rise to weak magnon-cavity coupling. $\omega_c/2\pi$ = 10.078GHz, $\omega_{\rm d}/2\pi$ = 9.998GHz and other parameters are the same as Fig.3.2. 28

3.4 Schematic of the change in the linear transmission as increasing the driving power on the YIG sphere that activates nonlinearities of the sphere. The output spectrum exhibits shifts and asymmetries (See Fig. 3.4 for exact behaviour)..... 30

3.5 (a) Transmission spectrum for a single YIG in a single-mode microwave cavity, as a function of scanning probe frequency, according to Eq. (3.12). Blue line is for the case when turning off the drive field. Figure 3.5(b) depicts the spin polarization against the drive power. We observe that, for drive power = 90mW, there are two stable states at $|\mathscr{M}^{(0)}|^2 = 0.66 \times 10^{15}$ and $|\mathscr{M}^{(0)}|^2 = 2.55 \times 10^{15}$. The green and red lines in Fig. 3.5(a) are for the same bistable states with input power $P_{\rm d}$ = 90mW. Figure 3.5(c) depicts the frequency shift of the lower polariton peak as a function of drive power. Parameters are $\omega_c/2\pi$ = 10.025GHz, $\omega_m/2\pi$ = 10.025GHz, $\omega_{\rm d}/2\pi$ = 9.998GHz, $g/2\pi$ = 41MHz, $U/2\pi$ = 8nHz, $\gamma_m/2\pi$ = 17.5MHz and $\gamma_c/2\pi$ = 3.8MHz, taken from recent experiments [1]. 32

3.6 (a) Transmission spectrum for two YIG in a microwave cavity, as scanning probe frequency, according to Eq. (3.21). The blue line is for the case without driving, while green, black and red lines are for triple states with input power $P_{\rm d}$ = 30mW. They represent the same three stable states described in Fig. 3.2(b). (b) Frequency shift associated with upper polariton peak, where $\delta_{\rm HP} = \omega_{\rm HP} - \omega_{\rm d}$. Other parameters are $\omega_c/2\pi$ = 10.078GHz, $\omega_1/2\pi$ = 10.018GHz, $\omega_2/2\pi$ = 9.963GHz, $\omega_{\rm d}/2\pi$ = 9.998GHz, $g_1/2\pi$ = 42.2MHz, $g_2/2\pi$ = 33.5MHz, $U_1/2\pi$ = 7.8nHz, $U_2/2\pi$ = 42.12nHz, $\gamma_1/2\pi$ = 5.8MHz, $\gamma_2/2\pi$ = 1.7MHz and $\gamma_c/2\pi$ = 4.3MHz. 34

3.7 Transition between bistability and multistability. (a) $\omega_c/2\pi$ = 10.078GHz, $\omega_{\rm d}/2\pi$ = 9.9909GHz and (b) $\omega_c/2\pi$ = 10.078GHz, $\omega_{\rm d}/2\pi$ = 9.9989GHz; (c) $\omega_c/2\pi$ = 10.06GHz, $\omega_{\rm d}/2\pi$ = 10GHz and (d) $\omega_c/2\pi$ = 10.075GHz, $\omega_{\rm d}/2\pi$ = 10GHz. Other parameters are the same as Fig. 3.2. 37

3.8 Frequency shift of upper polariton against input power at different values of cavity leakage. (a) $\gamma_c < g_{1,2}$ indicates strong magnon-cavity coupling; (b,c) $\gamma_c \simeq g_{1,2}$ indicates the intermediate magnon-cavity coupling; (d) $\gamma_c > g_{1,2}$ gives rise to weak magnon-cavity coupling. All the parameters are same as Fig.3.3. 38

4.1 Schematic of two ferrimagnetic samples of YIG, coherently coupled to a single-mode cavity, which is driven externally by a two-photon parametric drive. A uniform bias magnetic field B_0 applied to either of the YIG spheres generates the corresponding Kittel mode and the YIG1 is driven externally by a coherent drive of low photon occupancy. 44

4.2 Phase diagram highlighting the region of stable dynamics for (a) the three-mode cavity-magnon system considered in this letter, and (b) a parametrically driven single-mode cavity without any coupled accessories. 45

4.3 Spin-current amplification factor plotted (a,b) over the two-dimensional $\Delta - G$ plane, and (c) against G for $\Delta/\kappa = 3$. The figures in (b,c), plotted in logarithmic scale, highlights the region where F exceeds 10, and testify to the tremendous level of enhancement near the phase boundary $G_c/\kappa = 0.95$. The inset in (b) depicts a narrow segment of this region while the inset in (c) is a plot over the domain where F is bounded above by 10. 47

4.4 Comparative graph illustrating the respective enhancement factors under the two-photon resonance condition $\delta/\kappa = 0$, and in the detuned scenario, with $\delta/\kappa = 0.2$ chosen as an example. Here, $\delta = \omega_d - \omega_p/2$ signifies the two-photon detuning. 49

4.5 (a) Real and (b) Imaginary parts of the eigenvalues of the reduced 4×4 system involving the modes a and $M = (m_1 + m_2)/\sqrt{2}$ (as described by Eq. (4.3)). 50

4.6 Higher-order energy transitions afforded by the parametric drive, assuming that YIG1 is driven by a coherent field at one-photon level. 52

5.1 a), b) Eigenfrequencies and linewidths for an anti-$\hat{PT}$ symmetric system, plotted against a variable $\Delta = \delta/2$, calculated in units of Γ. While EPs emerge at $\Delta = \pm\Gamma$, the VIC-induced linewidth suppression (designated as X) corresponds to $\delta = 0$. c), d) Analogous plots for the $\hat{PT}$ symmetric system, against the coupling strength g, in units of γ, at $\Delta = 0$. EPs are found at $g = \pm\gamma$. 57

5.2 Schematic of a general two-mode system dissipatively coupled through a waveguide. $\gamma_{a(b)}$ and Γ describe decay into the surrounding (local heat bath) and coupling to the fiber (shared bath) respectively. 58

6.1 Schematic of the cavity-magnonic setup. The microwave cavity, running transverse to the waveguide, interacts with the YIG via the transmission line. A static magnetic field aligned along the z-axis generates the Kittel mode in YIG. (Redrawn from *Phys. Rev. Lett.* ***125****, 147202 (2020).*) 66

6.2 a) The spin current plotted against δ at two different nonlinearities; b) spin currents away from the VIC condition, compared against the lossless scenario, at different drive powers- for ease of comparison, the blue and red curves have been scaled up by 10; c) contrasting responses observed at a drive power of 1 mW for two different strengths of nonlinearity; d) sensitivity for a nonzero coherent coupling g at $D_p = 1$ μW..... 67

6.3 a) Real and b) imaginary parts of the eigenvalues of $\mathscr{H}_{NL}$ at a drive power of 0.1 W. 68

7.1 General two-mode system, with both coherent and dissipative pathways of interaction. HB_α = heat bath of mode α, with $\alpha = S$ denoting a shared reservoir..... 74

7.2 Schematic of a YIG sphere interacting remotely with a single-mode cavity, with the coupling mediated by a waveguide. (Redrawn from *Phys. Rev. Lett.* ***125****, 147202 (2020).*) 77

7.3 Response in the cavity field plotted against the pump power, for varying strengths of the dissipative coupling. Weaker dissipative couplings support larger ranges of the drive power pertaining to bistable states in the response. The parameters $\gamma_0/2\pi = 5$ MHz and $\mathscr{U}/2\pi = 42.1$ nHz. 78

7.4 Effect of intrinsic damping on the optical bistability. Other parameters are $\Gamma/2\pi = 5$ MHz and $\mathscr{U}/2\pi = 42.1$ nHz. The detunings are scaled down by a factor $S = 2\pi \times 20$ MHz. 80

7.5 (a) The cavity response plotted against the pump power showcasing the two stable states at $D_p = 90$ mW. (b) Transmission spectra through the waveguide as a function of the scanning frequency. (c) Shifts in lower polariton frequency vs. the pump power D_p. Other parameters are $\Gamma/2\pi = 5$ MHz, $\gamma_0/2\pi = 5$ MHz and $\mathscr{U}/2\pi = 42.1$ nHz. Scaling factor for detunings $S = 2\pi \times 20$ MHz..... 81

7.6 The lower polariton frequency shifts against pump power D_p for varying values of the intrinsic damping. All the other parameters are identical to Fig. 7.4. 83

7.7 (a) Real parts and (b) Imaginary parts of the eigenvalues of $\mathscr{H}_{NL}$ plotted against δ at $Dp = 0.02$ W. (c) $|t|$ is plotted against δ_p and δ at the same pump power. The vertical lines in (a), (b) and (c), all at $\delta/2\gamma = -3.37$, identify the exceptionally long-lived mode with extreme linewidth suppression. Other parameters are identical to Fig. 7.5. 85

7.8 Figures (a), (b) represent the transmission spectra against the probe detuning δ_p at two different values of δ, portraying the asymmetry and the transition from unidirectional reflection to perfect transmission. (c) Transmission spectra against δ with $\delta_p = 0$, highlighting a region of significant gain around $\delta/2\gamma = -3.7$. (d) Transmission plot demonstrating pronounced sensitivity around $\delta_p = 0$. Other parameters are identical to Fig. 7.5. Scaling factor for detunings $S = 2\pi \times 20$ MHz. 87

8.1 Schematic of two YIGs coherently coupled to a single-mode microwave cavity. The static magnetic fields exciting the Kittel mode in both the YIGs are aligned along the z-axis. The intracavity field mode is propagating along the y-axis, with the corresponding magnetic field directed along the x-axis. 93

8.2 Level anticrossing and level crossing in two different regimes of cavity QED; (a) Eigenfrequencies of the cavity-magnon system for $g = 2$ and $\gamma_i = 1$ exhibiting level splitting; (b) Eigenfrequencies and (c) Linewidths in the case of $g = 0.2$ and $\gamma_i = 0.01$, with the features of level crossing; (d) Eigenfrequencies in the case of asymmetric decay rates $\gamma_1 = 0.01$, $\gamma_2 = 0.012$ and $g = 0.2$ demonstrating level attraction. All the parameters are chosen in units of κ. 94

8.3 (Panel A; a-e) Sumtotal of the spincurrent response $|m_1|^2 + |m_2|^2$ plotted as functions of Δ_a in the case of strong magnon-photon coupling $g = 2$ and equal relaxation rates $\gamma_i = 1$ (similar to Fig. 8.2(a)). Note the conspicuous extinction of the central resonance in (A; c). (Panel B; a-e) Profiles for the case of $g = 0.2$, $\gamma_i = 0.01$ (similar to Fig. 8.2(b,c)). Only two peaks appear in this scenario. Drive power $P = 1$ mW. Other parameters are given in the text. 97

8.4 Reflection spectra for (a) $s = 0.01$ with $\gamma_i = 0$, and (b) $s = 0.04$ with $\gamma_i = 0.01$. Other parameters are $g = 0.2$ and $\kappa = 1$, which yields $\Gamma = g^2/\kappa = 0.04$. 103

9.1 Two YIG spheres are placed inside a microwave cavity near the maximum magnetic field of the cavity mode, and simultaneously in a uniform bias magnetic field. The cavity is driven by a weak squeezed vacuum field generated by a flux-driven JPA. The magnetic field of the cavity mode is in the x direction and the bias magnetic field is applied along the z direction. 109

9.2 Density plot of bipartite entanglement $E_{m_1m_2}$ between the two magnon modes versus Δ_a and Δ_{m_1} (a) with $\Delta_{m_2} = \Delta_{m_1}$, $r = 1$, $T = 20$ mK, (b) with $\Delta_{m_2} = \Delta_{m_1}$, $r = 1.5$, $T = 20$ mK. Other parameters are given in the text. 112

9.3 Plot of bipartite entanglement $E_{m_1m_2}$ between the two magnon modes against temperature with $\Delta_a = \Delta_{m_1} = \Delta_{m_2} = 0$ and $r = 1.5$. 112

9.4 Density plot of bipartite entanglement $E_{m_1m_2}$ between the two magnon modes versus Δ_a and Δ_{m_1} (a) with $\Delta_{m_2} = \Delta_{m_1}/2$, $r = 1.5$, $T = 20$ mK. (b) with $\Delta_{m_2} = 0$, $r = 1.5$, $T = 20$ mK. 114

9.5 (a) $\langle M_x^2 \rangle + \langle m_y^2 \rangle$ against Δ_a and Δ_{m_1} with $\Delta_{m_2} = \Delta_{m_1}$, $r = 1.5$, $T = 20$ mK. (b) $\langle M_x^2 \rangle$ against Δ_a and squeezing parameter r with $\Delta_{m_1} = \Delta_{m_2} = 0$, T=20 mK. 115

9.6 (a) Variance of the first magnon quadrature $\langle x_1(t)^2 \rangle$ versus Δ_a and Δ_{m_1}. (b) Variance of the first magnon quadrature against squeezing parameter r and phase θ. The other parameters in (a) are $r = 1.5$, $\Delta_{m_1} = \Delta_{m_2}$, T =20 mK. Other parameters in (b) are $\Delta_a = \Delta_{m_1} = \Delta_{m_2} = 0$ and T =20 mK. $\langle x_2(t)^2 \rangle$ is identical to $\langle x_1(t)^2 \rangle$. 116

A.1 An array of N single-mode quantum emitters coupled to the evanescent field of a one-dimensional waveguide, with $\gamma_\alpha = \kappa_{\alpha\alpha}$ denoting the individual coupling rates. The waveguide can be adiabatically eliminated to yield the master equation of the emitter chain. 142

1. INTRODUCTION

In the last few years, technologies based on quantum mechanical principles have begun revolutionizing our world in an unprecedented way [2–4]. Considering the large volume of information created, platforms for the manipulation and processing of quantum data are a prerequisite for the control of various protocols. However, not a single system is possible to be employed in realizing all the requirements of a present-day quantum information processing system. For example, photons are efficient carriers of information over long distances. At the same time, they do not interact between themselves and this in conjunction with the decoherence effects makes an all-optical design difficult to engineer. In contrast, superconducting circuits [5] can rapidly process information and spins [6] can store information. In other words, modern quantum machines require hybrid quantum systems [7, 8] with multitasking capabilities, involving, photons, phonons [9], atoms [10], ions [11] and in general, qubits [12], thereby facilitating the advancement of newer technologies in the domains of information processing [13], computation [14–16] and communication [3, 17] and sensing [18, 19].

Recently, hybrid quantum platforms based on collective excitations in magnetic systems have attracted much traction among the scientific community. The prime concept is to employ collective excitations in spin degrees freedom, i.e., magnons of ordered magnetic systems for the storage of information. In particular, ferrimagnetic materials like Yttrium iron garnet (YIG) have been used in research where experimental activity has flourished of late [1, 20–35]. Owing to their high spin density and low damping rates, YIGs are excellent candidates for magnonic setups. However, magnon-photon coupling in free space is extremely weak and it therefore warranted confinement of light into small volumes. A prominent approach in the context of atom-photon coupling has been that of cavity-quantum electrodynamics (cavity-QED) [36], wherein, high-quality resonators are used to enhance light-matter interactions. In 2013, Hübel *et al.* demonstrated a strong coupling between YIG and a superconducting coplanar resonator [20], spawning a new field of research at the intersection between condensed matter physics and quantum optics, dubbed as quantum

magnonics. Subsequently, Tabuchi *et al.* observed normal-mode splitting at cryogenic and room temperatures between YIG and a microwave cavity giving rise to cavity-magnon polaritons (CMPs) [21] while Zhang *et al.* demonstrated ultra-strong coupling by reducing the cavity mode volume and by ramping up the number of spins [22]. In another experiment, Tabuchi *et al.* established a strong coupling between a ferromagnetic sphere and a superconducting qubit, demonstrating control of magnon at the single quantum level [25]. Following the discovery of strong magnon-photon coupling, cavity magnonic systems have been used to demonstrate several intriguing phenomena which were first observed in the context of quantum optical systems involving atoms and cavities. For instance, in 2018, Wang *et al.* revealed bistability in CMPs using Kerr nonlinearity in a YIG sample [1]. Some other interesting experiments include microwave-to-optical transducers [35], exceptional points [30], dark modes [24] etc. to name a few.

In 2017, Bai *et al.* demonstrated the cavity-mediated remote exchange of spin excitations between two macroscopic YIGs in the linear domain of system parameters [29]. However, YIGs are anharmonic on account of the magneto-crystalline anisotropies present in the system [37]. Motivated by this, we developed a theory for the spin current in the nonlinear domain where the external drive is strong so that one needs to include the Kerr nonlinearity of the ferrite materials [38]. In this way, the nonlinear polaritons are created and we demonstrated the possibility of achieving both bistable and multistable signatures in the spin current response by obtaining a variety of steady-state results. Note that the system was driven into a far-from-equilibrium steady state that is determined by the details of external driving and various interactions. In addition, we developed a model for the spectroscopic detection of nonlinear spin currents, unfolding some of the key features of the nonlinear polaritons. The transmission of a weak probe field was used to obtain the shift in polaritonic peaks as a function of the pump power which perfectly replicated the multistable behaviour of the spin current signal. In 2021, our results were verified by Dr. You's group at Zhejiang University.

Since the observation of strong magnon-photon coupling, the lion's share of research in the field of cavity-magnonics was in the semiclassical domain whereas the system could potentially

be used to observe quantum effects at the macroscopic scale. One of the ways to observe quantum effects in a system is through the transfer of nonclassical properties from a quantum source, for instance, via the application of quantum light. In [39], we presented a scheme to generate entangled pair of YIG samples placed in a microwave cavity by the application of an external drive with quantum effects. The external drive was produced by a flux-driven Josephson parametric amplifier (JPA) which generates a microwave field with strong squeezing properties [40–51]. Further, we demonstrated a number of experimentally realizable tests for entanglement and illustrated that the generated entanglement could survive up to 300 mK. As a by-product of our results, we investigated squeezing in the collective magnon variables which can be achieved by resonantly driving the cavity with a squeezed vacuum field. Note, *en passant*, that our scheme for entangling magnetic samples does not require the use of nonlinearities in the system, which are typically weak.

As discussed earlier, cavity-mediated magnon-magnon coupling can lead to a transfer of spin-wave excitations between two spatially separated magnetic samples and it is desirable to have a mechanism to boost the transfer efficiency. One standard technique is to use high-quality cavities and large coupling between photons which would in turn result in the improved transfer of energy. In [52], we presented a scheme to substantially amplify this transfer efficiency through the application of a two-photon parametric drive on the cavity which could be produced either from a $\chi^{(2)}$-type or $\chi^{(3)}$-type nonlinearity [53]. Some other applications of parametric interactions include the observation of enhanced cooling [54], exponentially enhanced spin-cavity photon coupling [55, 56], enhanced phonon-mediated spin-spin coupling in a system of spins coupled to a cantilever [57], possibility of first order superradiant phase transitions [58], enhancement in the generation of entangling gates [59], amplification of small displacements of trapped ions [60] etc. The enhancement in the transfer efficiency in our scheme can be pinned down to the recurrent multiphoton absorption by the cavity opens up an infinite ladder of accessible energy levels, which can induce higher-order transitions within the magnon Fock space. This was reflected in a heightened spin-current response from one of the magnetic samples when the neighbouring sample is coherently pumped. The enhancement induced by the parametric drive can be considerably high

within the stable dynamical region. Specifically, near the periphery of the stability boundary, the spin current is amplified by several orders of magnitude. Such striking enhancement factors are attributed to the emergence of parametrically induced strong coherences precipitated by a long-lived mode, which is analogous to a bound state in continuum (BIC) [61–65].

So far, we have introduced some of the interesting physics emerging out of coherently coupled cavity-magnon systems. In 2018, Harder *et al.* observed a dissipative form coupling between magnons and photons revealing coalescence of the hybridized modes [66]. This was subsequently verified in a variety of cavity-magnonic configurations [67–76], including, for example, coplanar waveguides [72]. It is well-known that coherent coupling owes its origin to the spatial over between modes. In contrast, the dissipative coupling is an indirect coupling, *viz*, it is mediated by dissipative channels. In essence, dissipative coupling between any two modes can be engineered by coupling them through a common intermediary reservoir, for example, a waveguide. Dissipative coupling does not lend itself to a Hamiltonian description and it follows from the master equation description of the subsystems, obtained by eliminating the reservoir degrees of freedom [77]. An interesting consequence of dissipative coupling is the realization of anti-$\hat{PT}$ symmetry [75, 76, 78, 79], a feature of non-Hermitian Hamiltonians that change sign under the action of $\hat{PT}$. In particular, two-mode anti-$\hat{PT}$ symmetric systems possess a BIC which can be used to enhance experimentally observable parameters.

In [80], we proposed an expedient sensing scheme relevant to dissipatively coupled anti-Parity-Time (anti- $\hat{PT}$) symmetric systems and customized for the fine-grained estimation of anharmonic perturbations. The sensitivity to anharmonicities is derived from the coherence between two modes induced by a common vacuum. Owing to this coherence, the linear response acquires a pole on the real axis, i.e., a BIC. We demonstrated how this BIC can be exploited for the enhanced sensing of very weak anharmonicities at low pumping rates. Our results are applicable to a wide class of systems, and we specifically illustrated the remarkable sensing capabilities in the context of a weakly anharmonic Yttrium Iron Garnet (YIG) sphere interacting with a cavity via a tapered fiber waveguide. A small change in the anharmonicity led to a substantial change in the induced spin

current.

Extending our work on dissipatively coupled systems, we established the remote transfer of bistability from a nonlinear resource in a dissipatively coupled two-mode system [81]. As a clear advantage over coherently coupled settings, the dissipative nature of the interaction was found to support a lower pumping threshold for bistable signals. In fact, for comparable parameters, the bistability threshold for dissipatively coupled systems is lower by a factor of about five and we specifically illustrated our results in the context of a cavity-magnon system, interacting via a waveguide. Further, we spectroscopically studied the resulting hysteresis by applying a probe field through the waveguide and examining the polariton character of the transmitted field. As a consequence of dissipative coupling and the nonlinearity, we observed the emergence of a long-lived eigenmode which is responsible for heightened transmission levels and pronounced sensitivity in signal propagation through the waveguide. It is worth mentioning that dissipatively coupled anti-$\hat{PT}$ symmetric systems can also be used for the enhanced bidirectional conversion between microwave and optical fields [82].

An interesting feature of dissipatively coupled systems is the possibility of level attraction. Consider two coupled harmonic oscillators with their dynamics described by an effective non-Hermitian Hamiltonian. If the eigenfrequencies of the system do not coalesce at any point in parameter space, there exists a minimum separation between the energy eigenvalues known as level repulsion, a property of coherently coupled systems. In contrast, there could be a scenario where the modes intersect at certain points in the parameter space and this phenomenon is known as level attraction. In the context of cavity-magnonics, we elucidated two widely dissimilar parameter domains that bring forth the contrasting possibilities of level splitting and level crossing [83]. The former was observed in the regime of strong magnon-photon couplings, particularly when the three modes bear comparable relaxation rates. This character was marked by the appearance of three distinguishable and non-converging polariton branches in the spectral response to a cavity drive. However, when the bare modes are resonant and the couplings perfectly symmetrical, one of the spectral peaks gets wiped out. This anomalous extinction of polaritonic response can be

traced down to the existence of a conspicuous dark mode alongside two frequency-shifted bright modes. In an alternate parameter regime, where the magnon modes are weakly coupled to the cavity, features of level attraction unfold, subject to a large relaxation rate for the cavity mode. The emergence of level attraction can be reconciled with a theoretical model that embodies the dynamics of the magnon-magnon subsystem when the cavity field decays rapidly into its steady state, revealing a purely dissipative coupling between the magnon modes.

In this thesis, we discuss in detail our findings on the analyses of interactions between magnonic systems with quantum optical architectures involving microwave cavities and waveguides. The results presented in this thesis are primarily based on the following published articles

1. J. M. P. Nair, and G. S. Agarwal, *Deterministic quantum entanglement between macroscopic ferrite samples*, Applied Physics Letters, **117** (8), 084001 (2020).

2. J. M. P. Nair, Z. Zhang, M. O. Scully, and G. S. Agarwal, *Nonlinear spin currents*, Phys. Rev. B **102** (10), 104415 (2020).

3. J. M. P. Nair, D. Mukhopadhyay, and G. S. Agarwal, *Enhanced Sensing of Weak Anharmonicities through Coherences in Dissipatively Coupled Anti-PT Symmetric Systems*, Phys. Rev. Lett. **126**, 180401 (2021).

4. J. M. P. Nair, D. Mukhopadhyay, and G. S. Agarwal, *Ultralow threshold bistability and generation of long-lived mode in a dissipatively coupled nonlinear system: Application to magnonics*, Phys. Rev. B **103** (22), 224401 (2021).

5. D. Mukhopadhyay, J. M. P. Nair and G. S. Agarwal, *Anti-$\hat{P}\hat{T}$ symmetry enhanced interconversion between microwave and optical fields*, Phys. Rev. B **105** (6), 064405 (2022).

6. J. M. P. Nair, D. Mukhopadhyay, and G. S. Agarwal, *Cavity-mediated level attraction and repulsion between magnons*, Phys. Rev. B **105** (21), 214418 (2022).

7. D. Mukhopadhyay, J. M. P. Nair and G. S. Agarwal, *Quantum amplification of spin currents in cavity magnonics by a parametric drive induced long-lived mode*, Phys. Rev. B **106** (18),

184426 (2023).

This thesis is divided into nine chapters. In Chapter 2, we detail the theory of spin waves in an ordered magnetic system and review the progress in the recent field of magnonics coupled with quantum optical elements. In Chapter 3, we consider a cavity magnonic system comprising of two YIG samples placed in a microwave cavity and we detail two distinct domains of interactions leading to the possibility of multistability in the system and in Chapter 4, we discuss a scheme for the enhanced transfer of energy between magnets. We review the general symmetry properties of non-Hermitian systems in Chapter 5, especially anti-$\hat{PT}$ symmetric systems and their possible experimental realizations. In addition, we explicate the mechanism of sensing linear perturbations in a $\hat{PT}$ symmetric system based on EPs. In Chapter 6, we expound a protocol for the enhanced sensing of weak nonlinear perturbations in a dissipatively coupled two-mode system through the generation of an especially long-lived mode in anti-$\hat{PT}$ symmetric systems. The dissipatively coupled system is also shown to exhibit a significantly low bistability threshold compared to coherently coupled systems in Chapter 7. In Chapter 8, we consider a coherently coupled cavity-magnon system and illustrate the possibility of observing level attraction between two YIG samples without the use of common intermediary reservoirs. A protocol for entangling two magnetic systems in a cavity through the application of quantum light is elucidated in Chapter 9 and we provide a summary of our results in chapter 10.

2. MAGNONICS

Magnons are quanta of elementary excitations in an ordered magnetic system where spins interact primarily through exchange and dipolar interactions. In a lattice of spins where inter-spin spacing is small enough, spatial overlap between particles results in the exchange interaction leading to the Heisenberg exchange Hamiltonian. Note, however, the strength of the exchange interaction decreases exponentially with increasing inter-spin spacing, i.e., exchange interaction is short range and nearest neighbour approximation is typically valid. In contrast, dipole-dipole interaction (DDI) is long-range. The theory of spin-waves in a magnetic system was first developed by Bloch in 1932 which used general perturbation theory [84], but the theory could not explain magnon-magnon interactions. In 1940, Holstein and Primakoff used the symmetry properties of spin ladder operators to introduce an elegant nonlinear transformation which mapped spins at each lattice site to a quantized harmonic oscillator represented by bosonic operators [85]. This paved the foundations of spin-wave theory which perfectly predicted the interactions between magnons. Later on, Dyson generalized the theory of spin waves with a more exact treatment of the problem [86]. Magnonics deals with the control and manipulation of collective spin excitations and thanks to the rapid technological development over the last decade, it saw a resurgence in interest among the scientific community. Of particular importance is the demonstration of strong coupling between magnons and microwave photons by Hübel *et al.* in 2013 [20] which kick-started the field of cavity magnonics. Cavity and waveguide-integrated magnonic systems have since been extensively used in experiments leading to the observation of several interesting new physics. In this chapter, we introduce the quantum theory of spin waves and their interaction with photons [87].

This chapter is organized as follows. In section 2.1, we consider a generic Hamiltonian of a magnetic system comprising of exchange, dipolar and Zeeman interactions and use Holstein-Primakoff transformations to quantize the excitations from the ground state and we specifically illustrate the emergence of magnon-magnon interactions. In section 2.2, we provide a short overview of the theory of magnon-photon interaction and detail some of the recent developments in the do-

main of cavity-magnonics. Finally, we summarize the chapter in section 2.3.

2.1 Spin waves in an ordered magnetic system

We start off by considering a generic Hamiltonian of a 3D magnetic system [87] which has the form

$$\hat{H} = -\frac{1}{2}\sum_{ij} J_{ij}\hat{\mathbf{S}}_i.\hat{\mathbf{S}}_j - g\mu_B \sum_i \mathbf{B}_0.\hat{\mathbf{S}}_i, \tag{2.1}$$

where $\mathbf{S}_i$ are the spin operators at location $\mathbf{r}_i$ which follow the commutation relations $[\mathbf{S}_i^\alpha, \mathbf{S}_j^\beta] = i\hbar\delta_{ij}\epsilon_{\alpha\beta\gamma}\mathbf{S}_i^\gamma$ and α, β, γ represent the spatial coordinates of the spin. The first term on the right-hand side (RHS) of Eq. 2.1 constitutes the Heisenberg exchange interaction between spins with the exchange coefficient $J_{ij} > 0$, whereas the second term on the RHS represents the Zeeman energy from a static bias magnetic field B_0, the direction which is taken to be the $\hat{z}$ axis. The parameters g and μ_B are respectively the Lande g factor and the Bohr magneton. The exchange energies decay exponentially with increasing distance between the spins and therefore, for all practical purposes we may assume $J_{ij} = J$ for nearest neighbour spins. In addition, for the subsequent analysis in this section, we have dropped the DDI interactions. The effect of this term will be discussed at a later stage. Notice that we have set $\hbar = 1$ in the above Hamiltonian.

Let us examine Heisenberg interaction Hamiltonian in detail. To this end, it is appropriate to recast the Hamiltonian in terms of the ladder operators defined by $S_i^\pm = S_i^x \pm S_i^y$ with

$$\hat{S}_i^\pm \left|S_i, S_i^z\right\rangle = \sqrt{(S_i \mp S_i^z)(S_i + 1 \pm S_i^z)}\left|S_i, S_i^z \pm 1\right\rangle \tag{2.2}$$

where we have used $\hat{\mathbf{S}}_i^2 \left|S_i, S_i^z\right\rangle = S_i(S_i+1)\left|S_i, S_i^z\right\rangle$ and $\hat{S}_i^z \left|S_i, S_i^z\right\rangle = S_i^z \left|S_i, S_i^z\right\rangle$. Therefore the first term on the RHS of Eq. (2.1) morph into

$$\hat{H}_H = -\frac{J}{2}\sum_{ij}\Big(\frac{1}{2}(\hat{S}_i^+\hat{S}_j^- + \hat{S}_i^-\hat{S}_j^+) + \hat{S}_i^z\hat{S}_j^z\Big). \tag{2.3}$$

Here, the Hamiltonian $\hat{H}_H$ is used to denote the Heisenberg interaction part of the Hamiltonian $\hat{H}$. It is straightforward to show that the state $|G\rangle = \prod_i |S_i, S_i\rangle$, that is the state in which all the sins are polarized along one direction with maximum magnitude. The action of $\hat{H}_H$ on $|G\rangle$ is given by

$$\hat{H}_H |G\rangle = -\frac{J}{2} \sum_{<ij>} S_i S_j |G\rangle , \tag{2.4}$$

with energy $E = -\frac{J}{2} \sum_{<ij>} S_i S_j$. Note that $\hat{S}_i^+ |G\rangle = 0$ and we assume that all the spins are identical with $S_i = S_j = S$. Therefore, it is apparent from Eq. (2.3) and Eq. (2.4) that any other state with $S^z < S$ would bring about an energy $\tilde{E}$ which is greater than E_0. Stated differently, $|G\rangle$ is indeed the ground state of the Heisenberg interaction Hamiltonian. However, the ground state is not unique, i.e., there are $2NS + 1$ states with identical energy where N is the total number of spins. The effect of the Zeeman energy term is to break the symmetry and all the spins align along the direction of B_0. Note *en passant*, the magnetic ordering in ferromagnets owes its origin primarily to the exchange interactions which prevail over DDI at short distances.

2.1.1 Holtein-Primakoff theory of spin waves

In preparation for the study of excitations in the ferromagnet, it is convenient to rewrite the spin operators $\{\hat{S}_i^z, \hat{S}_i^+, \hat{S}_i^-\}$ at each location in terms of bosonic annihilation and creation operators $\{\hat{a}_i, \hat{a}_i^\dagger\}$, viz, mapping the Hamiltonian at each location to a harmonic oscillator. Before going into the details of the transformation, let us briefly recapitulate the bosonic operator algebra. The raising and lowering operators of the harmonic oscillator follow the commutation relations

$$\begin{aligned} [\hat{a}_i, \hat{a}_j^\dagger] &= \delta_{ij} \\ [\hat{a}_i^\dagger, \hat{a}_j^\dagger] &= [\hat{a}, \hat{a}_j] = 0, \end{aligned} \tag{2.5}$$

with their action on the number state $|n_i\rangle$ provided by

$$\begin{aligned} \hat{a}_i^\dagger \hat{a}_i |n_i\rangle &= n_i |n_i\rangle \\ \hat{a}_i |n_i\rangle &= \sqrt{n_i} |n_i - 1\rangle \\ \hat{a}_i^\dagger |n_i\rangle &= \sqrt{n_i + 1} |n_i + 1\rangle . \end{aligned} \tag{2.6}$$

In 1940, Holstein and Primakoff introduced a nonlinear transformation interlinking the spin operators and the bosonic operators given by

$$\begin{aligned} \hat{S}_i^+ &= \sqrt{2S - \hat{a}_i^\dagger \hat{a}_i} a_i \\ \hat{S}_i^z &= S - \hat{a}_i^\dagger \hat{a}_i. \end{aligned} \tag{2.7}$$

It is interesting to look at the action of $\hat{S}_i^z$ on $|n_i\rangle$, that is

$$\hat{S}_i^z |n_i\rangle = (S - n_i) |n_i\rangle . \tag{2.8}$$

Note that the number operator $\hat{a}_i^\dagger \hat{a}_i$ effectively counts the number of flipped spins in the ferromagnet and the state $|0\rangle$ represents the fully polarized spin state. In the low-temperature limit, we assume that the total number of excitations in the bulk of the ferromagnet is much less compared to the total number of spins. To simplify the analysis, let us rewrite the first part of Eq. (2.7) as

$$S_i^+ = \sqrt{2S}(1 - \frac{\hat{x}_i}{2} - \frac{\hat{x}_i^2}{8} + ..)a_i, \tag{2.9}$$

where $\hat{x}_i = \frac{a_i^\dagger a_i}{2S}$. Note that this assumes $a_i^\dagger a_i < 2S$ which may not be true for small S and it would appear that the expansion in Eq. (2.8) is erroneous. However, notice that the spin operators are summed over the bulk of the magnet and therefore, the series expansion is flawless as long as the average number of excitations at each site is much less compared to the number of spins, that is, $\langle a_i^\dagger . a_i \rangle << 2NS$. Substituting the above expansion into Eq. (2.3) together with the Zeeman energy

part of the Hamiltonian, we obtain

$$-\frac{JS}{2}\sum_{<ij>}\Big[(1-\frac{\hat{x}_i}{2}-\frac{\hat{x}_i^2}{8}+...)a_i a_j^\dagger(1-\frac{\hat{x}_j}{2}-\frac{\hat{x}_j^2}{8}+...)h.c.\Big]-\frac{J}{2}\sum_{<ij>}(S-a_i^\dagger a_i)(S-a_j^\dagger a_j)$$
$$-g\mu_B B_0\sum_i(S-a_i^\dagger a_i) \qquad (2.10)$$

Keeping only terms up to quadratic in the ladder operators, we can reduce the above Hamiltonian into

$$-\frac{JS}{2}\sum_{<ij>}(a_i a_j^\dagger+a_i^\dagger a_j-a_i^\dagger a_i-a_j^\dagger a_j+S)-g\mu_B B_0 NS+g\mu_B B_0\sum_i a_i^\dagger a_i. \qquad (2.11)$$

Thus, we have transformed the spin Hamiltonian into a system of N harmonic oscillators in three-dimensional space with nearest-neighbor interactions. We may diagonalize Eq. (2.11) by employing the momentum space annihilation and creation operators defined by

$$a_{\mathbf{k}}=\frac{1}{\sqrt{N}}\sum_i e^{-i\mathbf{k}.\mathbf{r}_i}a_i. \qquad (2.12)$$

The operators $a_{\mathbf{k}}$ and $a_{\mathbf{k}}^\dagger$ involves the collective excitation or deexcitation of spins. A quasi-particle, namely a magnon created by the action of $a_{\mathbf{k}}^\dagger$ is an excitation through the action S_i^- at each site which is completely delocalized across the bulk of the system. It is straightforward to show that $[a_{\mathbf{k}},a_{\mathbf{k}'}^\dagger]=\frac{1}{N}\sum_i e^{i(\mathbf{k}-\mathbf{k}').\mathbf{r}_i}=\delta_{\mathbf{k}\mathbf{k}'}$. Inverting Eq. (2.12) substituting in Eq. (2.11) renders the momentum space Hamiltonian

$$\hat{\mathscr{H}}_Q=-\frac{NJZS^2}{2}-g\mu_B B_0(NS-\sum_{\mathbf{k}}a_{\mathbf{k}}^\dagger a_{\mathbf{k}})-\frac{JSZ}{2}\sum_{\mathbf{k}}(v_{\mathbf{k}}a_{\mathbf{k}}^\dagger a_{\mathbf{k}}+v_{-\mathbf{k}}a_{\mathbf{k}}a_{\mathbf{k}}^\dagger-2a_{\mathbf{k}}^\dagger a_{\mathbf{k}}), \qquad (2.13)$$

where Z denotes the number of nearest neighbours, $\nu_k = \frac{1}{Z}\sum_R e^{i\mathbf{k}.\mathbf{R}}$ and $\mathbf{R} = \mathbf{r}_i - \mathbf{r}_j$ is the real space vector connecting nearest neighbour spins. The Hamiltonian when $\nu_{\mathbf{k}} = \nu_{-\mathbf{k}}$ can recast into

$$\hat{\mathscr{H}}_Q = \sum_{\mathbf{k}} \omega_{\mathbf{k}} a^\dagger_{\mathbf{k}} a_{\mathbf{k}}, \tag{2.14}$$

where $\omega_{\mathbf{k}} = JSZ(1 - \nu_{\mathbf{k}}) + g\mu_B B_0$. Palpably, the resonance frequencies of each mode can be controlled externally by the static bias magnetic field B_0.

2.1.2 Magnon-magnon interactions

So far, we have discussed the quadratic part of the infinite series Hamiltonian in Eq. (2.10). In this section, we explicate the emergence of magnon-magnon interactions via the higher order terms in Eq. (2.10). To this end, we write down the fourth-order perturbations to the Hamiltonian as

$$-\frac{J}{2}\sum_{<ij>}(\hat{a}^\dagger_i \hat{a}_i \hat{a}^\dagger_j \hat{a}_j) + \frac{J}{8}(\hat{a}^\dagger_i \hat{a}_i \hat{a}_i \hat{a}^\dagger_j + \hat{a}_i \hat{a}^\dagger_j \hat{a}^\dagger_j \hat{a}_j + h.c.). \tag{2.15}$$

We already saw that the quadratic Hamiltonian can be diagonalized by moving to the Fourier space representation. By the same token, we use Eq. (2.12) in the above Hamiltonian. To elucidate the origin of magnon-magnon interactions, we consider only one of the terms in Eq. (2.15) lending

$$-\frac{J}{8}\sum_{<ij>}(\hat{a}^\dagger_i \hat{a}_i \hat{a}_i \hat{a}^\dagger_j) = -\frac{J}{8N^2}\sum_{<ij>}\sum_{\mathbf{k}_i\hat{\mathbf{k}}_2\mathbf{k}_3\mathbf{k}_4} e^{i(\mathbf{k}_1-\mathbf{k}_2-\mathbf{k}_3).\mathbf{r}_i}.e^{i\mathbf{k}_4.\mathbf{r}_j}\hat{a}^\dagger_{\mathbf{k}_1}\hat{a}_{\mathbf{k}_2}\hat{a}_{\mathbf{k}_3}\hat{a}_{\mathbf{k}_4} \tag{2.16}$$

$$= -\frac{J}{8N^2}\sum_{i\mathbf{R}} e^{i(\mathbf{k}_1-\mathbf{k}_2-\mathbf{k}_3).\mathbf{r}_i}.e^{i(\mathbf{k}_4.\mathbf{R}}\hat{a}^\dagger_{\mathbf{k}_1}\hat{a}_{\mathbf{k}_2}\hat{a}_{\mathbf{k}_3}\hat{a}_{\mathbf{k}_4} \tag{2.17}$$

$$= \frac{J}{8N}\delta(\mathbf{k}_1 - \mathbf{k}_2 - \mathbf{k}_3 - \mathbf{k}_4)u_{\mathbf{k}_4}\hat{a}^\dagger_{\mathbf{k}_1}\hat{a}_{\mathbf{k}_2}\hat{a}_{\mathbf{k}_3}\hat{a}_{\mathbf{k}_4}, \tag{2.18}$$

where $u_{\mathbf{k}_4} = \sum_{\mathbf{R}} e^{i\mathbf{k}_4.\mathbf{R}}$. The above Hamiltonian represents the physical process wherein a magnon of momentum $\mathbf{k}_1$ is created by the annihilation of three magnons of momenta $\mathbf{k}_2$, $\mathbf{k}_3$ and $\mathbf{k}_4$ by ensuring $\mathbf{k}_1 = \mathbf{k}_2 + \mathbf{k}_3 + \mathbf{k}_4$ through the Dirac delta function $\delta(\mathbf{k}_1 - \mathbf{k}_2 - \mathbf{k}_3 - \mathbf{k}_4)$. Note that the Hamiltonian in Eq. (2.15) does not give rise to three-mode interactions. In fact, a Hamiltonian

involving an odd number of mode operators is not allowed from Eq. (2.10). In other words, the Heisenberg exchange Hamiltonian does not precipitate in odd-wave interactions. However, dipole-dipole Hamiltonian can engender such interactions and this will be the subject of discussion in the subsequent section.

2.1.3 Dipole-dipole interactions

We now consider the effect of DDI interactions on the Hamiltonian in Eq. (2.1). The DDI part of the Hamiltonian is given by

$$\hat{H}_{DD} = -\frac{g^2\mu_B^2}{2}\sum_{i\neq j}\Big(\frac{\hat{\mathbf{S}}_i.\hat{\mathbf{S}}_j}{r_{ij}^3} - 3\frac{(\hat{\mathbf{S}}_i.\mathbf{n})(\hat{\mathbf{S}}_j.\mathbf{n})}{r_{ij}^3}\Big). \tag{2.19}$$

where $\mathbf{r}_{ij} = \mathbf{r}_i - \mathbf{r}_j$, $r_{ij} = |\mathbf{r}_{ij}|$ and $\mathbf{n}$ symbolizes the unit vector along $\mathbf{r}_{ij}$. Note that the DDI is a long-range interaction, palpable from Eq. (2.19). Therefore, in a large ensemble of spins, the strength of DDI could become significantly large compared to exchange interactions. Let us examine the above Hamiltonian in detail. To this end, let θ_{ij} and ϕ_{ij} be the polar angles of $\mathbf{r}_{ij}$ with the $\hat{z}$ axis aligned in the direction of B_0 in Eq. (2.1), i.e., $\mathbf{n} = (\sin\theta_{ij}\cos\phi_{ij}, \sin\theta_{ij}\sin\phi_{ij}, \cos\theta_{ij})$. Substituting it in Eq. (2.19) and rewriting the Hamiltonian in terms of the ladder operators, we obtain

$$\begin{aligned}\hat{H}_{DD} = -\frac{g^2\mu_B^2}{2}\sum_{i\neq j}\frac{1}{r_{ij}^3}\Big[(\hat{S}_i^z\hat{S}_j^z) + \frac{1}{2}(\hat{S}_i^+\hat{S}_j^- + \hat{S}_i^-\hat{S}_j^+) - 3\Big(\cos^2\theta_{ij}\hat{S}_i^zS_j^z \\ + \frac{\sin^2\theta_{ij}}{4}(\hat{S}_i^+\hat{S}_j^- + \hat{S}_i^-\hat{S}_j^+) + \frac{\sin^2\theta_{ij}}{4}(\hat{S}_i^+\hat{S}_j^+e^{-i2\phi_{ij}} + \hat{S}_i^-\hat{S}_j^-e^{i2\phi_{ij}}) + \frac{\sin\theta_{ij}\cos\theta_{ij}}{2}(\hat{S}_i^z\hat{S}_j^+e^{-i\phi_{ij}} + \hat{S}_i^z\hat{S}_j^-e^{i\phi_{ij}}) \\ \frac{\sin\theta_{ij}\cos\theta_{ij}}{2}(\hat{S}_j^z\hat{S}_i^+e^{-+i\phi_{ij}} + \hat{S}_j^z\hat{S}_i^-e^{i\phi_{ij}})\Big)\Big].\end{aligned} \tag{2.20}$$

Collecting terms, combining $\hat{H}_{DD}$, $\hat{H}_H$ and the Zeeman energy terms, we have the full Hamiltonian given by

$$\hat{H} = -\frac{J}{2}\sum_{ij}\left(\hat{S}_i^z\hat{S}_j^z + \frac{1}{4}(\hat{S}_i^+\hat{S}_j^- + \hat{S}_i^-\hat{S}_j^+)\right) - g\mu_B B_0\sum_i \hat{S}_i^z$$
$$-\frac{g^2\mu_B^2}{2}\sum_{ij}\frac{1}{r_{ij}^3}\Big(\frac{1-3\cos^2\theta_{ij}}{2}[\hat{S}_i^z\hat{S}_j^z + \frac{1}{4}(\hat{S}_i^+\hat{S}_j^- + \hat{S}_i^-\hat{S}_j^+)] - \frac{3\sin^2\theta_{ij}}{4}[\hat{S}_i^+\hat{S}_j^- e^{-i2\phi_{ij}} + h.c.]$$
$$+\frac{\sin\theta_{ij}\cos\theta_{ij}}{2}[(\hat{S}_i^z\hat{S}_j^+ + \hat{S}_j^z\hat{S}_i^+)e^{-i\phi_{ij}} + h.c.]\Big). \quad (2.21)$$

Notice that the second line of the above equation which comes from the DDI interaction gives rise to terms analogous to the exchange interactions. In contrast, the final term in Eq. (2.21) is unique i.e., purely a consequence of DDI and it is indeed the origin of three-mode interactions. We may rewrite the final term as

$$\sum_{ij}\frac{\tilde{J}_{ij}}{2}(\hat{S}_i^z\hat{S}_j^+ + \hat{S}_j^z\hat{S}_i^+) + h.c., \quad (2.22)$$

where $\tilde{J}_{ij} = -\frac{g^2\mu_B^2\sin\theta_{ij}\cos\theta_{ij}e^{-i\phi_{ij}}}{2r_{ij}^3}$. Substituting Eq. (2.7) under the large spin limit, the above equation modifies to

$$\sum_{ij}\frac{\tilde{J}_{ij}}{2}\Big[\sqrt{2S}(S-\hat{a}_i^\dagger\hat{a}_i)\hat{a}_j + \sqrt{2S}(S-\hat{a}_j^\dagger\hat{a}_j)\hat{a}_i\Big] + h.c. \quad (2.23)$$

Palpably, Eq. (2.23) in combination with Eq. (2.12) leads to the emergence of three-wave interactions.

2.2 Cavity and waveguide magnonics

Recently, magnetic systems integrated with quantum optical elements such as a resonant cavity or a waveguide have emerged as platforms to observe exotic semiclassical and quantum effects at macroscopic scales. As described in the previous section, magnons are quasi-particles, low-lying collective excitations in magnetically ordered materials like ferromagnets with wave-like charac-

teristics [88]. Thanks to their excellent tunability, these spin waves have attracted a lot of attention of late with promising applications to quantum information science. It is conspicuous from Eq. (2.1) and Eq. (2.19) that the dynamics of spatially separated spins are coupled through the effective magnetic field created by exchange, DDI or anisotropic interactions. The competition between DDI and exchange interactions determines the wavelength of the resulting spin wave. It is worth mentioning that the exchange interactions typically result in short wavelengths, whereas DDI, if dominant, produces longer wavelengths. There exists a unique mode, namely the ferromagnetic resonance (FMR) mode where the individual spins precess uniformly in phase with identical amplitude. As a result, the ensemble of spins inside a ferromagnet can be considered as one giant macroscopic spin, the dynamics of which can be controlled externally by a bias magnetic field B_0 as discussed in the preceding section. This uniform spatial mode of the ferromagnetic excitations is also known as the Kittel mode and it plays a quintessential role in integrated quantum-magnonic systems for quantum information processing.

2.2.1 Some recent developments and motivation

Magnonics in quantum optical setups has been a subject of intense experimental activity over the last few years. In particular, ferrimagnetic materials like Yttrium iron garnet (YIG) have acquired much traction among the quantum optics community. The magnetic moment of a YIG arises from the Fe^{3+} ions, wherein, two of five iron spins and the remaining three in a unit lattice orient the opposite direction providing a net spin $s = 5/2$ with a spin density that goes as $\rho \approx 4.22 \times 10^{27}$ m^{-3}. In other words, a YIG sphere of diameter $d = 1$ mm contains approximately 10^{18} spins/ m^{-3}. Note that there is damping associated with the magnetization dynamics with lifetimes shorter than state-of-the-art quantum devices. However, thanks to their high spin density, YIGs can couple strongly to microwave fields. In 2013, Hübel *et al* reported the observation of strong anti-crossing characters of a YIG coupled to waveguides. This was followed by the observation of strong coupling between a magnet and split-ring resonators. Strong coupling of magnons to microwave 3D cavities was first demonstrated by Tabuchi *et al.* [21] and Zhang *et al.* [22] in 2014. In [21], they considered a single crystal YIG sphere coupled to a rectangular microwave cavity. They demon-

strated strong magnon-photon coupling of approximately $\sim$ 50 MHz. Further, they showed that the coupling is proportional to the square root of the total number of spins inside the YIG. Normal-mode splitting was observed even in the quantum regime where the average number of thermally excited magnons and photons is approximately zero. Some other noteworthy experiments in this domain include the coupling of a superconducting qubit to magnons via microwave fields in a cavity [25], super-strong coupling etc. Note that by adjusting the size of the cavity and the YIG to improve mode matching, it is even possible to achieve ultrastrong photon-magnon coupling [89]. Some other applications of magnonics in the context of non-Hermitian quantum optics involve sensing [80], nonreciprocity [72], exceptional points (EPs) [30], level attraction [66], multistability [38, 90], dark modes[24] and many more [66–68, 70, 74]. In addition, quantum effects like entanglement and squeezing, have also been explored in such systems [31–33, 91].

Considering the topicality and experimental progress of cavity and waveguide magnonics, we have analyzed some of the interesting semiclassical and quantum phenomena ensuing from the interaction of macroscopic magnetic samples with electromagnetic fields confined in cavities and waveguides. We have used some well-known quantum optics tools like master equation [77] approach and input-output formalism [92] in our analyses. In particular, using dissipative coupling emerging from the interaction to a waveguide, we have focused on anti-$\hat{PT}$ symmetric systems, in which the magnons are coupled dissipatively to microwave fields. In the following, we expound on the mathematical formalism involving some of the basic interactions between YIG and electromagnetic fields.

2.2.2 Spin-spin interactions in a YIG

Consider the Hamiltonian of a YIG sample given by Eq. (2.1). We shall drop the DDI terms in the Hamiltonian which is negligible when compared to exchange interactions. However, in a crystal, crystal fields may give rise to anisotropies in the exchange interaction strength [37]. YIGs possess a weak nonlinearity of the order of 1 nHz due to magneto-crystalline anisotropies present in the system. Note that we have already discussed how to diagonalize a Hamiltonian of the form in Eq. (2.1). The aim of this subsection is to specifically look at the anisotropic spin-spin interactions

in the Kittel mode. Therefore, to simplify the analysis, we only keep the Zeeman and anisotropic terms in the Hamiltonian

$$\hat{H} = -\hbar\gamma_e \sum_i \mathbf{B}_0 \hat{S}_i^z + \hbar U \Big(\sum_i \hat{S}_i^z \Big)^2, \tag{2.24}$$

where U is the strength of the anisotropic interaction. It is worth exploring the origin of this anisotropic interaction Hamiltonian. When the orbital of an electron is not spherically symmetric, the energy of the state can have an orientation-dependent term, namely the anisotropic energy. One such form of anisotropy is uniaxial anisotropy, characterized by an axis which may correspond to either a minimum or maximum energy. To be precise, the axis which allows the minimum energy is called the easy axis while the axis of maximum energy is dubbed the hard axis of magnetization. To first order in correction, the anisotropic part of the energy density of the system may be expressed in terms of direction cosines as

$$W = K_{an}(1 - \cos^2\theta), \tag{2.25}$$

where K_{an} denotes the anisotropy constant, $\theta = M^z/M$, M denotes the saturation magnetization and M_z is the component of M along the $\hat{z}$ axis. Subsequently, one can obtain the $\hat{z}$ component of the anisotropic field arising from the above equation as $H_{\text{an}} = -\frac{\partial W}{\partial M^z}$ which entails an additional magnetic field $H_{\text{an}} = -2K_{\text{an}}M^z/M^2$. The corresponding anisotropic Hamiltonian is given by $\hat{H}_{an} = -\dfrac{\mu_0}{2}\int M^z(\mathbf{r})H_{\text{an}}(\mathbf{r})\mathrm{d}^3r$, where μ_0 is the magnetic permeability of the material. We are specifically interested in the Kittel mode of magnons which is a uniform spatial of the system. Therefore, we have $M^z(\mathbf{r}) = \hbar\gamma_e S^z/V_m$, where V_m is the volume of the magnetic sample and we defined the collective spin operator as $\mathbf{S} = \sum_i \hat{\mathbf{S}}_i$. Thus, we may rewrite the anisotropic Hamiltonian as $\hat{H}_{an} = \gamma_e^2 \dfrac{\hbar^2\mu_0 K_{\text{an}}}{M^2 V} S_z^2$. The Hamiltonian of the system morph into

$$\hat{H} = -\hbar\gamma_e \mathbf{B}_0 S^z + \hbar U (S^z)^2, \tag{2.26}$$

where $U = \dfrac{\hbar\mu_0\gamma_e^2 K_{\text{an}}}{M^2 V_m}$. When the number of spins in the YIG is significantly larger than the number of excitations, one can diagonalize the above Hamiltonian employing the Holstein-Primakoff transformations [85] analogous to Eq. (2.7), i.e.,

$$\begin{aligned} S_z &\simeq 5N/2 - m^\dagger m, \\ S^+ &\simeq \sqrt{5N}m, \\ S^- &\simeq \sqrt{5N}m^\dagger, \end{aligned} \tag{2.27}$$

where m symbolizes the magnon annihilation operator, N denotes the total number of spins in the YIG which typically goes as 10^{18} which is significantly greater than the magnon population $\langle m^\dagger m\rangle$. We can recast the Hamiltonian in Eq. (2.26) into

$$H/\hbar = \omega_m m^\dagger m + U(m^{\dagger 2} m^2), \tag{2.28}$$

where $\omega_m = \gamma_e B_0 - \dfrac{2S\hbar\mu_0\gamma_e^2 K_{\text{an}}}{M^2 V_m} + U$. The resulting Hamiltonian is analogous to that of an optical cavity having a Kerr nonlinearity where U is a measure of the strength of anharmonicity.

2.2.3 Magnon-photon interaction

Consider a system comprising two YIG samples of diameter $d = 1$mm placed at the maximum magnetic field of the cavity field and one of the magnets is pumped externally at frequency ω_d [38]. Note that YIGs are spin $s = \frac{5}{2}$ particles with a spin density $\rho = 4.22 \times 10^{27} m^{-3}$. The Hamiltonian of the system without the anisotropic interaction terms is given by

$$\mathscr{H} = -\int_{V_m} \mathbf{M}.\mathbf{B} d^3\mathbf{r} + \frac{1}{2}\int_{V_a} (\epsilon_0 \mathbf{E}^2 + \frac{\mathbf{B}^2}{\mu_0}) d^3\mathbf{r} - \int M_z B_0 d^3\mathbf{r} - \int \mathbf{M}\cdot\mathbf{B}_1 \, d^3\mathbf{r}. \tag{2.29}$$

The first term on the right-hand side (RHS) of Eq. 2.29 denotes the interaction between the cavity magnetic field $\mathbf{B}$ and the magnetization $\mathbf{M}$ of the YIG, integrated over the volume of the magnetic sample V_m. The second term represents the free Hamiltonian of the cavity field having a mode

volume V_a, whereas the last two terms signify, respectively, the interaction of the magnetic sample with the external bias magnetic field B_0 and the dynamical pumping field $\mathbf{B}_1$ along the y axis. In the Kittel mode of the ferromagnetic sphere, we have $\mathbf{M} = \frac{\gamma_e \hbar \mathbf{S}}{V_m}$, where γ_e is the gyromagnetic ratio and $\mathbf{S}$ the collective spin operator of the YIG. Upon quantizing the cavity field using bosonic operators and selecting a mode of frequency ω_a, the Hamiltonian of the cavity field is given by

$$\frac{1}{2}\int_{V_a}(\epsilon_0 \mathbf{E}^2 + \frac{\mathbf{B}^2}{\mu_0})d^3\mathbf{r} = \hbar\omega_a a^\dagger a, \tag{2.30}$$

where $a(a^\dagger)$ denotes the annihilation(creation) operators of the cavity field satisfying the bosonic algebra $[a, a^\dagger] = 1$. Moving on to the interaction between the magnetic sample and the cavity magnetic field, we have

$$-\int_{V_m} \mathbf{M}\cdot\mathbf{B}\ \mathrm{d}^3\mathbf{r} = -\frac{\hbar\gamma_e}{V_m}\int_{V_m} S_x B_x(\mathbf{r})\mathrm{d}^3\mathbf{r} \tag{2.31}$$

where the cavity magnetic field is assumed to be along the $\hat{x}$ axis, $S_x = \sqrt{5N/2}(m+m^\dagger)$ and $B_x(\mathbf{r}) = i\sqrt{\frac{\mu_0\hbar\omega_a}{2V_a}}\left(u(\mathbf{r})a - u^*(\mathbf{r})a^\dagger\right)$. Here, $u(\mathbf{r})$ represents spatial mode function such that $\int_{V_a}|u(\mathbf{r})|\mathrm{d}^3 r = V_a$. Employing these relations, the interaction Hamiltonian can be rewritten into

$$-\int_{V_m} \mathbf{M}\cdot\mathbf{B}\ \mathrm{d}^3\mathbf{r} = \left(ga + g^* a^\dagger\right)\left(m + m^\dagger\right) \tag{2.32}$$

where the coupling constant g is defined as $g = -i\frac{\hbar\gamma_e}{2}\sqrt{\frac{5N\mu_0\hbar\omega_a}{V_a}}\alpha$ and $\alpha = \int_{V_m} u(\mathbf{r})\mathrm{d}^3\mathbf{r}$ represents the overlap intergral. In general $S_x = \sqrt{5N/2}(mf(\mathbf{r}) + m^\dagger f^*(\mathbf{r}))$, where $f(\mathbf{r})$ denotes the spatial mode function of the magnon mode. In this case, assuming g and f to be real, the overlap integral modifies to $\alpha = \int_{V_m} u(\mathbf{r})\mathbf{f}(\mathbf{r})\mathrm{d}^3\mathbf{r}$. Conspicuously, under the rotating wave approximation (RWA), the above expression reduces to $-\int_{V_m}\mathbf{M}\cdot\mathbf{B}\ \mathrm{d}^3\mathbf{r} = \hbar(gam^\dagger + g^* a^\dagger m)$. Notice that if f and g are complex, we can absorb the phase factor associated with α into a newly defined magnon or cavity operator and treat g as a real variable. The interaction Hamiltonian in analogous to the Janes-Cummings model of two interacting harmonic oscillators.

We have already discussed the form of Zeeman interaction term in terms of the magnon operators, that is, $-\int M_z B_0 d^3\mathbf{r} = \hbar\omega_m m^\dagger m$. As mentioned earlier, the final term on the RHS of Eq. (2.29) denotes the interaction of the Kittel mode with the external drive. We have $\mathbf{B}_1 = B_1 \cos\omega_d t\hat{y}$ and therefore, $-\int \mathbf{M}\cdot\mathbf{B}_1\, d^3\mathbf{r} = \frac{i\hbar\gamma_e B_1}{4}\sqrt{5N}(m-m^\dagger)(e^{-i\omega_d}+e^{i\omega_d})$. The interaction Hamiltonian under RWA reduces to $i\hbar\Omega(me^{i\omega_d t}) - m^\dagger e^{-i\omega_d t}$, where $\Omega = \frac{\sqrt{5N}\gamma_e B_1}{4}$ is the Rabi frequency of external drive. However, one would like to rewrite the Rabi frequency in terms of the power of the laser input instead of the associated magnetic field. To this end, we consider the input plane wave oscillating at frequency ω_d and the associated Poynting vector is given by $S = \frac{\mathbf{E}_1\times\mathbf{B}_1}{\mu_0} = \frac{cB_1^2}{\mu_0}$, where c is the velocity of light. Since $S = \frac{Power}{Area}$, for a laser field applied at frequency ω_d with power P_d, we have $P_d = \frac{cB_1^2}{\mu_0}\pi r^2$, where r is the radius of the magnetic sample. Therefore, we may rewrite the interaction Hamiltonian as $\mathscr{H}/\hbar = i\Omega(m^\dagger e^{-i\omega t} - me^{i\omega t})$, where $\Omega = \frac{\gamma_e}{r}\frac{\sqrt{5N\mu_0 P_d}}{4\pi c}$. In the end, the full Hamiltonian of the coherently interacting cavity-magnon can be written as

$$H_{\text{eff}}/\hbar = \omega_a a^\dagger a + \omega_m m^\dagger m + +U(m^{\dagger 2}m^2) + g(a^\dagger m + a m^\dagger) + i\hbar\Omega\left(m^\dagger e^{-i\omega_d t} - me^{i\omega_d t}\right). \tag{2.33}$$

Note that the two modes can also interact dissipatively through a common intermediary reservoir. This interaction enters through the master equation describing the dynamics of the system and it will be the subject of discussion in subsequent chapters.

2.3 Summary

To summarize, we introduced the quantum theory of magnons and their interactions with confined electromagnetic fields. Magnons are elementary excitations in ordered magnetic systems like ferromagnets. In general, a magnetic system can have interactions of different types, including, Heisenberg exchange interactions, DDI, Zeeman interaction and anisotropic interactions. In addition, they can also couple strongly to electromagnetic fields, for example, in resonators. When the number of spins in the magnetic system significantly exceeds the number of excitations in the bulk, one can map the magnet to a system of quantized interacting harmonic oscillators. In particular, we have explicated the effect of exchange and dipolar interactions leading to the emergence

of higher-order magnon interactions. Owing to their excellent tunability and strong coupling to microwave fields, YIGs, a ferrimagnetic system have attracted a lot of attention in recent years with applications in quantum information processing. We have also reviewed the experimental and theoretical progress in the domain of cavity-magnonics involving YIGs. In the subsequent chapters, we will discuss some of our theoretical analyses of the interaction between magnetic systems and microwave fields resulting in exotic semiclassical and quantum phenomena.

3. CAVITY MEDIATED TRANSFER OF SPIN CURRENTS[1]

The exchange of energy between atoms and molecules mediated by dipole-dipole interaction (DDI) is quintessential in various branches of science. In particular, it is well known from quantum electrodynamics that the exchange of a photon can bring about DDI and thereby stimulate the transfer of excitations between atoms [93] which form the bedrock of quantum gates. However, for the DDI to be significant in free space, the atoms must be placed at a distance less than the interacting electromagnetic field. In contrast, long-range DDI between sub-systems can be established in resonant cavities, for example, the strong DDI between non-interacting qubits in a dispersive cavity [94, 95]. Note that while bulk of the precursive literature have focused on atoms and qubits, there have been experiments involving the macroscopic systems for the transfer of excitations. Of particular importance is the 2017 experiment by Bai *et al* which demonstrated the remote transfer of excitations between two macroscopic YIGs mediated by a microwave cavity in the linear domain of the dynamics of the system [29]. It is worth noting that the DDI, in general, consists of a dissipative component and recently, Xu *et al* expanded the earlier work on spin currents to the dissipative domain [70]. The experiments, however, was performed in the domain of low external pump powers and therefore does not include the effect of intrinsic anharmonicities of the magnetic system. Lately, we extended the analysis, theoretically, to include the intrinsic Kerr nonlinearities of the ferrite samples by applying a strong external pump on the YIG leading to the generation of nonlinear cavity-magnon polaritons. In the long-time limit, that is, when the mode operators describing the YIGs and the cavity have decayed into a steady state, we observed multistability in the spin current response from the YIGs. Further, we developed a spectroscopic detection scheme for the observation of multistability in the experiments through the application of a weak probe field on the cavity. The shift in polaritonic peaks of the transmitted field replicated the multistable structure of the spin currents. In 2021, our results were verified using experimental data by Dr.

[1] A major part of this chapter is reprinted with permission from *Nonlinear spin currents* by J. M. P. Nair, Z. Zhang, M. O. Scully and G. S. Agarwal, Phys. Rev. B **102**, 104415 (2020), published by the American Physical Society. Collaboration with Z. Zhang and M. O. Scully is acknowledged.

You's group in China [90].

This chapter is organized as follows. In section 3.1, we discuss the theoretical model for the nonlinear spin current and introduce basic equations for the cavity-magnon system. We write the semiclassical equations for spin current in the YIG sphere and present numerical results using a broad range of parameters in section 3.2. In section 3.3, we develop a spectroscopic detection method for the spincurrents based on the polariton frequency shift by sending a weak probe field into the cavity. We discuss the theory of nonlinear magnon polariton in the case of a single and two YIG system. Further, we numerically obtain the transmission spectra and the polariton frequency shift using experimentally attainable parameters and show the transition from bistability to multistability. We summarize our results in section 3.4.

3.1 Cavity-magnon system

We begin by considering two YIG spheres in a single-mode microwave cavity as depicted in Fig. 3.1. The dispersive spin waves haven been observed in YIG bulks, involving two distinct modes: Kittel mode and magnetostatic mode (MS) [96, 97]. The Kittel mode has a spatially uniform profile as obtained in the long wavelength limit, whereas the MS mode has finite wave number so that it has distinct frequency from the Kittel mode. The technical advance on laser control and cavity fabrication recently made the mode selection accessible. In our model, we take into account the Kittel mode strongly coupled to cavity photons, along the line of recent experiments in which the MS mode is not the one of interest. The Kittel mode is a collective spin of many electrons, associated with a giant magnetic moment, i.e., $\mathbf{M} = \gamma \mathbf{S}/V$, where $\gamma = e/m_e c$ is the gyromagnetic ratio for electron spin and $\mathbf{S}$ denotes the collective spin operator with high angular momentum. This results in the coupling to both the applied static magnetic field and the magnetic field inside the cavity, shown in Fig. 3.1. The Hamiltonian of the hybrid magnon-cavity system is

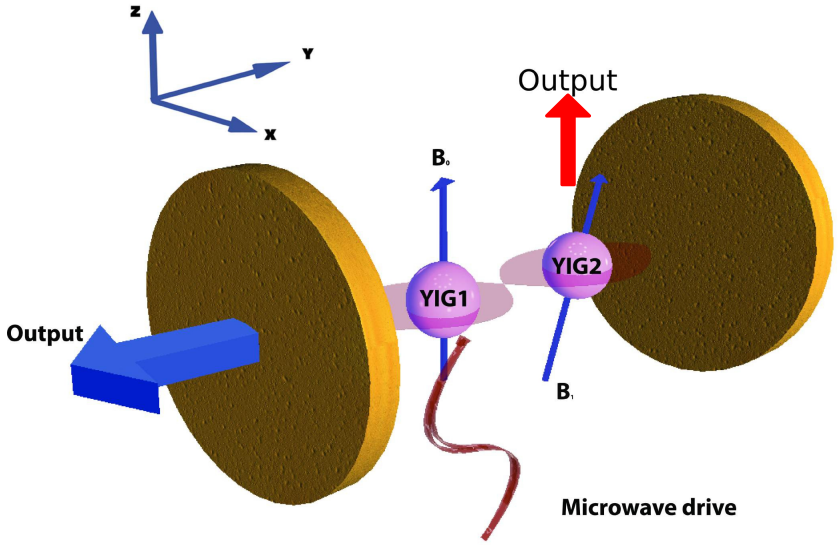

Figure 3.1: Schematic of cavity magnons. Two YIG spheres are interacting with the basic mode of the microcavity in which the right mirror is made of a high-reflection material so that photons leak from the left side. The static magnetic field producing the Kittel mode in YIG1 is along the $\hat{z}$axis, whereas the static magnetic field for YIG2 is tilted with respect to the $\hat{z}$-axis. The microwave field is along the $\hat{y}$ and the magnetic field inside the cavity is along the $\hat{x}$ axis.

$$H/\hbar = -\gamma \sum_{n=1}^{2} B_{n,0} S_{n,z} + \gamma^2 \sum_{n=1}^{2} \frac{\hbar K_{\mathrm{an}}^{(n)}}{M_n^2 V_n} S_{n,z}^2 + \omega_c a^\dagger a + \gamma \sum_{n=1}^{2} S_{n,x} B_{n,x} \tag{3.1}$$

assuming that the magnetic field in cavity is along the x axis whereas the applied static magnetic field $\mathbf{B}_0$ is along the z direction. The 2nd term in Eq. (3.1) results from the magnetocrystalline anisotropy giving the anisotropic field. We thereby assume the anisotropic field has z component only, in accordance to the experiments such that the crystallographic axis is aligned along the field $\mathbf{B}_0$. ω_c represents the cavity frequency. By means of the Holstein-Primakoff transform [85], we introduce the quasiparticle magnons described by the operators m and $m^\dagger$ with $[m, m^\dagger] = 1$. Considering the typical high spin density in the ferromagnetic material, e.g., yttrium iron garnet having diameter $d = 1$mm in which the density of the ferric iron Fe^{3+} is $\rho = 4.22 \times 10^{27} \mathrm{m}^{-3}$ that

leads to $S = \frac{5N}{2} = \frac{5}{2}\rho V = 5.524 \times 10^{18}$, the collective spin S is of much larger magnitude than the number of magnons, namely, $S \gg \langle m^\dagger m \rangle$. The raising and lowering operators of the spin are then approximated to be $S_i^+ = \sqrt{2S_i} m_i,\ S_i^- = \sqrt{2S_i} m_i^\dagger$ ($i = 1, 2$ labels the two YIGs). In the presence of the external microwave pumping, we can recast the Hamiltonian in Eq. (3.1) into

$$\begin{aligned} H_{\rm eff}/\hbar =& \omega_c a^\dagger a + \sum_{i=1}^{2} \Big[\omega_i m_i^\dagger m_i + g_i \left(m_i^\dagger a + m_i a^\dagger \right) \\ &+ U_i m_i^\dagger m_i m_i^\dagger m_i \Big] + i\Omega \left(m_1^\dagger e^{-i\omega_{\rm d} t} - m_1 e^{i\omega_{\rm d} t} \right) \end{aligned} \tag{3.2}$$

where the frequency of Kittel mode is $\omega_i = \gamma B_{i,0} - 2\hbar K_{\rm an}^{(i)} \gamma^2 S_i / M_i^2 V_i$ with $\gamma/2\pi = 28$GHz/T. $g_i = \frac{\sqrt{5}}{2}\gamma\sqrt{N} B_{\rm vac}$ gives the magnon-cavity coupling with $B_{\rm vac} = \sqrt{2\pi\hbar\omega_c/\mathrm{V}}$ denoting the magnetic field of vacuum and $U_i = K_{\rm an}^{(i)} \gamma^2 / M_i^2 V_i$ quantifies the Kerr nonlinearity. The Rabi frequency is related to input power $P_{\rm d}$ through $\Omega = \gamma \sqrt{\frac{5\pi\rho d P_{\rm d}}{3c}}$. From Eq. (3.2), we obtain the quantum Langevin equations (QLEs) for the magnon polaritons as

$$\begin{aligned} \dot{m}_1 &= -(i\delta_1 + \gamma_1) m_1 - 2iU_1 m_1^\dagger m_1 m_1 - ig_1 a + \Omega + \sqrt{2\gamma_1} m_1^{\rm in}(t) \\ \dot{m}_2 &= -(i\delta_2 + \gamma_2) m_2 - 2iU_2 m_2^\dagger m_2 m_2 - ig_2 a + \sqrt{2\gamma_2} m_2^{\rm in}(t) \\ \dot{a} &= -(i\delta_c + \gamma_c) a - i(g_1 m_1 + g_2 m_2) + \sqrt{2\gamma_c} a^{\rm in}(t) \end{aligned} \tag{3.3}$$

in the rotating frame of drive field, where $\delta_i = \omega_i + U_i - \omega_{\rm d}$ and $\delta_c = \omega_c - \omega_{\rm d}$. γ_i and γ_c represent the rates of magnon dissipation and cavity leakage, respectively. $m_i^{\rm in}(t)$ and $a^{\rm in}(t)$ are the input noise operators associated with magnons and photons, having zero mean and broad spectrum: $\langle m_i^{\rm in,\dagger}(t) m_j^{\rm in}(t') \rangle = \bar{n}_i \delta_{ij} \delta(t - t')$, $\langle m_i^{\rm in}(t) m_j^{\rm in,\dagger}(t') \rangle = (\bar{n}_i + 1)\delta_{ij}\delta(t - t')$, $\langle a^{\rm in,\dagger}(t) a^{\rm in}(t') \rangle = 0$ and $\langle a^{\rm in}(t) a^{\rm in,\dagger}(t') \rangle = \delta(t - t')$ where $\bar{n}_i = [\exp(\hbar\omega_i/k_B T) - 1]^{-1}$ is the Planck distribution.

3.2 Spin current in nonlinear magnon polaritons

Since the YIG1 is driven by a microwave field, one would expect a spin transfer towards YIG2. This results in the spin current which can be detected electronically through the magnetization of

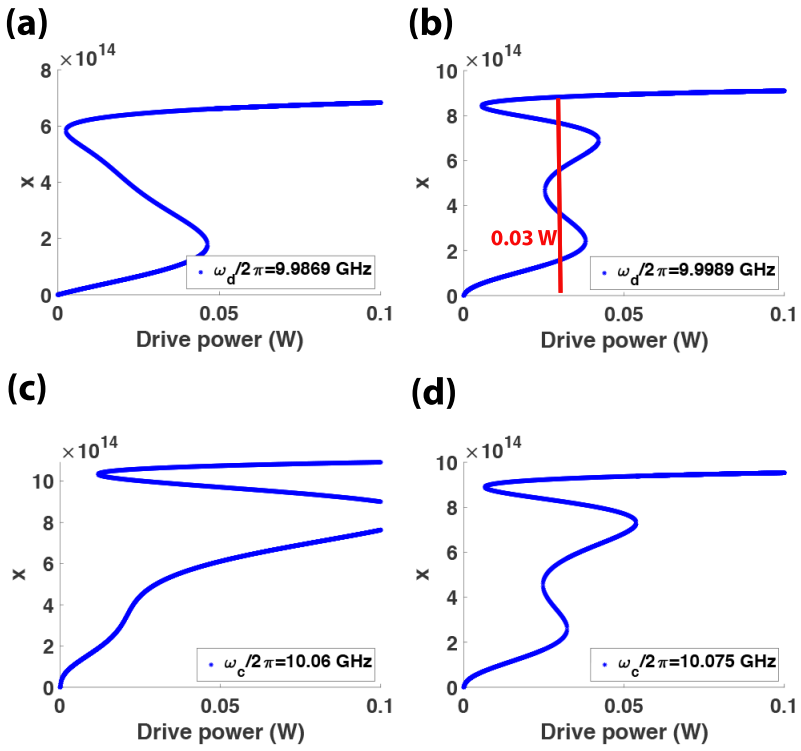

Figure 3.2: Spin current signal obtained from Eq. (3.5) illustrating bistability-multistability transition. (a,b) $\omega_c/2\pi = 10.078$GHz; (c,d) $\omega_d/2\pi = 10$GHz. Other parameters are $\omega_1/2\pi = 10.018$GHz, $\omega_2/2\pi = 9.963$GHz, $g_1/2\pi = 42.2$MHz, $g_2/2\pi = 33.5$MHz, $U_1/2\pi = 7.8$nHz, $U_2/2\pi = 42.12$nHz, $\gamma_1/2\pi = 5.8$MHz, $\gamma_2/2\pi = 1.7$MHz and $\gamma_c/2\pi = 4.3$MHz. In Fig.3.2(b), for drive power= 30mW, we observe three stable states given by $x = 1.58 \times 10^{14}$, $x = 5.6 \times 10^{14}$ and $x = 8.83 \times 10^{14}$.

the systems. Thus the spin current is determined by the quantity $\langle m_2^\dagger m_2 \rangle$, up to a constant in front. The spin migration effect has been observed in Ref.[29]. However as indicated in the introduction, the nonlinearity of the sample starts becoming important if the driving field increases. Thus we would like to understand the behavior of the spin current when the dependence on Kerr nonlinearity in Eq. (3.3) becomes important. As a first step, we will study the resulting behavior at the mean-field level, i.e., the quantum noise terms in Eq. (3.3) are essentially dropped and the decorrelation approximation is invoked when calculating the mean values of the operators. In the steady state, these mean values $\mathscr{O}^{(0)} = \langle O \rangle$ ($\mathscr{O}^{(0)} = \mathscr{M}_1, \mathscr{M}_2, \mathscr{A}; O = m_1, m_2, a$) obey the nonlinear algebraic

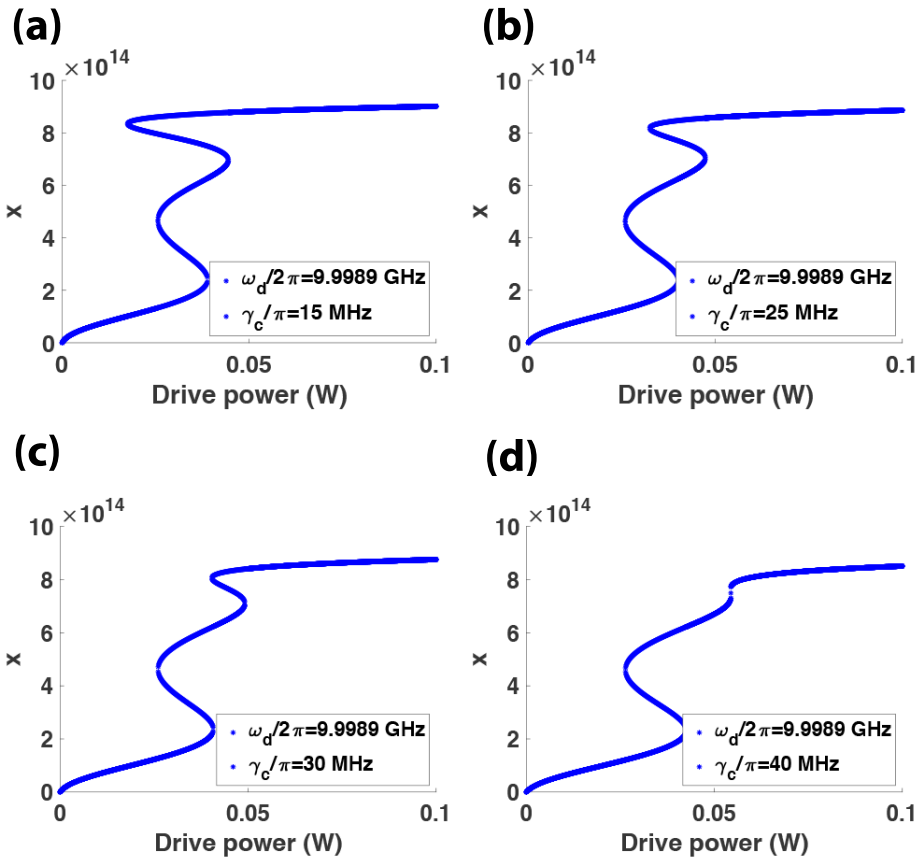

Figure 3.3: Spin current signal against drive power at different values of cavity leakage. (a) $\gamma_c < g_{1,2}$ indicates strong magnon-cavity coupling; (b,c) $\gamma_c \simeq g_{1,2}$ indicates the intermediate magnon-cavity coupling; (d) $\gamma_c > g_{1,2}$ gives rise to weak magnon-cavity coupling. $\omega_c/2\pi = 10.078$GHz, $\omega_d/2\pi = 9.998$GHz and other parameters are the same as Fig.3.2.

equations

$$
\begin{aligned}
&-(i\delta_1+\gamma_1)\mathscr{M}_1^{(0)} - 2iU_1|\mathscr{M}_1^{(0)}|^2\mathscr{M}_1^{(0)} - ig_1\mathscr{A}^{(0)} = -\Omega \\
&-(i\delta_2+\gamma_2)\mathscr{M}_2^{(0)} - 2iU_2|\mathscr{M}_2^{(0)}|^2\mathscr{M}_2^{(0)} - ig_2\mathscr{A}^{(0)} = 0 \\
&-(i\delta_c+\gamma_c)\mathscr{A}^{(0)} - i(g_1\mathscr{M}_1^{(0)} + g_2\mathscr{M}_2^{(0)}) = 0.
\end{aligned}
\tag{3.4}
$$

A manipulation of Eq. (3.4) yields the following nonlinear equation for the spin transfer, i.e., magnetization from YIG1 to YIG2 with $x \equiv |\mathscr{M}_2^{(0)}|^2$

$$\left|\left(\tilde{\delta}_1 + \frac{2U_1(\delta_c^2+\gamma_c^2)}{g_1^2 g_2^2}\left|\tilde{\delta}_2 + 2U_2 x\right|^2 x\right)\left(\tilde{\delta}_2 + 2U_2 x\right) - \frac{g_1^2 g_2^2}{(\delta_c - i\gamma_c)^2}\right|^2 x = \frac{5\pi g_1^2 g_2^2 \gamma^2 \rho d P_\mathrm{d}}{3c(\delta_c^2+\gamma_c^2)} \tag{3.5}$$

where $\tilde{\delta}_{1,2} = \delta_{1,2} - i\gamma_{1,2} - \frac{g_{1,2}^2}{\delta_c - i\gamma_c}$. We first note that in the absence of Kerr nonlinearity, the spin current reads

$$x = \frac{5\pi g_1^2 g_2^2 \gamma^2 (\delta_c^2+\gamma_c^2)\rho d}{3c|\tilde{\delta}_1\tilde{\delta}_2(\delta_c - i\gamma_c)^2 - g_1^2 g_2^2|^2} P_\mathrm{d} \tag{3.6}$$

which corresponds to the linear spin current measured in Ref. [29]. This gives rise to the linear regime with lower drive power in Fig. 3.2 and Fig. 3.3.

Fig. 3.2 depicts the spin current flowing to YIG2 against various degrees of the drive power. One can observe a smooth increase of the spin current obeying the linear law with the drive power, under the weak pumping. When the drive becomes stronger, a sudden jump of the spin current shows up, manifesting more efficient spin transfer between the two YIG spheres. When reducing the drive power, we can observe an alternative turning point, where a downhill jump of spin transfer is elaborated. By tweaking the magnon-light interaction, a bistability-multistability transition is further manifested, wherein the latter is resolved by the two cascading jumps. For instance, Fig. 3.2(a,b) elaborate such transition by increasing the frequency of the drive field. A similar transition can be observed as well through increasing the cavity frequency, shown in Fig. 3.2(c,d). It is worth noting from Fig. 3.2 that the multistability of magnon polaritons is accessible within the regime $U_1 \ll U_2$, whereas the multistable feature becomes less prominent with reducing the Kerr nonlinearity of YIG2, namely, $U_1 \sim U_2$.

So far, the results have manifested the essential role of the nonlinearity in producing the multistable nature of the spin transfer between magnon modes. Next we plot in Fig. 3.3 the robustness

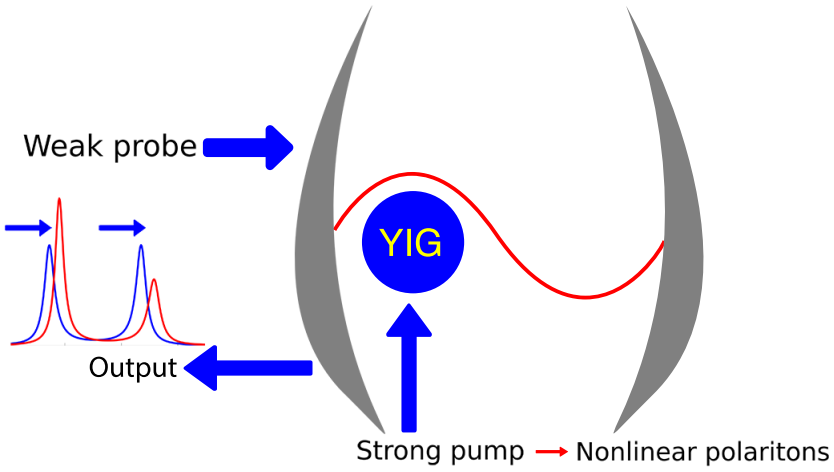

Figure 3.4: Schematic of the change in the linear transmission as increasing the driving power on the YIG sphere that activates nonlinearities of the sphere. The output spectrum exhibits shifts and asymmetries (See Fig. 3.4 for exact behaviour).

of multistability for different degrees of cavity leakage. The spin current manifests the multistable nature of magnon polaritons within a broad range of cavity leakage rates. Given the low-quality cavity where $g_{1,2} \simeq \gamma_c \gg \gamma_{1,2}$, one can still see the multistability.

Notice that the above results indicated $|\mathscr{M}_i^{(0)}|^2 \ll 2S \simeq 1.1 \times 10^{19}$ which fulfilled the condition for the validity of the effective Hamiltonian in Eq. (3.2).

3.3 Spectroscopic detection of nonlinear magnon polaritons

In order to study the physical characteristics of a system, it is fairly common to use a probe field. The response to the probe gives the system characteristics such as the energy levels, line shape and so on. We adopt a similar strategy here though we are dealing with a nonlinear & nonequilibrium system. We apply a weak probe field to the cavity and study how the transmission spectra changes with increasing drive power, see Fig.3.4. When turning off the drive, the probe transmission displays two polariton branches in the limit of strong cavity-magnon coupling. As the drive field is turned on, the nonlinearity of the YIG spheres starts entering, which results in a significant change in the transmission of the weak probe. The transmission peaks are shifted, and the transmission becomes asymmetric. To elaborate on this, we will start off with a simple case

including a single YIG sphere.

3.3.1 Nonlinearity of a single YIG as seen in probe transmission

For a single YIG sphere in a microwave cavity as considered in Ref. [1], the dynamics obeys the following equations

$$\begin{aligned}\dot{\mathscr{M}} &= -(i\delta_m + \gamma_m)\mathscr{M} - 2iU|\mathscr{M}|^2\mathscr{M} - ig\mathscr{A} + \Omega \\ \dot{\mathscr{A}} &= -(i\delta_c + \gamma_c)\mathscr{A} - ig\mathscr{M} + \mathscr{E}_p e^{-i\delta t}\end{aligned} \tag{3.7}$$

perturbed by a weak probe field at frequency ω and $\Omega_p(t) = \mathscr{E}_p e^{-i\delta t}$ + c.c., where $\mathscr{E}_p$ is the Rabi frequency of the probe field and $\delta = \omega - \omega_d$. For a notational simplicity, we have set $\mathscr{M}_1^{(0)} = \mathscr{M}$, $\delta_1 = \delta_m$, $U_1 = U$, $g_1 = g$, $\gamma_1 = \gamma_m$. The existence of nonlinear terms in Eq. (3.7) allows for the Fourier expansion of the solution such that

$$\mathscr{M}_i = \sum_{n=-\infty}^{\infty} \mathscr{M}_i^{(n)} e^{in\delta t}, \quad \mathscr{A} = \sum_{n=-\infty}^{\infty} \mathscr{A}^{(n)} e^{in\delta t} \tag{3.8}$$

where $\mathscr{M}^{(n)}$ and $\mathscr{A}^{(n)}$ are the amplitudes associated with the n-th harmonic of the probe field frequency [98]. Let $\mathscr{M}_0 \equiv \mathscr{M}^{(0)}$ and $\mathscr{A}_0 \equiv \mathscr{A}^{(0)}$ denote the zero-frequency component, giving the steady-state solution when turning off the probe field. Inserting these into Eq. (3.7), one can find the linearized equations for the components $\mathscr{M}_\pm \equiv \mathscr{M}^{(\mp 1)}$ and $\mathscr{A}_\pm \equiv \mathscr{A}^{(\mp 1)}$

$$\begin{aligned}&(\Delta - \delta)\mathscr{M}_+ + 2U\mathscr{M}_0^2\mathscr{M}_-^* + g\mathscr{A}_+ = 0 \\ &2U\mathscr{M}_0^2\mathscr{M}_+^* + (\Delta + \delta)\mathscr{M}_- + g\mathscr{A}_- = 0 \\ &g\mathscr{M}_+ + (\Delta_c - \delta)\mathscr{A}_+ = -i\mathscr{E}_p \\ &g\mathscr{M}_- + (\Delta_c + \delta)\mathscr{A}_- = 0, \\ &\Delta = \delta_m + 4U|\mathscr{M}_0|^2 - i\gamma_m, \quad \Delta_c = \delta_c - i\gamma_c\end{aligned} \tag{3.9}$$

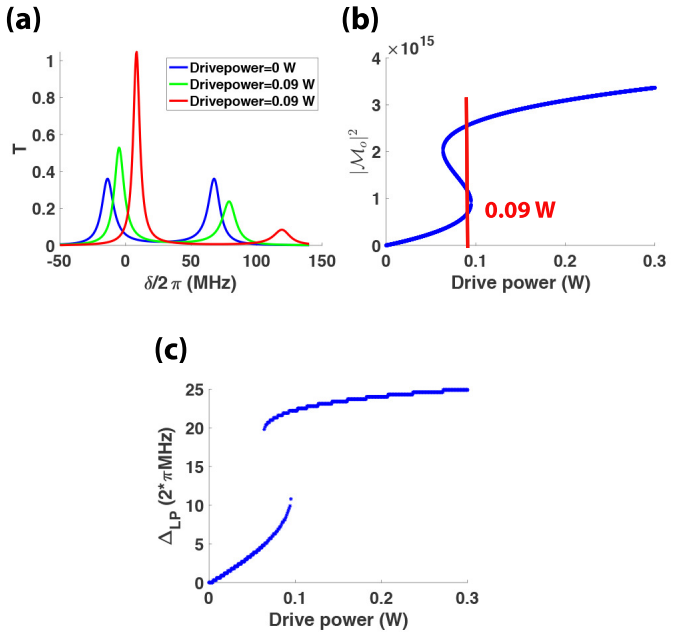

Figure 3.5: (a) Transmission spectrum for a single YIG in a single-mode microwave cavity, as a function of scanning probe frequency, according to Eq. (3.12). Blue line is for the case when turning off the drive field. Figure 3.5(b) depicts the spin polarization against the drive power. We observe that, for drive power = 90mW, there are two stable states at $|\mathscr{M}^{(0)}|^2 = 0.66 \times 10^{15}$ and $|\mathscr{M}^{(0)}|^2 = 2.55 \times 10^{15}$. The green and red lines in Fig. 3.5(a) are for the same bistable states with input power $P_{\rm d} = 90$mW. Figure 3.5(c) depicts the frequency shift of the lower polariton peak as a function of drive power. Parameters are $\omega_c/2\pi = 10.025$GHz, $\omega_m/2\pi = 10.025$GHz, $\omega_{\rm d}/2\pi = 9.998$GHz, $g/2\pi = 41$MHz, $U/2\pi = 8$nHz, $\gamma_m/2\pi = 17.5$MHz and $\gamma_c/2\pi = 3.8$MHz, taken from recent experiments [1].

which yields to

$$\mathscr{A}_+ = \frac{\mathscr{E}_p}{i(\Delta_c - \delta)}\left[1 + \frac{g^2}{(\Delta_c - \delta)v}\right] \tag{3.10}$$

where

$$v = \Delta - \delta - \frac{g^2}{\Delta_c - \delta} - \frac{4U^2(\Delta_c^* + \delta)|\mathscr{M}_0|^2}{(\Delta_c^* + \delta)(\Delta^* + \delta) - g^2}. \tag{3.11}$$

Eq. (3.10) defines the 1st-order response function and hence the complex transmission amplitude is given by

$$T(\delta) = -\frac{i}{\Delta_c - \delta}\left[1 + \frac{g^2}{(\Delta_c - \delta)v}\right] \tag{3.12}$$

which leads to the polariton frequency

$$\delta^2 = \frac{1}{2}\Big[(\delta_m + 4U|\mathscr{M}_0|^2)^2 + \delta_c^2 + 2g^2 - 4U^2|\mathscr{M}_0|^2 \pm \sqrt{\mathscr{F} + 16U^2\delta_c^2|\mathscr{M}_0|^2}\Big] \tag{3.13}$$

with

$$\mathscr{F} = \Big((\delta_m + 4U|\mathscr{M}_0|^2 - \delta_c)^2 + 4g^2 - 4U^2|\mathscr{M}_0|^2\Big) \times \Big((\delta_m + 4U|\mathscr{M}_0|^2 + \delta_c)^2 - 4U^2|\mathscr{M}_0|^2\Big). \tag{3.14}$$

For a given drive power, we calculate $|\mathscr{M}_0|^2$ from Eq. (3.7) and insert this value into Eq. (3.12) to obtain the transmission amplitude. The peak positions are given by Eq. (3.13). We plot the transmission spectrum in Fig. 3.5(a), employing the experimentally feasible parameters [1]. It shows the Rabi splitting between the two polariton branches at zero input power. As the input power is switched on, the peak shift can be considerably observed, resulting from the Kerr nonlinearity, as predicted from Eq. (3.13). For a given drive power, the lower and higher polaritons correspond to the lowest and highest energy peaks of the transmission spectra at frequencies ω_{LP} and ω_{HP} respectively. This is further illustrated in Fig. 3.5(b), where the two stable states are observed at $P_{\mathrm{d}} = 90\mathrm{mW}$. Fig. 3.5(c) depicts the frequency shift of the peak of lower polariton as a function of input power, and the bistability of the magnon polaritons is therefore evident. Here the frequency shift of lower polariton is defined by $\Delta_{\mathrm{LP}} \equiv \omega_{\mathrm{LP}} - \omega_{\mathrm{LP}}^0$ with ω_{LP}^0 giving the lower polariton frequency in the absence of Kerr nonlinearity.

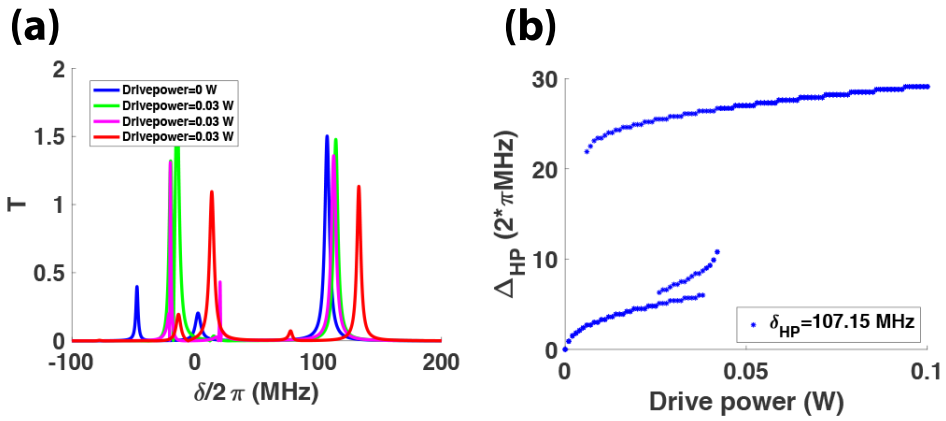

Figure 3.6: (a) Transmission spectrum for two YIG in a microwave cavity, as scanning probe frequency, according to Eq. (3.21). The blue line is for the case without driving, while green, black and red lines are for triple states with input power $P_{\rm d} = 30$mW. They represent the same three stable states described in Fig. 3.2(b). (b) Frequency shift associated with upper polariton peak, where $\delta_{\rm HP} = \omega_{\rm HP} - \omega_{\rm d}$. Other parameters are $\omega_c/2\pi = 10.078$GHz, $\omega_1/2\pi = 10.018$GHz, $\omega_2/2\pi = 9.963$GHz, $\omega_{\rm d}/2\pi = 9.998$GHz, $g_1/2\pi = 42.2$MHz, $g_2/2\pi = 33.5$MHz, $U_1/2\pi = 7.8$nHz, $U_2/2\pi = 42.12$nHz, $\gamma_1/2\pi = 5.8$MHz, $\gamma_2/2\pi = 1.7$MHz and $\gamma_c/2\pi = 4.3$MHz.

3.3.2 Detection of multistability in spin current via probe transmission

For two YIG spheres interacting with a single-mode cavity, we obtain the following equations for the system perturbed by a probe field

$$\begin{aligned}
\dot{\mathscr{M}}_1 &= -(i\delta_1 + \gamma_1)\mathscr{M}_1 - 2iU_1|\mathscr{M}_1|^2\mathscr{M}_1 - ig_1\mathscr{A} + \Omega \\
\dot{\mathscr{M}}_2 &= -(i\delta_2 + \gamma_2)\mathscr{M}_2 - 2iU_2|\mathscr{M}_2|^2\mathscr{M}_2 - ig_2\mathscr{A} \\
\dot{\mathscr{A}} &= -(i\delta_c + \gamma_c)\mathscr{A} - i(g_1\mathscr{M}_1 + g_2\mathscr{M}_2) + \mathscr{E}_p e^{-i\delta t}.
\end{aligned} \tag{3.15}$$

Applying the Fourier expansion technique given in Eq. (3.8), we find the linearized equations for the components associated with the harmonic $e^{\pm i\delta t}$

$$\begin{aligned}
&(\Delta_1 - \delta)\mathscr{M}_{1,+} + 2U_1\mathscr{M}_{1,0}^2\mathscr{M}_{1,-}^* + g_1\mathscr{A}_+ = 0\\
&2U_1\mathscr{M}_{1,0}^2\mathscr{M}_{1,+}^* + (\Delta_1 + \delta)\mathscr{M}_{1,-} + g_1\mathscr{A}_- = 0\\
&(\Delta_2 - \delta)\mathscr{M}_{2,+} + 2U_2\mathscr{M}_{2,0}^2\mathscr{M}_{2,-}^* + g_2\mathscr{A}_+ = 0\\
&2U_2\mathscr{M}_{2,0}^2\mathscr{M}_{2,+}^* + (\Delta_2 + \delta)\mathscr{M}_{2,-} + g_2\mathscr{A}_- = 0\\
&g_1\mathscr{M}_{1,+} + g_2\mathscr{M}_{2,+} + (\Delta_c - \delta)\mathscr{A}_+ = -i\mathscr{E}_p\\
&g_1\mathscr{M}_{1,-} + g_2\mathscr{M}_{2,-} + (\Delta_c + \delta)\mathscr{A}_- = 0
\end{aligned} \tag{3.16}$$

which can be easily solved by matrix techniques. Equation (3.16) can reduce to two linear equations with two unknowns

$$\begin{pmatrix} v_{11} & v_{12} \\ v_{21} & v_{22} \end{pmatrix} \begin{pmatrix} \mathscr{M}_{1,+} \\ \mathscr{M}_{2,+} \end{pmatrix} = i\mathscr{E}_p \begin{pmatrix} \alpha_1 \\ \alpha_2 \end{pmatrix} \tag{3.17}$$

with the coefficients

$$
\begin{aligned}
v_{11} &= \Delta_1 - \delta - \frac{g_1^2}{\Delta_c - \delta} + \frac{U_1 \mathscr{M}_{1,0}^2}{U_2 \mathscr{M}_{2,0}^2} \\
&\quad \times \frac{g_1^2 g_2^2 - 4U_1 U_2 (\Delta_c^* + \delta)(\Delta_c - \delta) \mathscr{M}_{1,0}^{*,2} \mathscr{M}_{2,0}^2}{(\Delta_c - \delta)[(\Delta_c^* + \delta)(\Delta_c + \delta) - g_1^2]} \\
v_{12} &= \frac{g_1 g_2}{\Delta_c - \delta} \left[\frac{U_1 \mathscr{M}_{1,0}^2}{U_2 \mathscr{M}_{2,0}^2} \frac{g_2^2 - (\Delta_c - \delta)(\Delta_2 - \delta)}{(\Delta_c^* + \delta)(\Delta_1^* + \delta) - g_1^2} - 1 \right] \\
v_{21} &= \frac{g_1 g_2}{\Delta_c - \delta} \left[\frac{U_2 \mathscr{M}_{2,0}^2}{U_1 \mathscr{M}_{1,0}^2} \frac{g_1^2 - (\Delta_c - \delta)(\Delta_1 - \delta)}{(\Delta_c^* + \delta)(\Delta_2^* + \delta) - g_2^2} - 1 \right] \\
v_{22} &= \Delta_2 - \delta - \frac{g_2^2}{\Delta_c - \delta} + \frac{U_2 \mathscr{M}_{2,0}^2}{U_1 \mathscr{M}_{1,0}^2} \\
&\quad \times \frac{g_1^2 g_2^2 - 4U_1 U_2 (\Delta_c^* + \delta)(\Delta_c - \delta) \mathscr{M}_{1,0}^2 \mathscr{M}_{2,0}^{*,2}}{(\Delta_c - \delta)[(\Delta_c^* + \delta)(\Delta_c + \delta) - g_2^2]}
\end{aligned}
\tag{3.18}
$$

and

$$
\begin{aligned}
\alpha_1 &= \frac{g_1}{\Delta_c - \delta} \left[1 - \frac{U_1 \mathscr{M}_{1,0}^2}{U_2 \mathscr{M}_{2,0}^2} \frac{g_2^2}{(\Delta_c^* + \delta)(\Delta_1^* + \delta) - g_1^2} \right] \\
\alpha_2 &= \frac{g_2}{\Delta_c - \delta} \left[1 - \frac{U_2 \mathscr{M}_{2,0}^2}{U_1 \mathscr{M}_{1,0}^2} \frac{g_1^2}{(\Delta_c^* + \delta)(\Delta_2^* + \delta) - g_2^2} \right]
\end{aligned}
\tag{3.19}
$$

where $\Delta_j = \delta_j + 4U_j |\mathscr{M}_{j,0}|^2 - i\gamma_j;\ j = 1, 2$. Note that $\mathscr{M}_{1,0}$ and $\mathscr{M}_{2,0}$ are to be obtained from Eq. (3.4). Solving for $\mathscr{A}_+$ we find, with relatively little effort

$$
\mathscr{A}_+ = \frac{\mathscr{E}_p}{i(\Delta_c - \delta)} \left[1 + \frac{(g_1 v_{22} - g_2 v_{21})\alpha_1 - (g_1 v_{12} - g_2 v_{11})\alpha_2}{v_{11} v_{22} - v_{12} v_{21}} \right] \tag{3.20}
$$

which leads to the transmission amplitude

$$
T(\delta) = -\frac{i}{\Delta_c - \delta} \left[1 + \frac{(g_1 v_{22} - g_2 v_{21})\alpha_1 - (g_1 v_{12} - g_2 v_{11})\alpha_2}{v_{11} v_{22} - v_{12} v_{21}} \right]. \tag{3.21}
$$

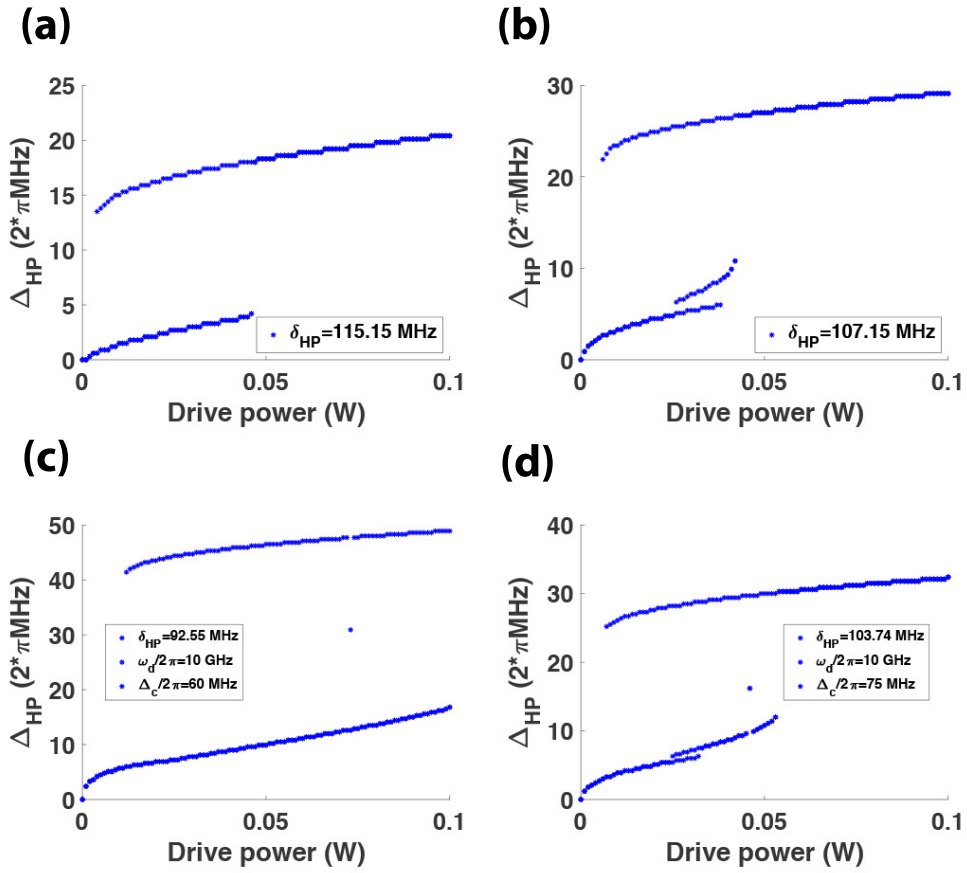

Figure 3.7: Transition between bistability and multistability. (a) $\omega_c/2\pi = 10.078$GHz, $\omega_{\rm d}/2\pi = 9.9909$GHz and (b) $\omega_c/2\pi = 10.078$GHz, $\omega_{\rm d}/2\pi = 9.9989$GHz; (c) $\omega_c/2\pi = 10.06$GHz, $\omega_{\rm d}/2\pi = 10$GHz and (d) $\omega_c/2\pi = 10.075$GHz, $\omega_{\rm d}/2\pi = 10$GHz. Other parameters are the same as Fig. 3.2.

The information on the dispersion relation of nonlinear magnon polaritons is contained in Eq. (3.21).

Fig. 3.6(a) illustrates the transmission spectra of the hybrid magnon-cavity systems under various input powers. Here we have taken into account the experimentally feasible parameters $\omega_c/2\pi = 10.078$GHz, $\omega_1/2\pi = 10.018$GHz, $\omega_2/2\pi = 9.963$GHz, $\omega_{\rm d}/2\pi = 9.998$GHz, $g_1/2\pi = 42.2$MHz, $g_2/2\pi = 33.5$MHz, $U_1/2\pi = 7.8$nHz, $U_2/2\pi = 42.12$nHz, $\gamma_1/2\pi = 5.8$MHz, $\gamma_2/2\pi = 1.7$MHz, $\gamma_c/2\pi = 4.3$MHz [90]. First of all we observe at very weak input power three

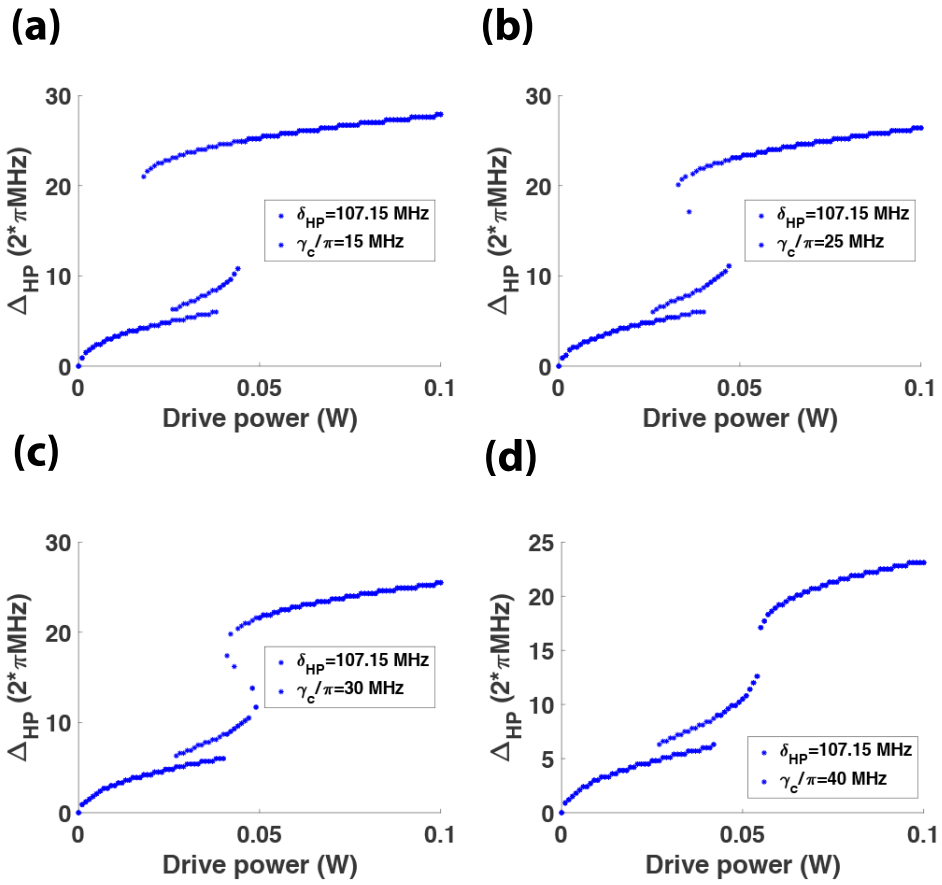

Figure 3.8: Frequency shift of upper polariton against input power at different values of cavity leakage. (a) $\gamma_c < g_{1,2}$ indicates strong magnon-cavity coupling; (b,c) $\gamma_c \simeq g_{1,2}$ indicates the intermediate magnon-cavity coupling; (d) $\gamma_c > g_{1,2}$ gives rise to weak magnon-cavity coupling. All the parameters are same as Fig.3.3.

distinct peaks positioned at the same frequencies as the polariton branches, termed as lower (LP), intermediate (MP) and higher polaritons (HP) in an ascending order of energy. With increasing input power, the peak shift of magnon polaritons can be observed from the transmission spectra, where the frequency shifts associated with the polariton states are defined by $\Delta_\sigma = \omega_\sigma - \omega_\sigma^0$; σ =LP, MP and HP, respectively, where ω_σ^0 denotes the polariton frequency with no nonlinearity. This shift is attributed to the Kerr nonlinearity given by the term $U_1|\mathscr{M}_1|^4 + U_2|\mathscr{M}_2|^4$ which is greatly enhanced as the strong drive creates large magnon number. Since the weak Kerr nonlinearity in

real ferromagnetic materials would lead to tiny frequency shift only, we essentially plot the polariton frequency shift as a function of input power. The net hysteresis loop is thereby monitored through the frequency shift of the higher polariton, ranging from 0 to 30MHz, shown in Fig. 3.6(b). The same trends can be also demonstrated for the frequency shift of lower polariton, which will be presented elsewhere. The multistability can then be clearly manifested by means of the two cascading jumps of frequency shift with increasing input power. More interestingly as shown in Fig.3.7, the bistability-multistability transition in magnon polaritons is revealed through tweaking either the frequency of microwave drive (upper row of Fig. 3.7) or the cavity-magnon detuning (lower row of Fig. 3.7). Within the parameter regimes feasible for experiments, the two magnon system shows in Fig. 3.7(a,c) the bistability that has been claimed in a single magnon in recent experiments [1]. By either increasing drive or cavity frequency, the multistable feature is further observed as depicted in Fig. 3.7(b,d).

Fig. 3.8 shows the robustness of multistability in magnon polaritons, against the cavity leakage. Clearly, the multistability becomes weaker when using the worse cavity. Indeed, the revisit of the hysteresis curves indicates that the multistability may be achieved, even with lower-quality cavity giving rise to intermediate magnon-cavity coupling, where $g_{1,2} \simeq \gamma_c \gg \gamma_{1,2}$ yields to Fig. 3.8(b,c). This regime is crucial for detecting the multistability and spin dynamics of magnons used in Ref.[1, 29], in that a spectrometer is desired to read out the photons imprinting the magnon states information. The photons leaking from the cavity will then undergo a Fourier transform through the grating attached to the detector. This scheme requires the much larger cavity leakage than the magnon dissipation, namely, $\gamma_c \gg \gamma_{1,2}$, so that the magnon states remain almost unchanged when reading off the photons from the cavity.

3.4 Summary

To summarize, we have studied the photon-mediated nonlinear spin migration between massive ferromagnetic materials. Owing to the Kerr nonlinearity coming from the magnetocrystalline anisotropy, the multistability in the spin current between the two YIG spheres was demonstrated. Strong external pump powers of magnitude $\approx 0.1\mu$W were used and this goes beyond the linear

regime of spin transfer studied before. We further developed a spectroscopic detection scheme for resolving the spin polarization migration, through the response of nonlinear magnon polaritons to the external probe field. Employing a broad range of experimentally realizable parameters, we showed that the spin current as a distinct signal of detection produced results in perfect agreement with the transmission spectrum, demonstrating, for instance, the bistability-multistability transition in magnon polaritons. The multistability is surprisingly robust against cavity leakage: the multistable nature may persist with a low-quality cavity giving intermediate magnon-cavity coupling. This may be helpful in probing the multistable effect in real experiments.

It is worth noting that the developed formalism and the accompanying results in this chapter would apply to various kinds of systems. In particular, our approach for multistability in magnons may be potentially extended to condensed-phase polyatomic molecules and molecular clusters, along with the fact of similar forms of nonlinear couplings $Ub^{\dagger}bb^{\dagger}b$ and $b^{\dagger}bq$ where b is the annihilation operator of excitons and q denotes the nuclear coordinate. Moreover, the energy-transfer protocol could be applied to systems of atoms, superconducting qubits and quantum dots, trapped ions, and spin ensembles. Likewise, nonlinear effects such as bistability would also be reinforced on account of the parametrically induced coherences.

4. QUANTUM AMPLIFICATION OF ENERGY-TRANSFER IN CAVITY MAGNONICS BY A PARAMETRIC DRIVE INDUCED LONG-LIVED MODE[1]

Photon-mediated interactions are a quintessential resource in various branches of science. A prime example is the well-known dipole-dipole interaction (DDI), which, according to quantum electrodynamics, arises from the exchange of a photon [77] between two atoms. The DDI consists, in general, of a dissipative component as well which can vanish at a certain separation of the dipoles. This DDI determines the energy/excitation transfer [99, 100] between, say, the donor and the acceptor molecules, and is of paramount importance in the generation of quantum gates [13, 101]. It is therefore desirable to have a mechanism which can control and potentially improve such an interaction. One routine technique is to use high-quality cavities and employ large coupling between the cavity photons [102–104]. A natural question then arises - can one further improve the cavity-mediated energy transfer which would be instrumental to the realization of quantum-enhanced fundamental interactions and the development of sophisticated quantum machines and networks?

In this chapter, we provide a definite answer to this question and demonstrate the possibility of enhancing the photon-mediated transfer of excitations. Guided by the developments in quantum metrology using squeezed states [105–109], we propose to use parametric interactions, which give rise to squeezed states of matter and light, to enhance the cavity-mediated transfer of excitations. We would specifically apply the idea in the context of cavity magnonics [1, 20–22, 34, 110] and show significant amplification of the photon-mediated transfer of spin currents between magnetic samples [29] by using parametric interactions in cavities. We show that parametric interactions can produce long-lived modes like BIC which result in substantial enhancement of the spin currents. We note that many other applications of parametric interactions have appeared in literature:

[1] A major part of this chapter is reprinted with permission from *Quantum amplification of spin currents in cavity magnonics by a parametric drive induced long-lived mode* by D. Mukhopadhyay, J. M. P. Nair and G. S. Agarwal, Phys. Rev. B **106**, 184426 (2022), published by the American Physical Society. Collaboration with D. Mukhopadhyay is acknowledged.

enhanced cooling [54]; exponentially enhanced spin-cavity photon coupling [55, 56]; enhanced phonon-mediated spin-spin coupling in a system of spins coupled to a cantilever [57]; possibility of first order superradiant phase transitions [58]; enhancement in the generation of entangling gates [59]; amplification of small displacements of trapped ions [60].

Here, we focus on cavity magnonics involving the coupling of high-quality microcavities and YIG spheres. These systems are attracting increasing attention [23, 24, 26] as favorable candidates to observe various semiclassical [30, 35, 66, 67, 70, 72, 74, 81, 82] and quantum phenomena [25, 27, 32, 91] at the macroscopic level. Some of the key developments include the coupling of magnons to a superconducting qubit [25] and phonons [27], microwave-to-optical interconversion [35, 82], exceptional points [30], entanglement [32, 91] and many more. One of the remarkable signatures of such a coupling was the observation of a cavity-mediated transfer of spin excitations [29]. Two YIG samples were placed at the opposite ends of a microwave cavity and by manipulating the cooperativity of one of them, researchers could detect the modifications in the magnon population, namely, the spin current of the other. Here we demonstrate how the photon-mediated transfer of spin-wave excitations can be significantly boosted by a two-photon parametric drive applied to the cavity. The parametric interaction could be produced either from a $\chi^{(2)}$-type or $\chi^{(3)}$-type nonlinearity. By coherently pumping one of the samples, we probe modifications to the steady-state magnon occupancy in the neighbouring sample as a function of the parametric drive strength. Our analysis showcases the emergence of parametrically induced coherences characterized by a long-lived mode leading to precipitous enhancement in the spin current response. The enhancement can be extraordinarily large around the two-photon resonance condition $\omega_d = \omega_p/2$, where ω_d and ω_p are the frequencies of the magnon drive and the parametric pump field respectively. This phenomenon is brought to bear by the cumulative effect of two-photon-excitation events. The cascaded absorption of photons by the concerned magnon mode opens up higher-order transition pathways within the magnon Fock space. The fact that magnificent enhancement factors can be achieved even within the permissible stable regime of the nonlinear dynamics underscores the utility of this scheme. The analysis presented in this letter is generic, and pertinent to a wide class

of systems with a parametrically driven component. This is because energy transfer is ubiquitous. The investigated paradigm would apply, for example, to nonlinear Kerr boson systems driven far from equilibrium [111].

4.1 Amplified spin currents

To set the stage, we shortly recapitulate the problem of two spatially separated macroscopic ferrite samples of YIG coupled to the microcavity field. Owing to an effective cavity-mediated coupling between the two spheres, an external driving field applied to the first YIG sample would elicit a spin current from the second one. The system Hamiltonian, in the reference frame of the driving field, assumes the form [1, 37]

$$\mathscr{H}_0/\hbar = \Delta_c a^\dagger a + \sum_{j=1}^{2} \Delta_j m_j^\dagger m_j + \sum_{j=1}^{2} g_j [a^\dagger m_j + a m^\dagger] + i\Omega(m_1^\dagger - m_1), \tag{4.1}$$

where a is the annihilation operator representing the cavity, $\Delta_c = \omega_c - \omega_d$ is the cavity detuning, m_1, m_2 are the two Kittel modes representing magnonic excitations in the two samples, and $\Delta_1 = \omega_1 - \omega_d$, $\Delta_2 = \omega_2 - \omega_d$ the respective detunings. For each j, the parameter $g_j = (\sqrt{5}/2)\gamma_e \sqrt{N_j} B_{\text{vac}}$ denotes the coherent magnon-photon interaction strength, with γ_e being the gyromagnetic ratio, $B_{\text{vac}} = \sqrt{\dfrac{\mu_0 \hbar \omega_c}{2V_c}}$ the magnetic field of vacuum, and N_j the total number of spins in the sample. Plus, $\Omega = \dfrac{\gamma_e}{2}\sqrt{\dfrac{5\mu_0 \rho_1 d_1 D_p}{3c}}$ is the Rabi frequency of the applied drive, where ρ_1 and d_1 are the respective spin density and diameter of the first sample, while D_p is incident power of the applied drive. To understand this transfer of spin-wave excitations at the level of transitions among energy levels, we note that in the absence of the extrinsic magnon drive, the Hamiltonian is excitation-preserving, with only an oscillatory energy transfer between the magnon and the cavity modes. Now let us label the eigenstates of the noninteracting system as $|n_a, n_1, n_2\rangle$, where n_a, n_1 and n_2 indicate populations of the cavity and the two magnon modes respectively. If a weak coherent drive (at the single-photon level) on m_1 excites the system into the state $|0, 1, 0\rangle$, energy would

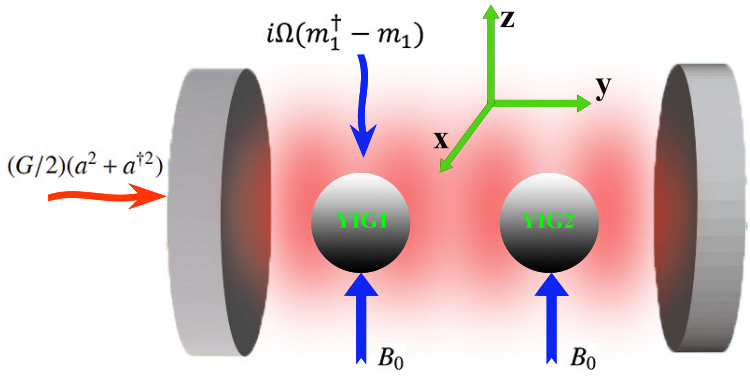

Figure 4.1: Schematic of two ferrimagnetic samples of YIG, coherently coupled to a single-mode cavity, which is driven externally by a two-photon parametric drive. A uniform bias magnetic field B_0 applied to either of the YIG spheres generates the corresponding Kittel mode and the YIG1 is driven externally by a coherent drive of low photon occupancy.

be exchanged back and forth among the energy levels $|0,1,0\rangle$, $|1,0,0\rangle$, and $|0,0,1\rangle$, provided the dissipation is negligible. The transfer happens via the pathway $|0,1,0\rangle \rightarrow |1,0,0\rangle \rightarrow |0,0,1\rangle$, and this simple scheme can be easily extended to the case of coherent drives.

We now demonstrate the impact of a parametric drive applied to the cavity on the associated transfer efficiency in the system considered above. Precisely, we would be leveraging the potential of parametrically enhanced spin-photon interactions to amplify the spin currents from magnetic samples loaded into a cavity resonator. The new schematic is portrayed in Fig. 4.1, where the cavity field is now parametrically driven. The preceding Hamiltonian has to be supplemented by an additional contribution of the form $\mathscr{H}_\mathrm{p}/\hbar = (G/2)(a^2 + a^{\dagger 2})$, so that the Hamiltonian for the parametric system [55, 56, 58] would be given by $\mathscr{H} = \mathscr{H}_0 + \mathscr{H}_\mathrm{p}$. To quell the time-dependence of the Hamiltonian, the frequency of the applied magnon drive ω_d has been set equal to $\omega_p/2$. Our objective is to investigate the steady-state spin-current response from the second YIG. Under the semiclassical approximation, the dynamical equations for the mode amplitudes at the level of mean fields can be obtained from the master equation of the system. These equations can be condensed

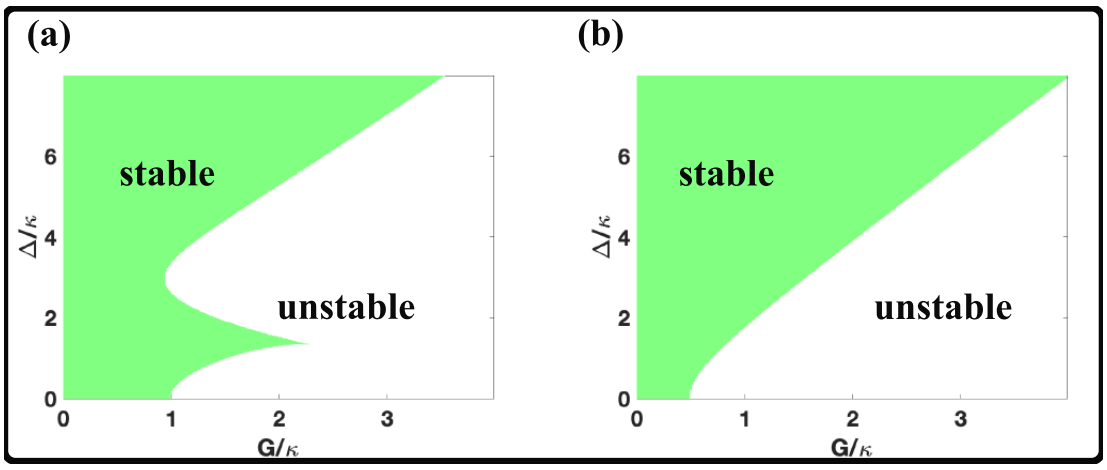

Figure 4.2: Phase diagram highlighting the region of stable dynamics for (a) the three-mode cavity-magnon system considered in this letter, and (b) a parametrically driven single-mode cavity without any coupled accessories.

in the form of a 6 × 6-matrix-differential equation

$$\dot{X} = -iH_{\text{eff}}X + \Omega F_{\text{in}}, \tag{4.2}$$

where $X = (a\ m_1\ m_2\ a^\dagger\ m_1^\dagger\ m_2^\dagger)^T$, $H_{\text{eff}} = \begin{pmatrix} H_{\text{eff}}^{(0)} & J \\ -J & -H_{\text{eff}}^{*(0)} \end{pmatrix}$ is a 6 × 6 coupling matrix, and $F_{\text{in}} = (0\ 1\ 0\ 0\ 1\ 0)^T$. The expectation-value notations $\langle . \rangle$ have been dropped for brevity. The constituent block elements of H_{eff} are given by $H_{\text{eff}}^{(0)} = \begin{pmatrix} \Delta_c - i\kappa & g_1 & g_2 \\ g_1 & \Delta_1 - i\gamma_1 & 0 \\ g_2 & 0 & \Delta_2 - i\gamma_2 \end{pmatrix}$ and $J = \begin{pmatrix} G & 0 & 0 \\ 0 & 0 & 0 \\ 0 & 0 & 0 \end{pmatrix}$, where $2\kappa, 2\gamma_1, 2\gamma_2$ are the respective relaxation rates of the cavity mode and the two magnon modes. Thus $H_{\text{eff}}^{(0)}$ denotes the coupling matrix in the absence of the parametric drive, i.e., with G set equal to 0. Eq. (4.2) would permit a steady-state solution insofar as the eigenmodes of H_{eff} have decaying character. Subject to this assumption, the steady-state spin-current response from the second magnetic sample could be expressed as $\mathscr{M} = |m_2|^2$, wherein $m_2 = \sum_{j=2,5} \left[-iH_{\text{eff}}^{-1} \right]_{2j} \Omega$.

To keep the analysis straightforward, we henceforth work with the assumption that $\Delta_1 = \Delta_2 = \Delta_c = \Delta$, $\kappa = \gamma_1 = \gamma_2 = \gamma$, and $g_1 = g_2 = g$. As was just stated, the stability of the steady

state hinges on the imaginary parts of the eigenvalues, which we label as λ_i's. This is formally equivalent to the Routh-Hurwitz criterion for the stability of nonlinear dynamics. The stable and the unstable regimes for this parametric model are numerically plotted in Fig. 4.2(a), for the ratio $g/\kappa = 2$, with the demarcating partition between the two identified by the equality $\mathrm{Im}(\lambda_i) = 0$ for *at least* one λ_i. Commensurately, there exists a critical parametric coupling strength $G_c(\Delta)$ below which the dynamics is stable. Contrast this with the corresponding stable regime obtained in the absence of magnons, i.e., $g = 0$, which is juxtaposed for reference in Fig. 4.2(b). Not only does the magnon-photon coupling skew the stablity criterion, it does so in a highly nontrivial fashion. The effect is clearly not monotonic in Δ. It can also be shown that the stability criterion does not depend on the two-photon detuning $\delta = \omega_d - \omega_p/2$ and the same phase diagram would apply to the case of non-zero detuning.

In order to capture the effect of the parametric drive, we introduce a dimensionless parameter F that embodies the relevant enhancement in the spin-current response, $F = \frac{\mathscr{M}_{G\neq 0}}{\mathscr{M}_{G=0}}$. To start off, we note that this ratio is independent of the Rabi frequency Ω, which, for this kind of experiments, would correspond to the low-power regime, like 1μW. Moreover, for a specified value of G, this ratio is fundamentally predicated on the properties intrinsic to the system. Consequently, any departure of F from unity is construed as a reinforcement due to the two-photon driving term. In other words, F would represent additional advantage of using the parametric drive over what is achievable otherwise.

We next present detailed results for the spin current based on Eq. (4.2). Note that we choose parameters such that the system is stable. Fig. 4.3(a,b) foregrounds the impact of variation in G on F in the form of a two-dimensional (2D) plot. The color-coded expanse within the graph, with $G < G_c$, pertains to the stable regime. Over a significant extent within the stable domain, the factor remains appreciably higher than unity. Particularly prominent is the narrow belt near the partition between the stable and unstable regimes, where the magnitude of F starts surging expeditiously to larger orders of 10. In view of this, we have split the stable domain into two distinct regions. Fig. 4.3(a) corresponds to the region over which the amplification factor is bounded above by 10.

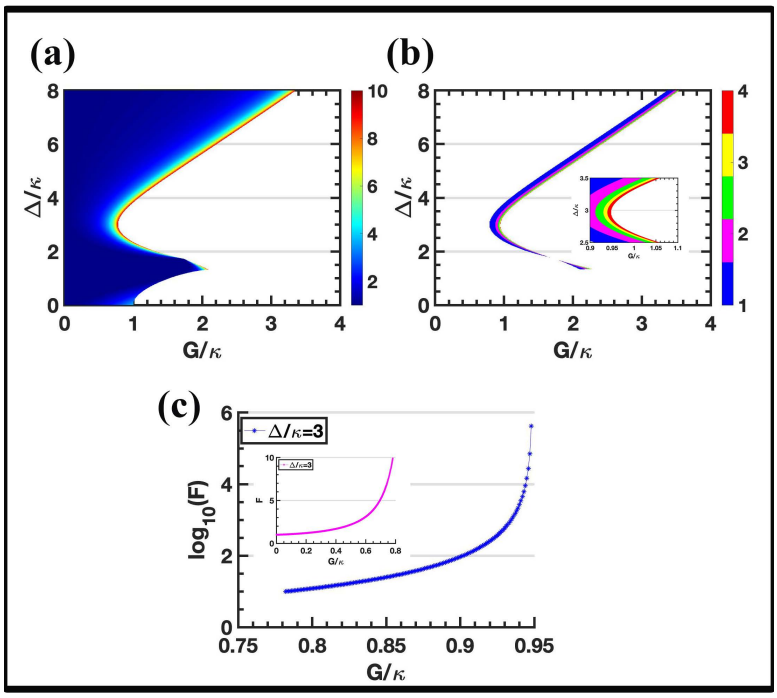

Figure 4.3: Spin-current amplification factor plotted (a,b) over the two-dimensional $\Delta - G$ plane, and (c) against G for $\Delta/\kappa = 3$. The figures in (b,c), plotted in logarithmic scale, highlights the region where F exceeds 10, and testify to the tremendous level of enhancement near the phase boundary $G_c/\kappa = 0.95$. The inset in (b) depicts a narrow segment of this region while the inset in (c) is a plot over the domain where F is bounded above by 10.

For the range of parameters close to the stability partition, the logarithmic graph in Fig. 4.3(b) displays a significantly large spot where the magnitude of $F \gg 10$. To provide useful estimates, a one-dimensional (1D) projection of the 2D plot onto the $\Delta/\kappa = 3$ subspace is showcased in Figs. 4.3(c). Initially, as the narrow strip near the boundary is approached, we encounter about a tenfold enhancement in the spin-current response, i.e., $F \simeq \mathcal{O}(10)$. Further advances towards the boundary renders prodigious enhancements by several orders of magnitude ($F \simeq \mathcal{O}(10^2 - 10^4)$), evidenced by the inset in Fig. 4.3(c). What is intrigiuing is that these remarkable enhancement factors are all accessible within the stable regime. One may ask if it is possible to enhance the standard ($G = 0$) photon mediated spin current by simply increasing the coupling strength g. Our calculations show that for $G = 0$, corresponding to a fixed Δ, the spin current increases, peaks and then saturates for large g-values. The peak value is less than 10 times the saturation value. This behavior persists over a fairly large range of Δ. Thus, the kind of enhancement reported in Fig. 4.3 cannot be achieved by increasing the coupling strength g. For completeness, in Fig. 4.4, we also compare the enhancement factor for a non-zero magnitude of the two-photon detuning $\delta = \omega_d - \omega_p/2$ against the corresponding graph in the resonant setting. The inclusion of a two-photon detuning serves to regularize the somewhat divergent behavior of F near the edge of the phase boundary. The detuning merely translates the coupling matrix as $H_{\text{eff}} \to H_{\text{eff}} - \delta$. On account of this rigid translation, the imaginary parts of the eigenvalues remain unaffected while the real parts get shifted by $-\delta$. This explains why the phase boundary does not change but the almost divergent nature of the response near the boundary is further stabilized. We also remark that the techniques for producing parametric drives in microwave domain are known from the early work of Yurke [112] and many others [113, 114]. Josephson junction amplifiers operating at low temperatures have evolved as the keystone for these experiments. This is in contrast to the ones in the optical domain which work at room temperature and utilize second order nonlinearities in crystals (see, for example, [115]). As an alternative strategy sustainable at room temperature, we also float the possibility of modulating the parametric pump at twice the cavity frequency, thereby generating the desired parametric interaction.

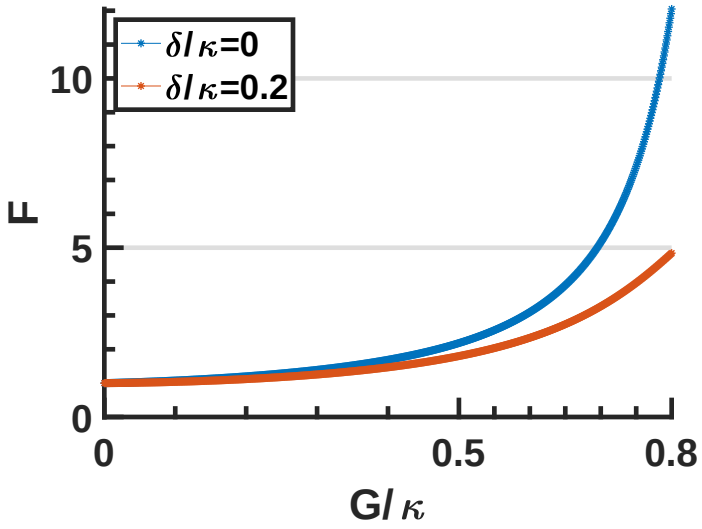

Figure 4.4: Comparative graph illustrating the respective enhancement factors under the two-photon resonance condition $\delta/\kappa = 0$, and in the detuned scenario, with $\delta/\kappa = 0.2$ chosen as an example. Here, $\delta = \omega_d - \omega_p/2$ signifies the two-photon detuning.

While we have presented the numerical results of the spin-current enhancement using the semi-classical approach, it is worthwhile to examine the contributions from quantum fluctuations to these semiclassical results. To account for quantum corrections, we need to work with the quantum Langevin equations [32] and evaluate the covariance matrix of photon and magnon variables. The analysis demonstrates that the quantum contribution remains many orders of magnitude smaller than the semiclassical contribution and can be ignored. The physical reason behind this is the the Langevin forces are delta-correlated, i.e. $\left\langle F(t)F^{\dagger}(t')\right\rangle = 2\gamma\delta(t-t')$, so that the fluctuations are effectively driven by a flux of strength γ. The semiclassical response, on the contrary, ensues from a classical driving field characterized by the Rabi frequency Ω. Since for a driving power of 1 μW, $(\Omega/\gamma) \sim 10^5$, the quantum contribution remains strongly subordinated.

4.2 Parametric-drive-induced long-lived mode

The anomalously large enhancement observed along the inner fringes of the stability boundary, and depicted in Fig. 4.3(c), is an immediate consequence of parametrically induced magnon-photon coherences. In particular, strong coherence leads to the emergence of a long-lived mode

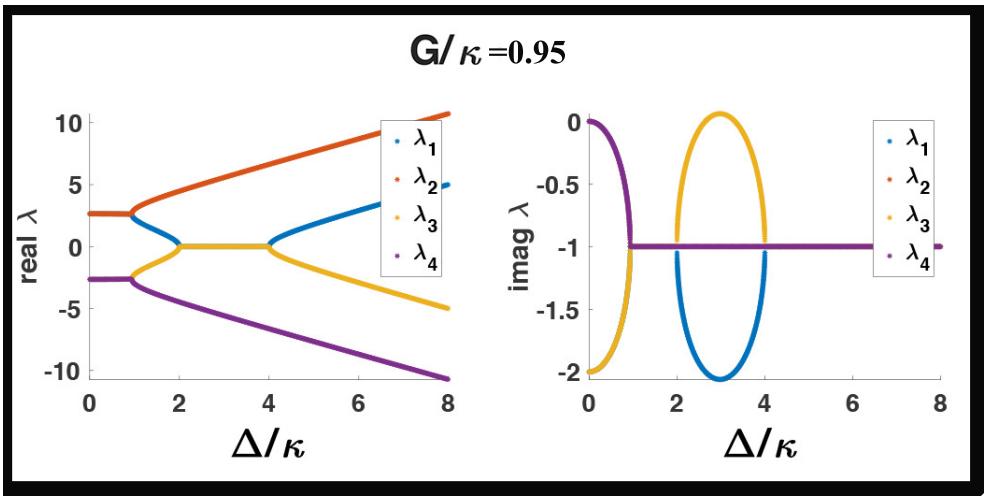

Figure 4.5: (a) Real and (b) Imaginary parts of the eigenvalues of the reduced 4×4 system involving the modes a and $M = (m_1 + m_2)/\sqrt{2}$ (as described by Eq. (4.3)).

which sharply reinforces the response function. We can streamline the characterization of eigenvalues by expressing the starting Hamiltonian in terms of the collective magnon operators $M = (m_1 + m_2)/\sqrt{2}$ and $m = (m_1 - m_2)/\sqrt{2}$. This leads to

$$\begin{aligned} \mathscr{H}/\hbar = \Delta a^\dagger a + \Delta M^\dagger M + \Delta m^\dagger m + g[a^\dagger M + a M^\dagger] \\ + G(a^2 + a^{\dagger 2}) + i\Omega[(M^\dagger + m^\dagger) - \text{h.c})], \end{aligned} \tag{4.3}$$

Clearly, the mode m, which is decoupled from the cavity field, can be dispensed with, and the coupled dynamics would involve only a, M, and their adjoints. The relevant dynamical equation can now be cast as

$$\dot{\mathscr{X}} = -i\mathscr{H}_{\text{eff}}\mathscr{X} + \Omega\mathscr{F}_{\text{in}}, \tag{4.4}$$

where we have $\mathscr{X} = (a\ M\ a^\dagger\ M^\dagger)^T$ and $\mathscr{H}_{\text{eff}} = \begin{pmatrix} \mathscr{H}_{\text{eff}}^{(0)} & \mathscr{J} \\ -\mathscr{J} & -\mathscr{H}_{\text{eff}}^{*(0)} \end{pmatrix}$, with $\mathscr{H}_{\text{eff}}^{(0)} = \begin{pmatrix} \Delta - i\gamma & g \\ g & \Delta - i\gamma \end{pmatrix}$, and $\mathscr{J} = \begin{pmatrix} 2G & 0 \\ 0 & 0 \end{pmatrix}$. We now plot the four eigenvalues (real and imaginary parts) of the reduced

Hamiltonian $\mathscr{H}_{\text{eff}}$ at $G/\kappa = 0.95$ in Figs. 4.5(a,b). It is observed that there exists a particular eigenvalue λ_3 with vanishing real part, and whose imaginary part becomes tantalizingly close to zero at $\Delta/\kappa \approx 3$. Viewed alternatively, the mode identified by λ_3 is symbolic of a long-lived or a bound state in continuum. Since $\mathscr{H}_{\text{eff}}^{-1} \sim (\det[\mathscr{H}_{\text{eff}}])^{-1} \sim (\prod_j \lambda_j^{-1})$, the effect of a vanishingly diminutive eigenvalue is reflected in the dramatic amplification of the steady-state response. The stark enhancement in the spin current stems from the energy of a two-photon parametric drive and stands testimony to the emergence of higher-order energy transition pathways ensuing from the parametric term (see Fig. 4.6). Without the parametric drive, the transfer efficiency was dictated by the applied magnon drive. However, with the provision of a parametric drive, an elementary two-photon excitation can raise the state $|1,0,0\rangle$ to $|3,0,0\rangle$. As the intracavity field interacts with the magnons, this energy can be redistributed amongst all the participating entities, leading to a myriad of allowed final states, such as $|2,1,0\rangle$, $|1,1,1\rangle$, and $|1,0,2\rangle$, to cite a few. Therefore, the possibility of effecting higher-order magnon occupancies opens up, even in the limit of very weak pumping rates. In general, for adequately strong values of G, transitions from $|1,0,0\rangle$ to higher-order excited states of the form $|2n+1,0,0\rangle$ can be achieved with greater probabilities, which, in turn, would engender higher-order excitations of the magnon modes. While we illustrate the energy transitions assuming an external drive at the single-photon level, these arguments are easily generalized to the case of larger coherent drives.

4.3 Summary

To sum things up, we have brought to light the emergence of parametrically induced strong coherence effects in a cavity-QED system which can lead to magnificent enhancements in the cavity-mediated transfer of spin excitations. In light of the recent upswing of interest in cavity magnonics, we have highlighted the application of this principle to the parametric amplification of spin currents in magnetic samples. To underline the origin of this enhancement, we have set forth a compact explanation in terms of higher-order energy transitions from the system's ground state stimulated by the cascaded two-photon absorption from the parametric pump. Increasing the strength of the parametric drive only serves to embolden this effect, with progressively higher

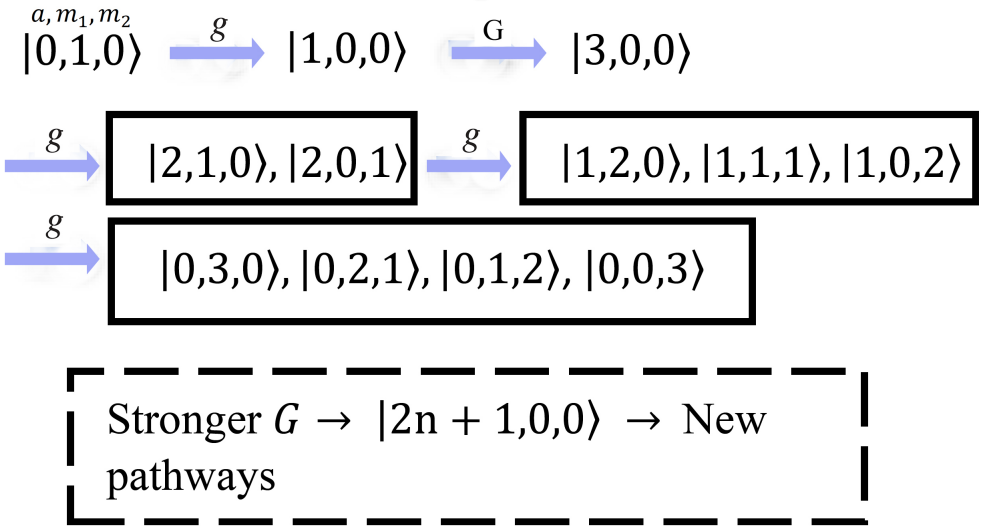

Figure 4.6: Higher-order energy transitions afforded by the parametric drive, assuming that YIG1 is driven by a coherent field at one-photon level.

and higher spin currents being observed. The efficiency of this process peaks at the two-photon resonance condition $\omega_d = \omega_p/2$, supporting enhancement by orders of magnitude even within the stable phase of the system dynamics. The spectacular amplification of spin-current transfer at the resonance condition stems from a parametrically produced long-lived mode in the system. The developed formalism and the accompanying results would apply to various kinds of systems. Quite generally, the energy-transfer protocol could be applied to systems of atoms, superconducting qubits and quantum dots, trapped ions, and spin ensembles, in general. Likewise, nonlinear effects such as bistability would also be reinforced on account of the parametrically induced coherences. We have preliminary results which show that for typical values of the Kerr-like nonlinearities in magnons and for power levels lower than 0.1 μ W, the results in Fig. 4.3 are not quite affected except when G/κ exceeds 0.9. However, this subject requires a detailed analysis and will be a topic of investigation in the future.

5. ANTI-$\hat{PT}$ SYMMETRY IN MAGNONICS[1]

One of the axioms of quantum mechanics necessitates the Hamiltonian of a physical system to be Hermitian, which ensures real energy eigenspectra. In 1998, Carl Bender introduced $\hat{PT}$-symmetric quantum mechanics, where the Hermiticity criterion was replaced by a less stringent space-time reflection symmetry [116], in other words, the $\hat{PT}$ symmetry and where $\hat{P}$ and $\hat{T}$ respectively denote parity and time-reversal operators. The spectrum of a Hamiltonian in the unbroken $\hat{PT}$-symmetric phase is real and it can be used to describe the physics of quantum mechanical systems. Non-Hermitian systems involving $\hat{PT}$ symmetry have attracted considerable attention, including, for example, in optics, acoustics, electrical circuits and recently in magnonics. In particular, non-Hermitian degeneracies of the $\hat{PT}$symmetric systems, the exceptional points (EPs) have found applications in enhanced sensing of linear perturbations. Note *en passant*, the real nature of eigenvalues is not only a property of $\hat{PT}$ symmetry systems but a large class of systems, namely pseudo-Hermitian systems.

Physical systems are inherently open, that is, systems interact with their environment leading to open quantum dynamics which can be described either by master equation or quantum Langevin approaches. This entails a non-Hermitian Hamiltonian to characterize the dynamics of the system. The dynamics of the system depend heavily on the symmetry properties of the effective non-Hermitian Hamiltonian. It is worth mentioning that $\hat{PT}$ symmetry requires the incorporation of external gain into the system and they do not occur naturally in nature. In contrast, there exists another interesting symmetry known as anti-$\hat{PT}$ symmetry of the non-Hermitian Hamiltonian $\hat{H}$ which does not require the incorporation gain into the system. It is defined by the condition $\{\hat{PT}, \hat{H}\} = 0$ where $\{A, B\}$ denotes the anti-commutator of A and B. In other words, the non-Hermitian Hamiltonian with anti-$\hat{PT}$ symmetry changes sign under the action of the $\hat{PT}$ operator.

[1]A small portion of this chapter is reprinted with permission from *Enhanced Sensing of Weak Anharmonicities through Coherences in Dissipatively Coupled Anti-PT Symmetric Systems* by J. M. P. Nair, D. Mukhopadhyay and G. S. Agarwal, Phys. Rev. Lett. **126**, 180401 (2021), published by the American Physical Society. Collaboration with D. Mukhopadhyay is acknowledged.

Anti-$\hat{PT}$ symmetry was first theoretically proposed by L. Ge *et al* in synthetic optical materials with negative refractive index and later experimentally realized by several different groups. Recently, the emergence of waveguide QED has opened up a new avenue in realizing anti-$\hat{PT}$ symmetric systems. Note that anti-$\hat{PT}$ symmetric systems are the most naturally occurring systems in nature when compared to their $\hat{PT}$ symmetric counterparts. In our research, we focus on the properties of anti-$\hat{PT}$ symmetric systems specifically in the context of magnonic models.

This chapter is organized as follows. In section 5.1, we discuss the symmetry properties of a generic two-mode system with a focus on anti-$\hat{PT}$ symmetry and we detail the possible experimental realizations of anti-$\hat{PT}$ symmetric systems in section 5.2. We summarize the chapter in section 5.3.

5.1 Symmetry properties of two-mode non-Hermitian systems

The dynamics of a two-mode system, according to the coupled-mode theory is provided by

$$\dot{X} = -i\mathscr{H}X + F_{in}, \tag{5.1}$$

where the constituents of the column matrix X denote the mean-field amplitudes of the two modes, $\mathscr{H}$ is an effective 2×2 non-Hermitian Hamiltonian and F_{in} describes the modality of external pumping. $\hat{PT}$-symmetry is defined by the condition $[\hat{PT}, \mathscr{H}] = 0$ where $\hat{P} = \begin{pmatrix} 0 & 1 \\ 1 & 0 \end{pmatrix}$ and the action $\hat{T}$ results in complex conjugation of $\mathscr{H}$, that is, $\hat{T}\alpha\hat{T} = \alpha^*$ for any complex scalar α. Consider a generic 2×2 Hamiltonian given by $\mathscr{H} = \begin{pmatrix} \alpha & \beta \\ \mu & \nu \end{pmatrix}$ for complex values of the matrix constituents. Under the action of $\hat{PT}$, the Hamiltonian transforms into

$$\hat{PT}\,\mathscr{H}\,\hat{PT} = \tilde{\mathscr{H}} = \begin{pmatrix} \nu^* & \mu^* \\ \beta^* & \alpha^* \end{pmatrix}. \tag{5.2}$$

The Hamiltonian is said to be $\hat{PT}$ symmetric if $\tilde{\mathscr{H}} = \mathscr{H}$ and anti-$\hat{PT}$ symmetric when $\tilde{\mathscr{H}} = -\mathscr{H}$. Let us consider both the scenarios in detail.

$\hat{PT}$ symmetry: $\hat{PT}$ symmetric mode hybridization is conformable with the parameter choices $\alpha = \delta/2 - i\gamma$ and $\beta = g$ where δ, γ and g are real parameters. The Hamiltonian of a $\hat{PT}$ symmetric system can be written as

$$\mathscr{H} = \begin{pmatrix} \delta/2 - i\gamma & g \\ g & \delta/2 + i\gamma \end{pmatrix}. \tag{5.3}$$

Notice the term $\mathscr{H}_{22} = \delta/2 + i\gamma$ include external gain into the system commensurate with the damping in the other mode. The eigenvalues are $\lambda_{\pm} = \delta/2 \pm \sqrt{g^2 - \gamma^2}$ are the corresponding right eigenstates are given by

$$|\psi\rangle_{+} = \frac{1}{\sqrt{2}} \begin{pmatrix} \chi \\ 1 \end{pmatrix}, |\psi\rangle_{-} = \frac{1}{\sqrt{2}} \begin{pmatrix} -\chi^{*} \\ 1 \end{pmatrix}, \tag{5.4}$$

where $\chi = \sqrt{1 - (\gamma/g)^2} - i2\gamma/g$. The system is in an unbroken $\hat{PT}$-symmetric phase if every eigenfunction of $\mathscr{H}$ is also an eigenfunction of the $\hat{PT}$ operator. By the same token, if some of the eigenfunctions of $\mathscr{H}$ are not eigenfunctions of $\hat{PT}$, the $\hat{PT}$ symmetry of $\mathscr{H}$ is broken. Therefore, the system is in the $\hat{PT}$-symmetric phase for $g \geq \gamma$ leading to real eigenvalues. It follows that the transition point $\gamma = g$, which defines the EP, introduces real singularities by quenching the line widths to nought as depicted in Fig. 5.1. Note that the existence of EPs is a property of non-Hermitian systems. It is apparent from Eq. (5.4) that at an EP of order 2, both eigenfunctions $|\psi\rangle_{+}$ and $|\psi\rangle_{-}$ coalesce to a unique eigenfunction. Stated differently, at an EP, both the eigenvalues and eigenfunctions of the system coincide and the non-Hermitian Hamiltonian becomes non-diagonalizable. It is worth mentioning that a Hermitian Hamiltonian remains diagonalizable irrespective of degeneracies in the eigenspectrum, thanks to the existence of a complete set of eigenstates. In contrast, one must use a Jordan normal decomposition of the Hamiltonian at the EP. As mentioned in the introduction, EPs have found applications in sensing linear perturbations in classical systems which will be discussed later in this chapter.

anti-$\hat{PT}$ symmetry: An anti-$\hat{PT}$ symmetric realization of mode hybridization can be pinned

down by the parameter choices $\alpha = \delta/2 - i\gamma$, $\beta = -i\Gamma$. Clearly, while the modes are oppositely detuned in character, both of them retain their lossy nature where $\mathscr{H}$ is substituted by $\mathscr{H} = \begin{pmatrix} \delta/2 - i\gamma & -i\Gamma \\ -i\Gamma & -\delta/2 - i\gamma \end{pmatrix}$. The eigenvalues would be obtained as $-i\gamma \pm \sqrt{\delta^2/4 - \Gamma^2}$ for $|\delta/2| > \Gamma$ and $-i\gamma \pm i\sqrt{\Gamma^2 - \delta^2/4}$ ($\hat{PT}$ symmetric phase) for $|\delta/2| < \Gamma$. The behaviour of the real and imaginary parts of these eigenvalues is provided in Fig. 5.1. As long as the stability criterion is fulfilled, the linear response of the system is inversely related to $\det[\mathscr{H}] = -[\delta^2/4 - \gamma^2 + \Gamma^2]$. The $\hat{PT}$ phase brings in real singularities at $\delta = 0$ in the limit $\gamma_0 \to 0$, which is evidenced by the resonant inhibition in the imaginary part of λ_+, as marked by the point X in Fig. 5.1 (d). The extreme condition $\gamma \to \Gamma$ holds when none of the modes suffers spontaneous losses to its independent surrounding. The point X distinguishes an especially long-lived resonance, which leads to a tremendous buildup in the steady-state amplitudes. We would demonstrate in Chapter 4 how the inclusion of anharmonicity promptly regularizes the divergent linear response, with the nonlinear response being highly sensitive to variations in the strength of anharmonicity. Note that point X in anti-$\hat{PT}$ symmetric systems is functionally analogous to the EP in $\hat{PT}$ symmetric systems.

5.2 Possible realizations of anti-$\hat{PT}$ symmetry

Before going into the possible realizations of anti-$\hat{PT}$ symmetry, let us begin by discussing the emergence of $\hat{PT}$ symmetric systems. They have been realized in multitude of settings, including for example in photonic structures and mechanical membranes. In particular, optical systems with balanced loss and gain have evinced several exotic phenomena emerging out of $\hat{PT}$symmetric systems, including the observation of non-reciprocal transport, coherent perfect absorption, metrology, etc. Of particular interest are the phase transition points in $\hat{PT}$ symmetric systems, the EPs with exciting new phenomena. Some well-known examples include the observation of unidirectional invisibility, enhanced sensing, laser mode selection etc. to name a few.

In stark contrast to $\hat{PT}$ symmetric systems, anti-$\hat{PT}$ symmetric systems do not require external gain into the system. The first experimental realization of anti-$\hat{PT}$ symmetry in a physical system came in 2016 using dissipative couplings between spin waves from flying atoms in a warm atomic

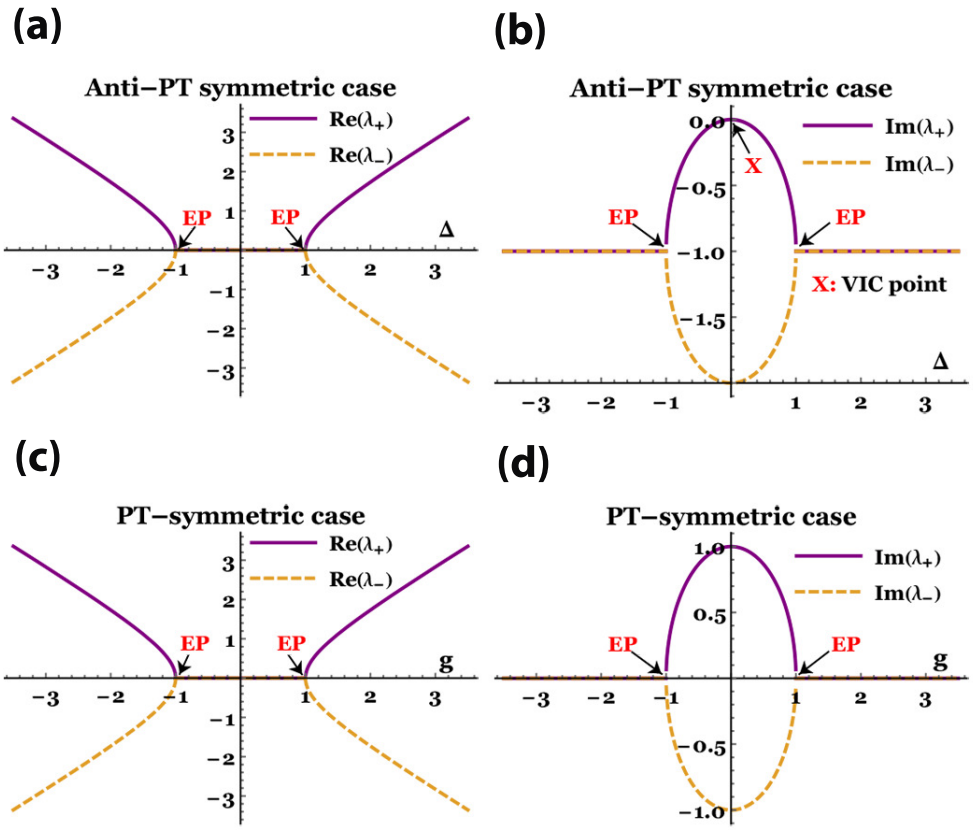

Figure 5.1: a), b) Eigenfrequencies and linewidths for an anti-$\hat{PT}$ symmetric system, plotted against a variable $\Delta = \delta/2$, calculated in units of Γ. While EPs emerge at $\Delta = \pm\Gamma$, the VIC-induced linewidth suppression (designated as X) corresponds to $\delta = 0$. c), d) Analogous plots for the $\hat{PT}$ symmetric system, against the coupling strength g, in units of γ, at $\Delta = 0$. EPs are found at $g = \pm\gamma$.

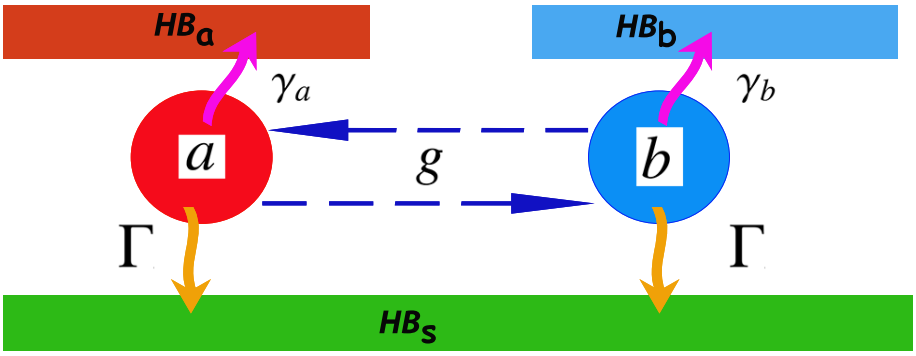

Figure 5.2: Schematic of a general two-mode system dissipatively coupled through a waveguide. $\gamma_{a(b)}$ and Γ describe decay into the surrounding (local heat bath) and coupling to the fiber (shared bath) respectively.

vapour cell. In addition, anti-$\hat{PT}$ symmetric systems have been investigated, theoretically and experimentally, in a plentitude of settings including, but not limited to driven cold atoms [117, 118], laser-cooled atomic ensembles [119], metamaterials [78], nonlinear optical systems [120], waveguides [121, 122], diffusive systems [123], coupled cavity-magnon systems [76], qubits using nuclear spins [124] and have been revealed to entail many exotic physical phenomena. Recently, in 2018, anti-$\hat{PT}$ symmetry was experimentally demonstrated in an electrical circuit employing negative resistance units where they demonstrated phase transitions at an EP of the anti-$\hat{PT}$ symmetric system [125]. In the following, we detail the theory of the origin of anti-$\hat{PT}$ symmetry using dissipative couplings.

5.2.1 Anti-$\hat{PT}$ symmetry through dissipative coupling

It is well-known that quantum mechanically, the spatial overlap between two sub-systems can bring about coherent coupling which enters as a real off-diagonal term in the effective Hamiltonian describing the dynamics of the system. In addition, these subsystems could be interfacing with a dissipative environment. Dissipative environments in an open quantum system fall roughly under two classifications - one, where the modes are coupled independently to their local heat baths, and another, where a common reservoir interacts with both as depicted in Fig. 5.2. When the common

reservoir is adiabatically eliminated, the dynamics of the system engenders a complex coupling between the subsystems having coherent and dissipative components. The coupling is fundamentally of quantum origin and waveguide QED offers a platform to manipulate such interactions. It is interesting to note the generality of the scheme, i.e., any systems, for instance, atoms, superconducting qubits, cavities etc. can be used to engineer dissipative coupling through a waveguide. To further explain the origin of anti-$\hat{PT}$ symmetry, we consider a two-mode system coupled through a waveguide characterized by the Hamiltonian

$$H = \Delta_a a^\dagger a + \Delta_b b^\dagger b + i\Omega(b^\dagger - b), \tag{5.5}$$

where Δ_a and Δ_b are the frequency detunings of the modes relative to the external drive with Rabi frequency Ω. Note that the coupling through the waveguide is not included in the Hamiltonian and it enters through the master equation characterizing the full dynamics. A complete description of the two-mode system, in terms of its density matrix ρ, is provided by the master equation [126] (Appendix A)

$$\frac{\mathrm{d}\rho}{\mathrm{d}t} = -\frac{i}{\hbar}[H,\rho] + \gamma_a \mathscr{L}(a)\rho + \gamma_b \mathscr{L}(b)\rho + 2\Gamma \mathscr{L}(c)\rho, \tag{5.6}$$

where γ_a and γ_b are, respectively, the intrinsic damping rates of the modes, induced by coupling with their independent heat baths. The parameter Γ introduces coherences, and the Liouvillian operator $\mathscr{L}$ is defined by its action $\mathscr{L}(\sigma)\rho = 2\sigma\rho\sigma^\dagger - \sigma^\dagger\sigma\rho - \rho\sigma^\dagger\sigma$. Assuming symmetrical couplings of the modes to the common reservoir we have the relation $c = \frac{1}{\sqrt{2}}(a + b)$. The master equation is valid under the condition that the phase difference of light propagation from one mode to the other is a multiple of 2π. Therefore, the mean field equations for the dynamics of the system are given by

$$\begin{pmatrix} \dot{a} \\ \dot{b} \end{pmatrix} = -i\mathscr{H} \begin{pmatrix} a \\ b \end{pmatrix} + \Omega \begin{pmatrix} 0 \\ 1 \end{pmatrix}, \tag{5.7}$$

where $\mathscr{H} = \begin{pmatrix} \Delta_a - i(\gamma_a + \Gamma) & -i\Gamma \\ -i\Gamma & \Delta_b - i(\gamma_b + \Gamma) \end{pmatrix}$. Palpably, the off-diagonal elements of the system are purely imaginary, alluding to the dissipative form of coupling between the modes. In 2020, Yang *et al* demonstrated the realization anti-$\hat{PT}$ symmetric system in a cavity magnonic setup by dissipatively coupling a microwave cavity with a YIG sample through a waveguide. In the next few chapters, we would focus on anti-$\hat{PT}$ symmetric systems, specifically in the context of magnonic setups. In particular, the following chapter discusses the great utility of dissipatively coupled two-mode systems for the sensing of anharmonic systems. Before that, in the next section, we review the mechanism of sensing linear perturbations close to EPs in $\hat{PT}$ symmetric systems

5.3 Summary

In summary, we have reviewed the general properties of non-Hermitian dynamics in open quantum systems. We discussed two interesting symmetries of the effective non-Hermitian Hamiltonian demonstrating exotic physical effects. The first of them, $\hat{PT}$ symmetric systems require the incorporation of external gain and the non-Hermitian degeneracies in such systems, the EPs possess excellent sensing capabilities. In contrast, anti-$\hat{PT}$ symmetric systems are the most naturally occurring symmetries in nature. We have detailed various experimental platforms to realize it and specifically illustrated the role of dissipative coupling in these setups. In the subsequent chapter, we will discuss how anti-$\hat{PT}$ symmetric systems can be used for the enhanced sensing of anharmonic perturbations.

6. ENHANCED SENSING OF WEAK PERTURBATIONS IN DISSIPATIVELY COUPLED TWO-MODE SYSTEMS[1]

The development of sensors with improved sensitivity and selectivity plays a quintessential role in advancing newer technologies with far-reaching applications [127–131] across various scientific disciplines. Over the last decade, there has been a significant amount of interest in EPs [132–136] to engineer augmented response in an open quantum system [116, 137–149]. Some recent experiments include the demonstration of enhanced sensitivity in microcavities near EPs [137] and the observation of higher-order EPs in a coupled-cavity arrangement [138]. While this is a truly remarkable development and has acquired a lot of traction, these methodologies are customized to sense only linear perturbations. One would like to examine the possibilities of newer sensing techniques, which could be tapped for the detection of anharmonic perturbations.

In this chapter, we outline a new protocol for the enhanced sensing of nonlinearities in dissipatively coupled anti-$\hat{PT}$ systems where the coupling between subsystems is produced via interaction through a common intermediary reservoir [126]. The sensing scheme hinges on the emergence of VIC in such systems which has been the subject of intense activity [150–164] with applications ranging from heat engines [154], nuclear gamma ray transmission [160] to photosynthesis [161] and molecular isomerization in vision [164]. In a linear system with strong VIC, one of the eigenvalues characterizing its dynamics moves to the real axis generating a long-lived eigenmode precipitating in a prodigious response to external fields.We demonstrate that the response is strongly sensitive to weak nonlinearities which are, otherwise, difficult to detect.

Guided by recent experiments, we show explicit results on enhanced sensing by employing the VIC paradigm in an anti-$\hat{PT}$ symmetric configuration to the detection of very weak magnetic nonlinearities in a YIG sphere coupled to a cavity [21, 22, 25, 37, 66, 67, 72, 74, 76, 165–169]. Dis-

[1] A major part of this chapter is reprinted with permission from *Enhanced Sensing of Weak Anharmonicities through Coherences in Dissipatively Coupled Anti-PT Symmetric Systems* by J. M. P. Nair, D. Mukhopadhyay and G. S. Agarwal, Phys. Rev. Lett. **126**, 180401 (2021), published by the American Physical Society. Collaboration with D. Mukhopadhyay is acknowledged.

sipative coupling using YIGs has been observed in a multitude of settings, involving, for instance, a Fabry-perot cavity [66] or a coplanar waveguide [67]. Note that under most circumstances, weak nonlinearities of the order of nHZ would require immense drive power to be detected in experiments. However, a dissipatively coupled system affords a prodigious response in the magnetization of the YIG which goes up spectacularly with the weakening strength of nonlinearity. That this response is strongly sensitive to variations in the strength of anhamonicity underpins the utility of our scheme in sensing applications. This new paradigm is applicable generally to a wide class of systems encountered across various scientific disciplines. Examples include quantum dots coupled to plasmonic excitations in a nanowire [170], superconducting transmon qubits [171], quantum emitters coupled to metamaterials [150–152, 172], optomechanical systems [173], hybrid magnon-photon systems [66] and more.

This chapter is organized as follows. In section 6.1, we expound the properties of the linear response in a dissipatively coupled two mode system and the effects of VIC. In section 6.2, we provide scheme for the enhanced sensing of weak anharmonic perturbations in such systems exploiting the VIC point and we specifically illustrate the sesning capabilities of our scheme in the context of a cavity-magnon system in section 6.3. We conclude the chapter in section 6.4.

6.1 Linear response in a dissipatively coupled two-mode system

We start off by considering the general model for a two-mode anharmonic system, which is pertinent to a wide range of physical systems. The Hamiltonian of the system, analogous to Eq. (2.33) is given by

$$\begin{aligned} H/\hbar = \omega_a a^\dagger a + \omega_b b^\dagger b + g(ab^\dagger + a^\dagger b) \\ +U(b^{\dagger 2} b^2) + i\Omega(b^\dagger e^{-i\omega_d t} - b e^{i\omega_d t}), \end{aligned} \tag{6.1}$$

where ω_a and ω_b denote the respective resonance frequencies of the uncoupled modes a and b, and g constitutes the coherent hermitian coupling between them. The parameter U is a measure of the strength of anharmonicity intrinsic to the mode b, which is driven externally by a laser at frequency

ω_d. The quantity Ω represents the Rabi frequency. If the two modes are coupled dissipatively at strength Γ, the mean value equations for a and b are obtained to be

$$\begin{pmatrix} \dot{a} \\ \dot{b} \end{pmatrix} = -i\mathscr{H}\begin{pmatrix} a \\ b \end{pmatrix} - 2iU(b^\dagger b)\mathscr{R}\begin{pmatrix} a \\ b \end{pmatrix} + \Omega e^{-i\omega_d t}\begin{pmatrix} 0 \\ 1 \end{pmatrix}, \tag{6.2}$$

where $\mathscr{H} = \begin{pmatrix} \omega_a - i(\gamma_a + \Gamma) & g - i\Gamma \\ g - i\Gamma & \omega_b - i(\gamma_b + \Gamma) \end{pmatrix}$, $\mathscr{R} = \begin{pmatrix} 0 & 0 \\ 0 & 1 \end{pmatrix}$. A canonical transformation of the form $(a, b) \to e^{-i\omega_d t}(a, b)$ stamps out the time dependence on the final term in Eq. (6.2) and translates $\mathscr{H}$ to $\mathscr{H}^{(d)} = \mathscr{H} - \omega_d \mathbb{1}$ without tampering with the nonlinear term, where $\mathbb{1}$ is the 2×2 identity matrix. This transformation takes us to the frame of the applied laser frequency.

Before proceeding with a generalized treatment, let us first deconstruct the linear dynamics in the case of purely dissipative coupling, i.e. when U is dropped and $g = 0$. Defining $\delta = \omega_a - \omega_b$ and the mode detunings $\Delta_i = \omega_i - \omega_d$ $(i = a, b)$, we have the eigenvalues of $\mathscr{H}^{(d)}$ given by $\lambda_\pm = \frac{\Delta_a + \Delta_b}{2} - i(\gamma_0 + \Gamma) \pm i\sqrt{(\Gamma^2 - \delta/2)^2}$, for $|\delta/2| < \Gamma$ with $\gamma_0 = \gamma_a = \gamma_b$. Contingent on the stability condition, that is, making sure the imaginary parts of the eigenvalues of $\mathscr{H}^{(d)}$ is less than zero which averts exponential amplification, the steady-state solutions for the mean values $\mathscr{O}^{(i)} = \langle O \rangle$ $(\mathscr{O}^{(i)} = \mathscr{A}, \mathscr{B}; i = a, b)$ would unfold as

$$\frac{\mathscr{A}}{\Gamma} = \frac{\mathscr{B}}{-i\delta/2 - \gamma} = \frac{\Omega}{\Gamma^2 - (\delta/2)^2 - \gamma^2}, \tag{6.3}$$

where, we have set $\Delta_a = -\Delta_b = \delta/2$ and $\gamma = \gamma_0 + \Gamma$. Palpably, in the limit when $\delta \to 0$ and $\gamma \to \Gamma$, in other words, close to VIC, the linear response demonstrates a real singularity which can be used for the enhanced sensing of both linear and nonlinear perturbations.

Sensing of linear perturbations close to VIC: Before going into the details of sensing nonlinear perturbations, let us discuss the utility of VIC in sensing linear perturbations. In Eq. (6.3), we obtained the expression for the linear response of a dissipatively coupled two mode system under anti-$\hat{PT}$ symmetry. Consider a complex perturbation ϵ to one of the diagonal elements of $\mathscr{H}^{(d)}$,

for example, $\mathscr{H}_{22}^{(d)} = -\delta/2 - i\gamma + \epsilon$. Subsequently, the linear response of the system in Eq. (6.3) modifies to

$$\frac{\mathscr{A}}{\Gamma} = \frac{\mathscr{B}}{-i\delta/2 - \gamma} = \frac{\Omega}{\Gamma^2 - (\delta/2)^2 + (\delta/2 - i\gamma)\epsilon - \gamma^2}. \tag{6.4}$$

The sensitivity of the response functions in variations to the parameter ϵ can, then, be obtained as

$$\frac{\partial\mathscr{A}(\epsilon)}{\partial\epsilon} = \frac{\Omega\Gamma(\delta/2 - i\gamma)}{[\Gamma^2 - (\delta/2)^2 + (\delta/2 - i\gamma)\epsilon - \gamma^2]^2}, \quad \frac{\partial\mathscr{B}(\epsilon)}{\partial\epsilon} = \frac{i\Omega\Gamma(\gamma + i\delta/2)^2}{[\Gamma^2 - (\delta/2)^2 + (\delta/2 - i\gamma)\epsilon - \gamma^2]^2}. \tag{6.5}$$

When the system parameters are tuned tantalizing close to VIC, i.e., in the limit when $\delta \to 0$ and $\gamma \to \Gamma$, the sensitivities scales as ϵ^{-2}, leading to a prodigious response to variations in the parameter ϵ. In fact, adjacent to VIC, a perturbation in any of the four elements of the matrix $\mathscr{H}^{(d)}$ would engender a pronounced linear response which would scale as inverse square of the perturbation parameter. In the following, we show how VIC and the accompanied diverging response can be used for the enhanced sensing of nonlinear perturbations.

6.2 Enhanced sensing of weak nonlinear perturbations

Next, we illustrate the importance of the condition $\mathrm{Im}(\lambda_+) \to 0$ in the context of the nonlinear response observed in the system. The nonlinear behaviour depends on the intrinsic symmetry properties of the matrix $\mathscr{H}$. Specifically, the extraordinary response achievable in anti-$\hat{PT}$ symmetric models yields a convenient protocol for the fine-grained estimation of weak anharmonicity. We now consider a full treatment of Eq. (6.2) by factoring in the effect of U. In the rotating frame, upon setting $g = 0$ and choosing $\gamma_a = \gamma_b = \gamma_0$, this leads to the modified steady-state relations:

$$\begin{aligned} -(i\delta/2 + \gamma_0 + \Gamma)a - \Gamma b = 0, \\ -(-i\delta/2 + \gamma_0 + \Gamma)b - 2iU|b|^2 b - \Gamma a + \Omega = 0. \end{aligned} \tag{6.6}$$

Defining $\gamma = \gamma_0 + \Gamma$ and eliminating a, the intensity $x = |b|^2$ is found to satisfy a cubic relation

$$\frac{\beta^2}{\gamma^2 + (\delta/2)^2} x - \frac{2U\beta\delta}{\gamma^2 + (\delta/2)^2} x^2 + 4U^2 x^3 = I, \tag{6.7}$$

where $\beta = \Gamma^2 - \gamma^2 - (\delta/2)^2$ and $I = \Omega^2$. Eq. (6.7) can entail a bistable response under the condition $U\delta < 0$ and $\delta^2 > 12\gamma^2$. However, throughout this manuscript, we operate at adequately low drive powers to ward off bistable signatures. Now, in the limit $\gamma_0 \to 0$ and $\delta \to 0$, β becomes vanishingly small, and the first two terms in Eq. (6.7) recede in importance, for a given Rabi frequency Ω. Consequently, in the neighbourhood of $\delta = 0$, the response becomes highly sensitive to variations in U. To be more precise, for sufficiently low values of the detuning, the response mimics the functional dependence $x \approx (I/4U^2)^{1/3}$. A tenfold decrease in U, therefore, scales up the peak intensity of b by a factor of 4.64. In this context, it is useful to strike a correspondence with the sensitivity in eigenmode splitting around an EP which is typically employed in $\hat{PT}$-symmetric sensing protocols [137, 138, 141]. For two-mode systems, where the EP is characterized by a square root singularity, this splitting $\delta\omega$ scales as the square root of the perturbation parameter ϵ implying a sensitivity that goes as $\left|\frac{\delta\omega}{\delta\epsilon}\right| \propto |\epsilon|^{-1/2}$. However, in our setup, the sensitivity to U in the response is encoded as $\left|\frac{\delta x}{\delta U}\right| \propto |U|^{-5/3}$.

6.3 Results on enhanced sensing for a dissipatively coupled cavity-magnon system

The importance of the above result in the context of sensing is hereby legitimized for dissipatively coupled systems. Guided by the recent experiments on dissipatively coupled hybrid magnon-photon systems [66, 67, 72, 76, 165–167], we apply these ideas to the specific example of Kerr nonlinearity in a YIG sample [37]. However, the bulk of these works have restricted their investigations to the linear domain. Here, we transcend this restriction and study the nonlinear response to an external drive. We consider an integrated apparatus comprising a microwave cavity and a YIG sphere, both interfacing with a one-dimensional waveguide [76, 165], as depicted in Fig.6.1. Owing to the nonexistent spatial overlap between the cavity and magnon modes, the direct coupling between them can be dropped. However, the interaction with the waveguide would

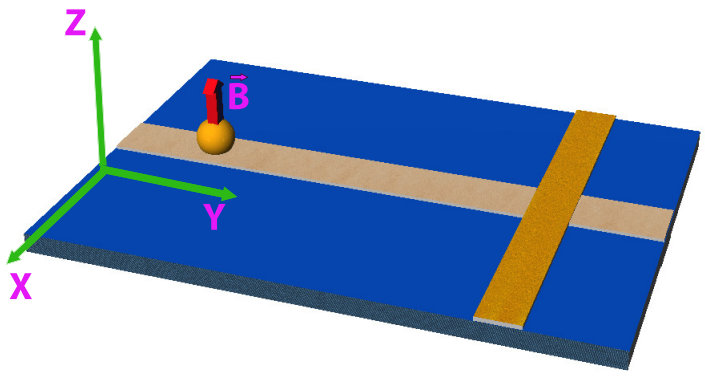

Figure 6.1: Schematic of the cavity-magnonic setup. The microwave cavity, running transverse to the waveguide, interacts with the YIG via the transmission line. A static magnetic field aligned along the z-axis generates the Kittel mode in YIG. (Redrawn from *Phys. Rev. Lett.* ***125****, 147202 (2020).*)

engender an indirect coupling between them. In order to excite the weak Kerr nonlinearity of the YIG sphere, a microwave laser is used to drive the spatially uniform Kittel mode. The full Hamiltonian in the presence of the external drive can be cast exactly in the form of Eq. (6.1), with b superseded by the magnonic operator m [37, 38].

As discussed earlier, the mediating effect of the waveguide is reflected as a dissipative coupling between the two modes, which instills VIC into the system. With the anti-$\hat{PT}$ symmetric choices $\Delta_a = -\Delta_m = \delta/2$, $\gamma_a = \gamma_b = \gamma_0$, and the redefinition $\gamma_0 + \Gamma = \gamma$, we recover Eq. (6.7) in the steady state, with the obvious substitution $b \to m$ and $x = |m|^2$ denoting the spin current response. We now expound the utility of engineering a lossless system in sensing weak Kerr nonlinearity. To that end, we zero in on the parameter subspace $\Gamma = \gamma = 2\pi \times 10$ MHz. Since $\beta = -\delta^2/4$, the contributions from the first two terms in Eq. (6.7) taper off as resonance is approached. As outlined earlier, we find that for all practical purposes, the nonlinear response can be approximated as $x \approx (I/4U^2)^{1/3}$ in the region $\delta/2\pi < 1$ MHz, which demonstrates its stark sensitivity to U. A lower nonlinearity begets a higher response, as manifested in Fig. 6.2(a), where plots of x against δ are studied at differing strengths of the nonlinearity. Even at $D_p = 1\ \mu W$, we observe a significant enhancement in the induced spin current of the YIG around $\delta = 0$. The result is a

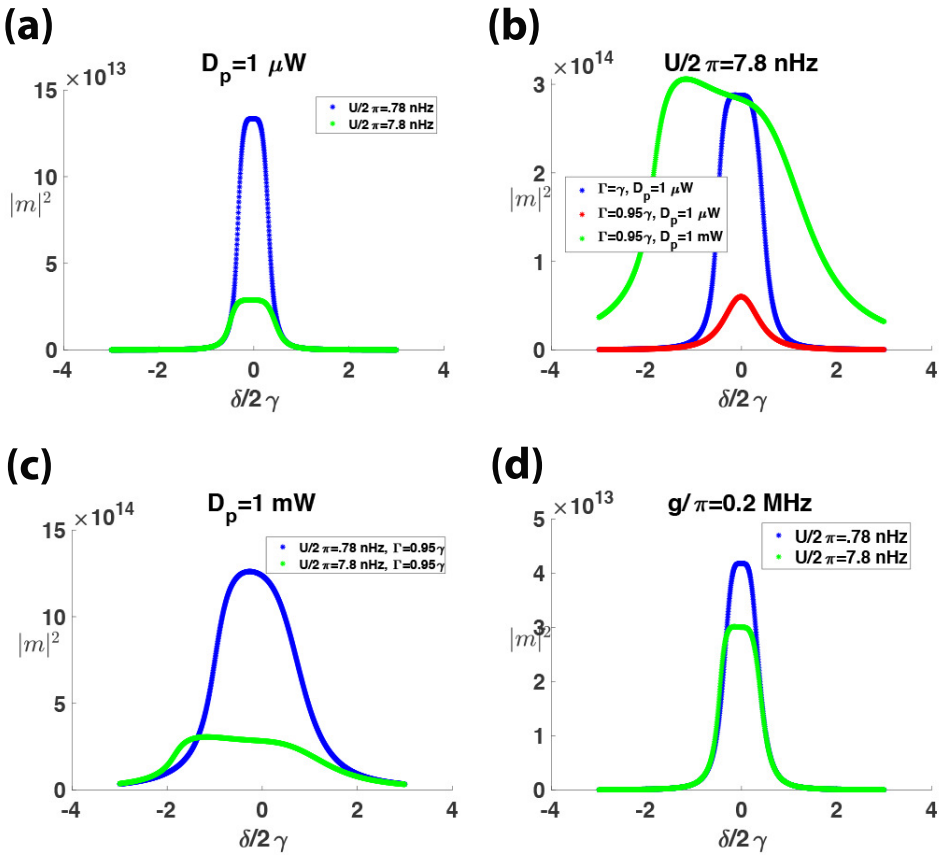

Figure 6.2: a) The spin current plotted against δ at two different nonlinearities; b) spin currents away from the VIC condition, compared against the lossless scenario, at different drive powers- for ease of comparison, the blue and red curves have been scaled up by 10; c) contrasting responses observed at a drive power of 1 mW for two different strengths of nonlinearity; d) sensitivity for a nonzero coherent coupling g at $D_p = 1\ \mu$W.

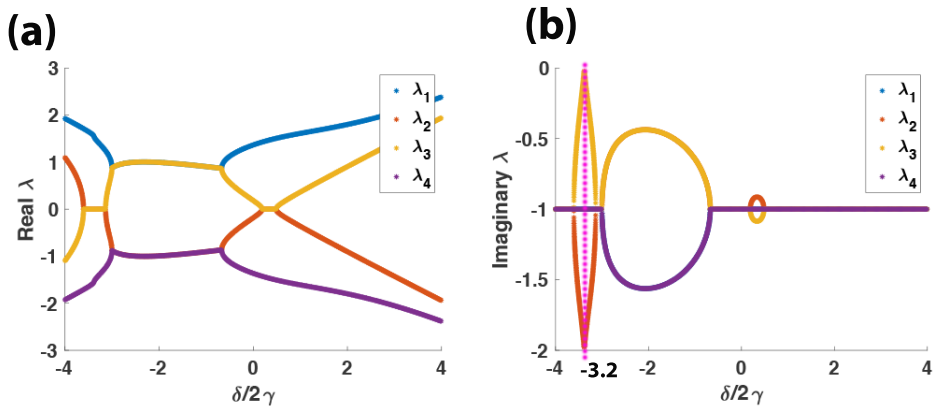

Figure 6.3: a) Real and b) imaginary parts of the eigenvalues of $\mathscr{H}_{NL}$ at a drive power of 0.1 W.

natural upshot of the VIC-induced divergent response in an anti-$\hat{PT}$ symmetric system in the linear regime. Quite conveniently, the inclusion of nonlinearity dispels the seemingly absurd problem of a real singularity noticed in the linear case. If $\Gamma < \gamma$, a strong quenching in the response is observed, as depicted in Fig. 6.2(b). The sensitivity to variations in U also incurs deleterious consequences. Nevertheless, we can counteract this decline by boosting the drive power. A drive power close to 1 mW can bring back the augmented response and the pronounced sensitivity to U (Fig. 6.2(c)). By the same token, the introduction of coherent coupling g between the two modes prompts a decline in the sensitivity. The real singularity pertaining to a purely dissipative linear model is now replaced by a complex one, i.e., with a finite linewidth, bringing down the sharpness of the resonance and similarly, the sensitivity. Here, a tenfold depreciation in U barely generates an enhancement factor of 1.39 in the response, as illustrated in Fig. 6.2 (d). This is to be contrasted with the $g = 0$ case in Fig. 6.2(a), where the magnification factor is 4.64 for an otherwise identical set of parameters. Propitiously, systems with zero coherent coupling were engineered in recent experiments [76, 165]. This mechanism can, thus, serve as an efficient tool to sense small anharmonicities present in a system.

The protocol hinges on the anti-$\hat{PT}$ symmetric character and eigenmodes of $\mathscr{H}$, which largely control the dynamics at low drive powers. At larger drive powers ($\sim$ 0.1 W), the nonlinear cor-

rection in (3) becomes important. This phenomenon can be understood by studying the modified spectroscopic character of the system in response to a weak probe field. The nonlinear effects can be encapsulated as time-varying fluctuations to the steady-state values, *viz.* $a(t) = a + \delta a(t)$, $b(t) = b + \delta b(t)$. By virtue of linearization [33], the dynamics of the fluctuations $\delta\xi = \begin{pmatrix}\delta a(t) & \delta b(t) & \delta a^\dagger(t) & \delta b^\dagger(t)\end{pmatrix}^T$ could be explained through a higher-dimensional Hamiltonian matrix,

$$\mathscr{H}_{NL} = \begin{pmatrix} -\frac{\delta}{2} - i\gamma & -i\Gamma & 0 & 0 \\ -i\Gamma & \tilde{\Delta} - i\gamma & 0 & 2Ub^2 \\ 0 & 0 & \frac{\delta}{2} - i\gamma & -i\Gamma \\ 0 & -2Ub^{*2} & -i\Gamma & -\tilde{\Delta} - i\gamma \end{pmatrix}, \tag{6.8}$$

where $\tilde{\Delta} = \frac{\delta}{2} + 4U|b|^2$. The eigenvalues of this matrix, for the cavity-magnon setting, appear in Fig. 6.3. Strong anharmonicity alters the coherence properties of the system, as reinforced by the extreme linewidth narrowing observed now around $\frac{\delta}{2\gamma} = -3.2$ in Fig. 6.3(b). Note that the nonlinear corrections stem from the matrix elements $2Ub^2$ and $-2Ub^{*2}$. Thus, the higher-dimensional eigensystem attains precedence over the linear model when the product $U|b|^2$ becomes comparable to Γ. However, in the event that $U|b|^2 \ll \Gamma$, the nonlinearity acts merely as a perturbation. It is precisely in this weakly anharmonic regime that our sensing proposal holds relevance.

6.4 Summary

In summary, we have proposed a dissipative test bed that shows enhanced sensitivity to Kerr nonlinearity of the mode, hence qualifying it as a prototypical agency to gauge the strength of anharmonic perturbations under optimal conditions. The sensitivity to anharmonicities can be traced down to the existence of a remarkably long-lived eigenmode of the linear system, characterized by a vanishing linewidth. The physical origin of this peculiar behaviour lies in an effective coupling induced between the cavity and the magnon modes in the presence of a shared ancillary reservoir. Optimal results vis-à-vis the estimation of nonlinearity are obtained when VIC strongly dominates,

i.e., when spontaneous emissions from the modes to the surrounding environments become negligible in comparison to the waveguide-mediated coupling. Higher drive powers lead to new domains of VIC on account of strongly anharmonic responses. The precise implications of these new VICs would be a subject of future study. To provide numerical estimates, our analysis has been tailored to demonstrate a pronounced sensitivity in the context of magnonic excitations. Nonetheless, the essence of our assessment would be applicable to any two-mode nonlinear system.

7. ULTRA-LOW THRESHOLD BISTABILITY AND GENERATION OF A LONG-LIVED MODE[1]

The manipulation of coherent coupling in hybrid quantum systems has been a cornerstone of research in quantum optics and information processing for several years. From classical to quantum, the unremitting quest for superior information processing algorithms and technologies has driven the field into the next dimension [2–4, 13, 174]. Researchers were able to maneuver the dynamics of quantum systems in developing cutting-edge machinery for information processors, involving, for example, atoms [10], trapped ions [11], spins [6], superconducting circuits [5] and more. However, there exists no single all-encompassing quantum system capable of holding up to all the requirements and vital performance metrics of a modern-day signal-processing network. A photon, in spite of being a low-noise carrier of information, suffers from low storage potential. However, integrated photonic circuits [7, 8], which exploit strong light-matter interaction, seem to be progressively holding the leverage in the design of chip-scale information-processing devices with multitasking capabilities.

Recently, hybrid optomagnonic systems utilizing ferrimagnetic materials like YIG have gained traction among the optics community [1, 20–34, 38, 39]. YIGs are endowed with high spin density and the collective motion of these spins is embodied in the form of quasiparticles named magnons. Strong coherent coupling between photons and magnons has been used to realize an array of quantum and semiclassical effects including, but not restricted to, squeezing [31], entanglement [32, 33, 39], multistability [1, 38], exceptional points [30] and dark modes [24]. In 2018, Harder *et al* observed a dissipative form of magnon-photon coupling [66] underscored by the attractive nature of the eigenmodes, otherwise known as level crossing [67–70, 72]. While coherent coupling stems from the spatial overlap between two modes, dissipative coupling can be

[1] A major part of this chapter is reprinted with permission from *Ultralow threshold bistability and generation of long-lived mode in a dissipatively coupled nonlinear system: Application to magnonics* by J. M. P. Nair, D. Mukhopadhyay and G. S. Agarwal, Phys. Rev. B **103**, 224401 (2021), published by the American Physical Society. Collaboration with D. Mukhopadhyay is acknowledged.

engineered by the inclusion of a shared reservoir (typically a waveguide) coupled independently to the two modes. Such an indirect coupling is mediated by a narrow bandwidth of propagating photons supported by the waveguide continuum, with dominant frequencies proximal to the mode transitions. Recently, Yu *et al* [74] used an oscillator model to enunciate the physical origins of dissipative couplings.

It is interesting to note that systematic studies on dissipatively coupled architectures with nonlinear components are far and few between. However, many systems that involve transmon qubits [171] or magnonic excitations [37] have intrinsic anharmonicity, which is often ignored as an inconsequential correction. The essence of our work is to drive home the imperative to examine the nonlinear domain of a dissipatively coupled two-mode system. The nonlinearity induces optical bistability, which finds applications as complex devices like photonic switches [175–177], quantum memories [178, 179] etc. By taking up the model of a dissipative optomagnonic system interfacing with a waveguide channel, we lay bare the prospect of remote transfer of bistability from a spatially separated YIG sphere to a single-mode cavity. As a fruitful consequence, the dissipatively coupled system manifests a remarkably low bistability threshold in contrast to a coherently coupled system with comparable coupling strength. The bistable signature is also mirrored by the modified polariton resonances of the waveguide transmission. In addition, the driven nonlinearity spawns a long-lived eigenmode with ultra-small linewidth leading to anomalous transmission effects like enhanced sensitivity in waveguide transmission, with potential applications in futuristic signal-processing networks.

This chapter is organized as follows. In section 7.1, we develop a theoretical model to investigate the nonlinear response of a two-mode system coupled via an intermediary waveguide. We provide a detailed analysis of the bistability and the critical drive power required to achieve the same. In section 7.2, we explore the specific example of a driven cavity-magnon system. For experimentally realizable values of the system parameters, our simulations demonstrate bistability in the cavity response. In section 7.3, we employ a spectroscopic technique to advance a testable scheme for ratifying the bistability. Sec 7.4 contains a concise description of the higher-

dimensional eignensystem, which is directly responsible for a new domain of coherences. Finally, we summarize our results in section 7.5.

7.1 Bistability threshold in dissipatively coupled systems

Before delving into any particular empirical models, we spell out the theoretical formalism describing a large class of two-mode anharmonic systems. The characteristic Hamiltonian resembling Eq. (2.33) goes as

$$\begin{aligned} \mathscr{H}/\hbar = \omega_a a^\dagger a + \omega_b b^\dagger b + g(ab^\dagger + a^\dagger b) \\ + \mathscr{U} b^{\dagger 2} b^2 + i\Omega(b^\dagger e^{-i\omega_d t} - b e^{i\omega_d t}), \end{aligned} \tag{7.1}$$

where ω_a and ω_b denote the respective resonance frequencies of the uncoupled modes a and b, and g signifies the direct coupling between them. The parameter $\mathscr{U}$ is a measure of the strength of Kerr nonlinearity intrinsic to the mode b and conjured up by an external laser (pump) at frequency ω_d, for which Ω signifies the Rabi frequency. While the Hamiltonian captures the effect of coherent coupling between the modes, a an embodiment of the dissipative coupling introduced by an interposing reservoir entails full recourse to the master-equation formalism. For a two-mode system with a density matrix ρ, the corresponding the master equation would be given by

$$\frac{\mathrm{d}\rho}{\mathrm{d}t} = -\frac{i}{\hbar}[\mathscr{H}, \rho] + \gamma_a \mathscr{L}(a)\rho + \gamma_b \mathscr{L}(b)\rho + 2\Gamma \mathscr{L}(c)\rho, \tag{7.2}$$

where γ_a and γ_b are the intrinsic damping rates of the modes respectively, while the parameter τ is tied to coherences introduced by the common reservoir. $\mathscr{L}$ is the Liouillian defined by its action $\mathscr{L}(\sigma)\rho = 2\sigma\rho\sigma^\dagger - \sigma^\dagger\sigma\rho - \rho\sigma^\dagger\sigma$ and $c = \frac{1}{\sqrt{2}}(a + e^{i\phi}b)$ is the jump operator for symmetrical couplings to the reservoir. Here $\phi = 2\pi L/\lambda_0$ symbolizes the phase difference between the two couplings, where λ_0 represents the resonant wavelength and L denotes the spatial separation between a and b. Assuming the wavelength of the resonant mode to be much bigger than the spatial separation, it makes sense to approximate $\phi \approx 0$. In the rotating frame of the laser drive, the mean value equations for a and b would be obtained as

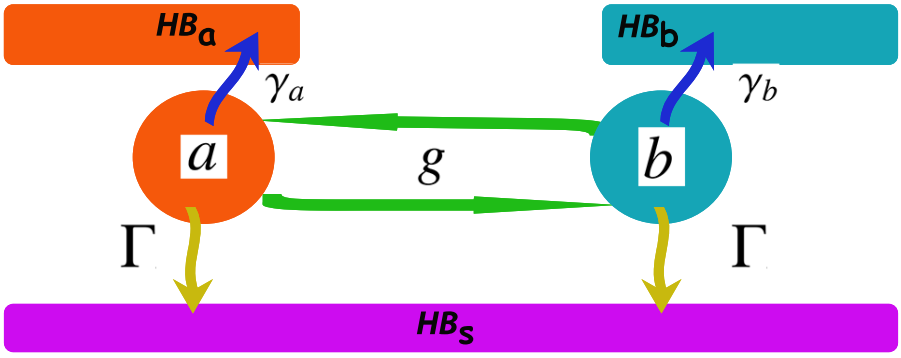

Figure 7.1: General two-mode system, with both coherent and dissipative pathways of interaction. HB_α = heat bath of mode α, with $\alpha = S$ denoting a shared reservoir.

$$\begin{pmatrix} \dot{a} \\ \dot{b} \end{pmatrix} = -i \begin{pmatrix} \delta_a - i(\gamma_a + \Gamma) & g - i\Gamma \\ g - i\Gamma & \delta_b - i(\gamma_b + \Gamma) \end{pmatrix} \begin{pmatrix} a \\ b \end{pmatrix} + 2\mathscr{U}(b^\dagger b) \begin{pmatrix} 0 & 0 \\ 0 & 1 \end{pmatrix} \begin{pmatrix} a \\ b \end{pmatrix} + \begin{pmatrix} 0 \\ \Omega \end{pmatrix}, \tag{7.3}$$

where $\delta_i = \omega_i - \omega_d$ $(i = a, b)$. For brevity, $\langle ... \rangle$ notations have been excluded. Invoking the mean-field approximation allows one to decouple the higher-order expectations as $\langle \xi_1 \xi_2 \rangle = \langle \xi_1 \rangle \langle \xi_2 \rangle$, so that $\left\langle b^\dagger b b \right\rangle$ essentially reduces to $|b|^2 b$.

Purely dissipative models can be pinned down by the choices $g = 0$ and $\Gamma \neq 0$. Within this category, one can achieve an anti-$\hat{PT}$ symmetric mode hybridization by tuning the control field to a frequency such that $\delta_b = -\delta_a = \delta/2$ and by enforcing equal damping rates $\gamma_a = \gamma_b = \gamma_0$. Such models then satisfy $\{\hat{PT}, \mathscr{H}\} = 0$, where $\{.,.\}$ stands for the anti-commutator. When the stability criterion is fulfilled, the time-dependent solutions decay into a stationary value in the long-time limit, i.e. $(a, b) \to (a_0, b_0)$, which can be easily derived from Eq. (7.3) by setting $\dot{a} = \dot{b} = 0$. These

stationary values are, therefore, entwined via the constraints

$$(2\gamma - i\delta)a_0 + 2\Gamma b_0 = 0,$$
$$(2\gamma + i\delta)b_0 + 4i\mathscr{U}|b_0|^2 b_0 + 2\Gamma a_0 - 2\Omega = 0, \tag{7.4}$$

where $\gamma = \gamma_0 + \Gamma$. So γ_0 represents the spontaneous rate of emission into the local heat baths. Eliminating b_0, one has a polynomial equation for $y = |a_0|^2$, predicting bistability in the ensuing response,

$$\frac{\beta^2}{\Gamma^2}y - 2\mathscr{U}\beta\delta\frac{\gamma^2 + (\delta/2)^2}{\Gamma^4}y^2 + 4\mathscr{U}^2\frac{(\gamma^2 + (\delta/2)^2)^3}{\Gamma^6}y^3 = I, \tag{7.5}$$

with the definitions $\beta = \Gamma^2 - \gamma^2 - (\delta/2)^2$ and $I = \Omega^2$. Note, *en passant*, that this bistability is not ingrained in mode a, rather, it is transferred from the anharmonic mode b. The turning points of the bistability curve can be gleaned from the expression above by inspecting the solutions to $\frac{\mathrm{d}I}{\mathrm{d}y} = 0$, which turn out to be

$$y_\pm = \frac{\beta\Gamma^2}{6\mathscr{U}[\gamma^2 + (\delta/2)^2]^2}\left[\delta \pm \sqrt{(\delta/2)^2 - 3\gamma^2}\right]. \tag{7.6}$$

Thus, the condition for observing bistable signature can be encoded as: $\mathscr{U}\delta < 0$ and $\delta^2 > 12\gamma^2$. In addition, there is a cutoff value for the pump power beyond which the bistable characteristics set in. The appropriate magnitude of $I^{(c)}$ pertains to the inflection point in the $I - y$ graph and can be inferred from the conditions $\frac{\mathrm{d}I}{\mathrm{d}y} = \frac{\mathrm{d}^2I}{\mathrm{d}y^2} = 0$. For any generic two-mode system with the interaction comprising both coherent and dissipative components, i.e. $g \neq 0, \Gamma \neq 0$, the cutoff power obeys the relation

$$I^{(c)} = \frac{1}{432}\frac{[\sqrt{3}(4\gamma^2 - \Gamma^2 + g^2)\mathrm{sgn}(\mathscr{U}) + 2g\Gamma]^3}{\mathscr{U}\gamma^3}, \tag{7.7}$$

where sgn(x) is +1 when $x > 0$ and −1 for $x < 0$. For all the subsequent analyses in this paper, we

shall work with the assumption $\mathscr{U} > 0$. The precise ramifications of the expression (7) in relation to the nature of coupling can be understood by comparing the cutoffs for coherently coupled and dissipatively coupled systems by letting $\Gamma = 0$ and $g = 0$ respectively. This leaves us with

$$\frac{I_{dis}^{(c)}}{I_{coh}^{(c)}} = \left(\frac{4\gamma^2 - \Gamma^2}{4\gamma^2 + g^2}\right)^3, \tag{7.8}$$

where we have assumed that the two kinds of systems decay effectively at the same rate. Note that for $\Gamma \neq 0$ and $g \neq 0$, the expression above is always less than one. Stated differently, a dissipatively coupled system demonstrates a lower bistability threshold when compared to a coherently coupled system with identical coupling strength. More importantly, we can achieve an extremely low threshold in a dissipatively coupled system by signifiicantly boosting the waveguide-mediated interaction relative to the intrinsic damping, such that $\gamma \approx \Gamma$. To put this into perspective, for two systems with identical coupling strengths, that is $\Gamma \approx g$, the quantity in Eq. (7.8) goes over to a finite value equaling 0.22 as $\gamma \to \Gamma$. Despite the fact that a dissipatively coupled system showcases remarkably low bistability threshold, the 78% advantage is the best that can be attained in an experimental apparatus.

7.2 Dissipatively coupled nonlinear magnonic system

To give substance to the foregoing discussion on dissipatively coupled systems, we consider a hybrid optomagnonic apparatus that has already evolved into a topical system of experimental activities. Our setup consists of a single-mode optical cavity and a YIG sphere separated by some finite distance and interacting dissipatively with each other via an intermediary one-dimensional waveguide, as illustrated in Fig. 7.2. The intrinsic anharmonicity of the YIG [37] is kindled by a microwave laser acting as the pump. The Hamiltonian of this driven system can be laid out as

$$\mathscr{H}/\hbar = -\gamma_e B_0 S_z + \gamma_e^2 \frac{\hbar K_{\text{an}}}{M^2 V} S_z^2 + \omega_a a^\dagger a + \mathscr{H}_\Omega, \tag{7.9}$$

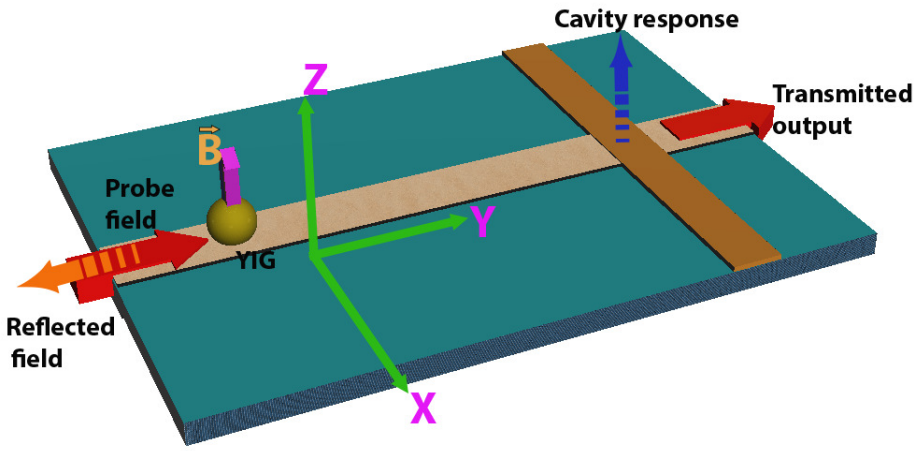

Figure 7.2: Schematic of a YIG sphere interacting remotely with a single-mode cavity, with the coupling mediated by a waveguide. (Redrawn from *Phys. Rev. Lett.* ***125****, 147202 (2020).*)

where $\mathscr{H}_\Omega = i\hbar\Omega\left(m^\dagger e^{-i\omega_d t} - m e^{i\omega_d t}\right)$, B_0 is the static magnetic field applied along the $+\hat{z}$ direction, $\gamma_e = e/m_e c$ is the gyromagnetic ratio for electron spin and $\mathbf{S}$ the collective spin operator of the YIG. The quantity $\mathbf{M} = \gamma_e \mathbf{S}/V$ denotes the magnetization, where V is the volume of the YIG. The second term in Eq. (7.9) stems from the magnetocrystalline anisotropy. The parameter ω_a represents the cavity resonance frequency and a ($a^\dagger$) characterizes the annihilation (creation) operator of the cavity. Invoking the Holstein-Primakoff transformation [85] in the limit of large spin, the above Hamiltonian simplifies to Eq. (7.1) with $g = 0$, frequency $\omega_b = \gamma_e B_0 - \frac{2\hbar\gamma_e^2 S K_{\rm an}}{M^2 V}$, $\mathscr{U} = \frac{\gamma_e^2 K_{\rm an}}{M^2 V}$. The Bosonic operators $(b, b^\dagger)$, which represent the magnonic quasiparticle, are related to the spin operators as $S^+ = \sqrt{2S}b, S^- = \sqrt{2S}b^\dagger$ in the limit $S \gg \langle b^\dagger b\rangle$. Here, $S = \frac{5}{2}\rho V$ is the collective spin of the YIG, with the Fe^{3+} ion density and the diameter of the YIG given by $\rho = 4.22 \times 10^{27}$ m^{-3} and $d = 1$ mm respectively. The Rabi frequency $\Omega = \gamma_e \sqrt{\frac{5\pi\rho d D_{\rm p}}{3c}}$ is determined by the system characteristics as well as the pump power D_p. Here, c stands for the speed of light. As discussed in the general setting, the cavity signal satisfies the multistable equation expressed in Eq. (7.5). In Fig. 7.3(a), we plot the optical response against various pump powers. As we slowly ratchet up the drive power, an abrupt jump is observed in the signal as opposed to the fairly linear ascent in the domain of weaker drives. A similar precipitous transition is seen as we tamp down the drive power,

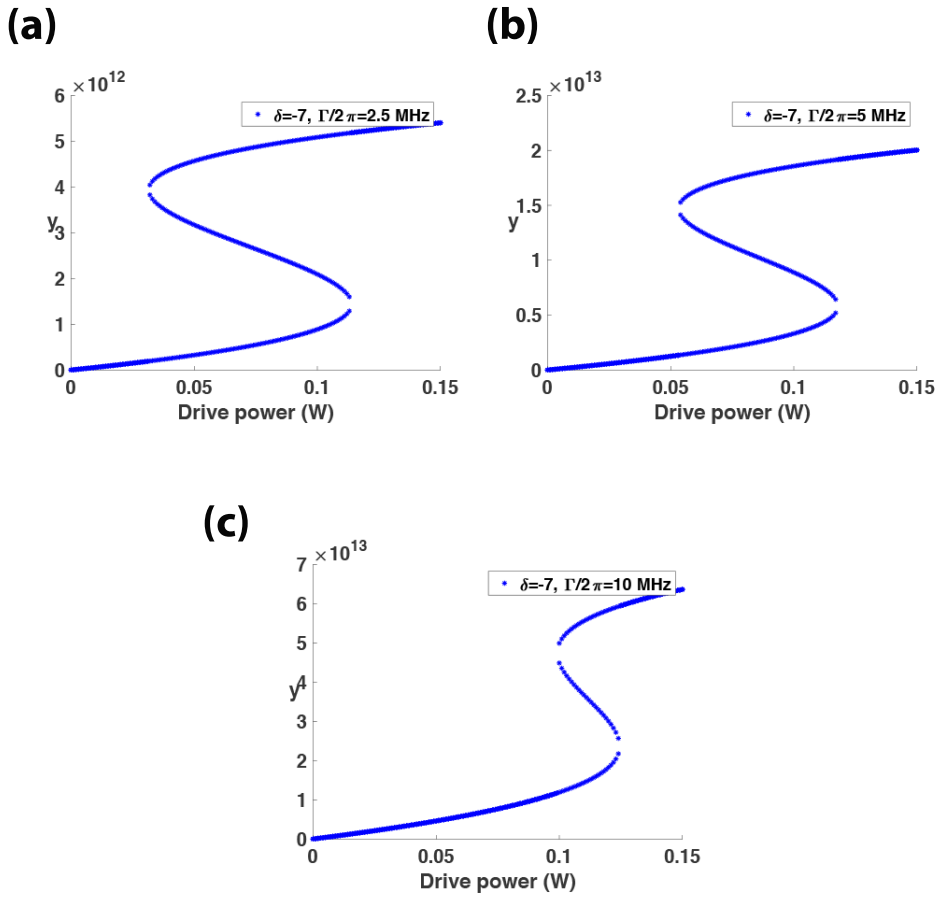

Figure 7.3: Response in the cavity field plotted against the pump power, for varying strengths of the dissipative coupling. Weaker dissipative couplings support larger ranges of the drive power pertaining to bistable states in the response. The parameters $\gamma_0/2\pi = 5$ MHz and $\mathscr{U}/2\pi = 42.1$ nHz.

this time at a different point, unravelling the transfer of bistability to the cavity. This is analogous to the optical bistability reported in a coherently coupled cavity-magnon system [1], in which the nonlinear resource (YIG) is contained in the cavity. However, the paradigm we explore has the antithetical underpinnings of spatial separation being the source of coupling, as the YIG is only remotely interacting with the cavity. A boost in the dissipative coupling brings about a diminishing window of bistability, as illustrated in Fig. 7.3(b)-(c). This bears stark disparities with coherently coupled systems, where a stronger coupling widens the region of bistability. Nevertheless, this feature turns out to be quite advantageous as we can generate broader bistability windows for modest values of the engineered dissipative coupling. The observed bistability is fairly robust against intrinsic damping rates of the modes, as evident from Figs. 7.3(a)-(d).

It makes for a relevant observation that as the dissipative coupling is downsized, not only is the bistability window broadened but the effect is also rendered accessible at lower drive powers. This seems to be a subtle point of divergence between directly and indirectly coupled systems. That said, one cannot, of course, make the dissipative coupling indefinitely weak and still expect to harness bistable signatures to one's advantage. This is a trivial consequence of the fact that weak couplings cannot elicit strong responses from the cavity.

7.3 Probes of bistability via the waveguide transmission

Spectroscopy is a quintessential tool in science and engineering, and is routinely applied to QED systems. The fundamental spectroscopic principle of is to probe the system using a weak electromagnetic excitation, and from the transmission properties of the system, one extracts key information about the system, including, but not limited to, its eigenmode configuration. Here, we employ a similar technique to investigate the transmission properties of the nonlinear opto-magnonic device with varying drive powers, as depicted in Fig. 7.2. Specifically, we show how anharmonicity-induced shifts in the polariton minima reinforce the bistable nature of cavity signal. In the presence of a monochromatic probe field guided through the fiber, the Hamiltonian in Eq. (7.1) gets modified to $\mathscr{H} + \varepsilon\mathscr{H}'$, where $\mathscr{H}' = i\hbar[(a^\dagger + b^\dagger)e^{-i\delta_p t} - h.c.)]$, $\delta_p = \omega_p - \omega_d$,

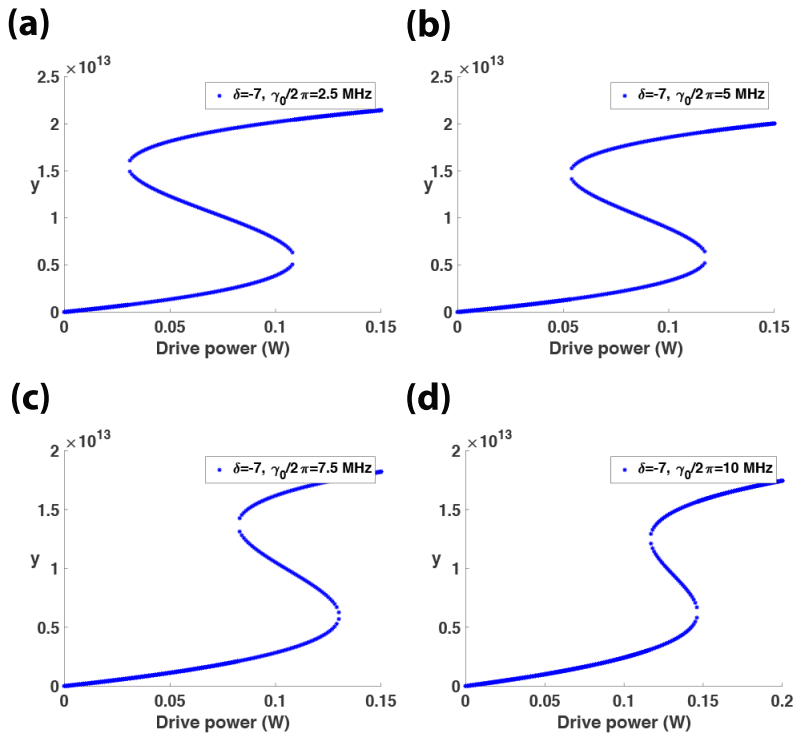

Figure 7.4: Effect of intrinsic damping on the optical bistability. Other parameters are $\Gamma/2\pi = 5$ MHz and $\mathscr{U}/2\pi = 42.1$ nHz. The detunings are scaled down by a factor $S = 2\pi \times 20$ MHz.

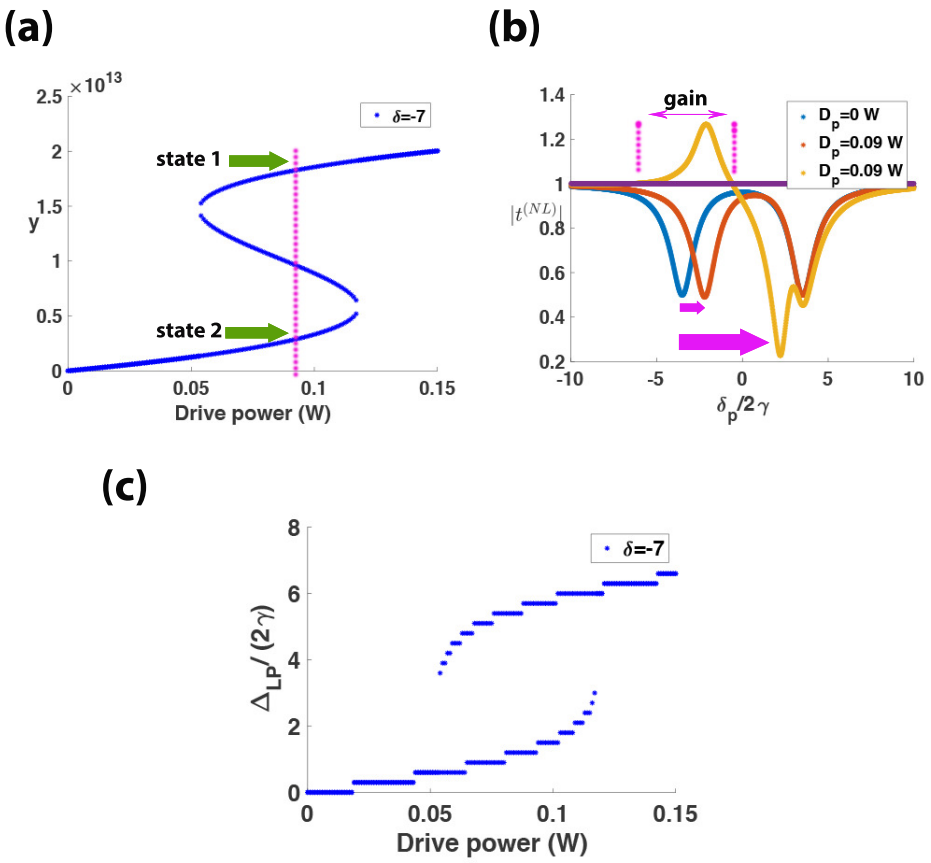

Figure 7.5: (a) The cavity response plotted against the pump power showcasing the two stable states at $D_p = 90$ mW. (b) Transmission spectra through the waveguide as a function of the scanning frequency. (c) Shifts in lower polariton frequency vs. the pump power D_p. Other parameters are $\Gamma/2\pi = 5$ MHz, $\gamma_0/2\pi = 5$ MHz and $\mathscr{U}/2\pi = 42.1$ nHz. Scaling factor for detunings $S = 2\pi \times 20$ MHz.

$\varepsilon = \sqrt{2\Gamma \mathscr{P}_\varepsilon/\hbar\omega_p}$ and $\mathscr{P}_\varepsilon$ is the probe power. The updated Langevin equations then entail

$$\begin{aligned}\dot{a} &= -(-i\delta/2 + \gamma)a - 2\Gamma b + \varepsilon e^{-i\delta_p t},\\ \dot{b} &= -(i\delta/2 + \gamma)b - 2i\mathscr{U}|b|^2 b - \Gamma a + \Omega + \varepsilon e^{-i\delta_p t}.\end{aligned} \tag{7.10}$$

The solution to this set of equations in the long-time limit can be written as a Fourier series expansion,

$$a = \sum_{n=-\infty}^{\infty} a_{(n)} e^{-in\delta_p t}, \quad b = \sum_{n=-\infty}^{\infty} b_{(n)} e^{-in\delta_p t}, \tag{7.11}$$

where $a_{(n)}$ and $b_{(n)}$ are the amplitudes associated with n-th harmonic of the probe frequency. The steady components a_0, b_0, which are actually oscillating at the pump frequency, conform to Eq. (7.4). The probe being a weak field, we ignore the higher-order terms and truncate the series with n running up to ± 1. Utilizing Eqs. (7.10) and (7.11), we conclude the following set of linear equations for the oscillating components of the steady state:

$$\mathscr{M} X^{(1)} = F_\varepsilon, \tag{7.12}$$

where $\mathscr{M} = \begin{pmatrix} \mathscr{A} & \mathscr{B} \\ \mathscr{B}^* & \mathscr{C} \end{pmatrix}$, $X^{(1)} = (a_+, b_+, a_-^*, b_-^*)^T$, $F_\varepsilon = \varepsilon(1,1,0,0)^T$, with the elements $\mathscr{A} = \begin{pmatrix} \gamma - i(\delta/2 + \delta_p) & \Gamma \\ \Gamma & -\gamma + i(\tilde{\Delta} + \delta_p) \end{pmatrix}$, $\mathscr{B} = \begin{pmatrix} 0 & 0 \\ 0 & 2i\mathscr{U} b_0^2 \end{pmatrix}$, $\mathscr{C} = \begin{pmatrix} \gamma - i(\delta/2 - \delta_p)) & \Gamma \\ \Gamma & \gamma - i(\tilde{\Delta} + \delta_p) \end{pmatrix}$, and $\tilde{\Delta} = \frac{\delta}{2} + 4\mathscr{U}|b_0|^2$. The first-order fluctuations about the steady state can then be obtained numerically by inverting Eq. (7.12). Using the input-output relation $\varepsilon_t = \varepsilon - 2\Gamma(a+m)$, where ε_t designates the transmitted signal, we obtain the transmission coefficient at the probe frequency,

$$\begin{aligned} t^{(NL)} = \varepsilon_t/\varepsilon &= 1 - 2\Gamma(a_+ + m_+)/\varepsilon \\ &= 1 + 2\Gamma \sum_{r,s=1}^{2} (\mathscr{M}^{-1})_{rs}. \end{aligned} \tag{7.13}$$

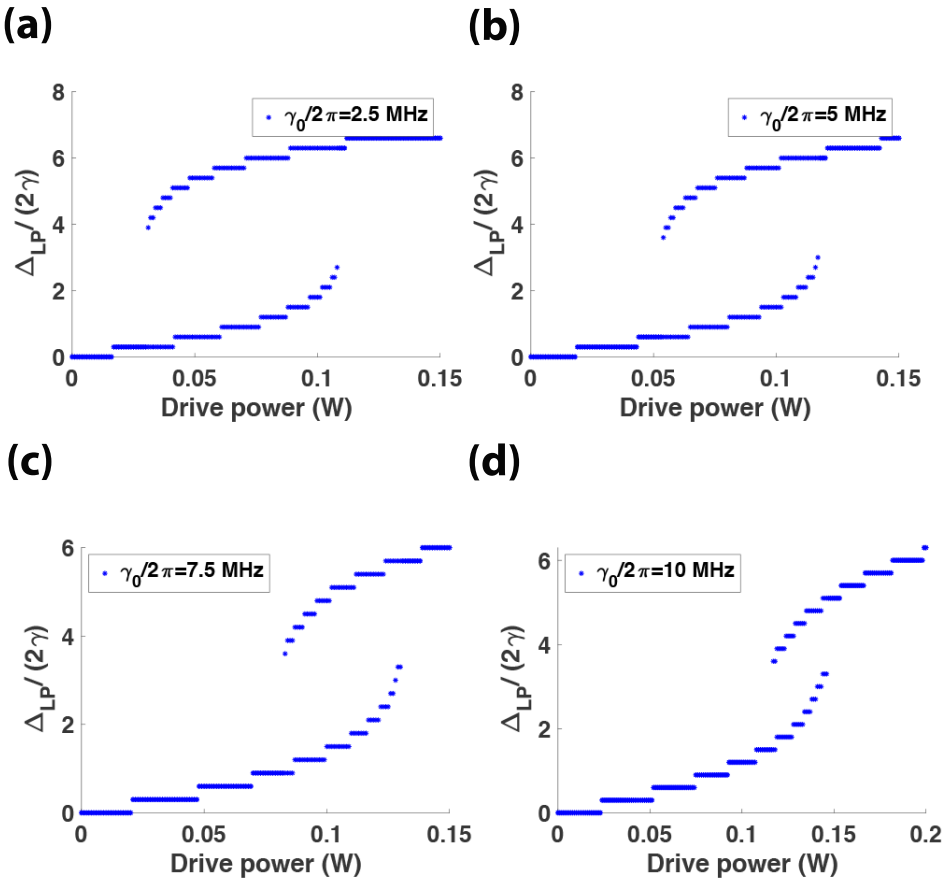

Figure 7.6: The lower polariton frequency shifts against pump power D_p for varying values of the intrinsic damping. All the other parameters are identical to Fig. 7.4.

In the absence of a pump, when nonlinear effects remain dormant, the Rabi splitting between the cavity-magnon polariton branches is substantiated in Fig. 7.5 (a). For a nonzero drive power, under conditions of bistability, the higher polariton resonance remains largely unscathed while the lower polariton sustains appreciable frequency shifts. Here, lower and higher polaritons (LP and HP) refer to the polariton branches with lower (appearing on the left) and higher (appearing on the right) frequencies in the transmission spectra. The respective minima are labelled as δ_{LP} and δ_{HP}. The bistability in transmission is illustrated with two stable transmission spectra in Fig. 7.5(a) at drive power 0.09 W. In addition, we draw information on the hysteresis curve in Fig. 7.3 by

investigating shifts in the lower polariton minima. We numerically obtain the corresponding shifts in polariton frequency $\Delta_{\rm LP} = \delta_{\rm LP}$-$\delta^{(0)}_{\rm LP}$ as a function of input (pump) power, where $\delta^{(0)}_{\rm LP}$ is the detuning of the lower branch at zero drive power. The bistability gets manifested in the frequency shifts in Fig. 7.5 (c), which replicate the pattern of the spincurrent curve in Fig. 7.3 (b). Further, we provide the frequency-shift curves (Figs. 7.6(a)-(d)) against the intrinsic decay parameters of the cavity and magnon modes, testifying to the robustness of bistability against extraneous decoherence.

7.4 Anharmonicity-induced long-lived mode

In this section, we show how the presence of nonlinearity activates new coherences, which, in turn, introduces optical anomalies in the fiber transmission. Owing to its nonlinear nature, the system of coupled-mode equations in Eq. (7.10) does not yield readily to a Hamiltonian-based analysis. However, an effective Hamiltonian can be eked out by appealing to a linearized approximation about the steady state, *viz.* $a(t) = a_0 + \delta a(t)$, $b(t) = b_0 + \delta b(t)$. The fluctuations $\delta a(t)$ and $\delta b(t)$ are presumed to be general, albeit small in relation to a_0 and b_0. This permits the dismissal of higher-order effects in these variations, akin to what was invoked in the last section. The variables $\delta b(t)$ and $\delta b^{\dagger}(t)$ get interlinked due to the anharmonicity. The inter-coupling is, of course, too weak to bear on any observable effects at smaller drive powers. However, a drive power around 0.02 W makes this coupling paramount. Defining $Y(t) = Y + \delta\xi(t)$, where $Y(t) = \begin{pmatrix} a(t) & b(t) & a^{\dagger}(t) & b^{\dagger}(t) \end{pmatrix}^T$ and $Y = \begin{pmatrix} a & b & a^{\dagger} & b^{\dagger} \end{pmatrix}^T$ are both 4-element vectors, the Langevin equations reduce to a linear dynamical model, $\left[\dfrac{\mathrm{d}}{\mathrm{d}t} + i\mathscr{H}_{NL}\right]\delta\xi(t) = \mathscr{E}_{in}(t)$, with

$$\mathscr{H}_{NL} = \begin{pmatrix} -\frac{\delta}{2} - i\gamma & -i\Gamma & 0 & 0 \\ -i\Gamma & \tilde{\Delta} - i\gamma & 0 & 2\mathscr{U} b_0^2 \\ 0 & 0 & \frac{\delta}{2} - i\gamma & -i\Gamma \\ 0 & -2\mathscr{U} b_0^{*2} & -i\Gamma & -\tilde{\Delta} - 2i\gamma \end{pmatrix}, \tag{7.14}$$

$\mathscr{E}_{in}(t) = \varepsilon\begin{pmatrix} e^{-i\delta_p t} & e^{-i\delta_p t} & e^{i\delta_p t} & e^{i\delta_p t} \end{pmatrix}^T$ and $\tilde{\Delta}$ has been defined in relation to Eq. (7.12) earlier. A straightforward comparison with Eq. (7.12) reveals that $\mathscr{M} = i(\mathscr{H}_{NL} - \delta_p)$, implying that an-

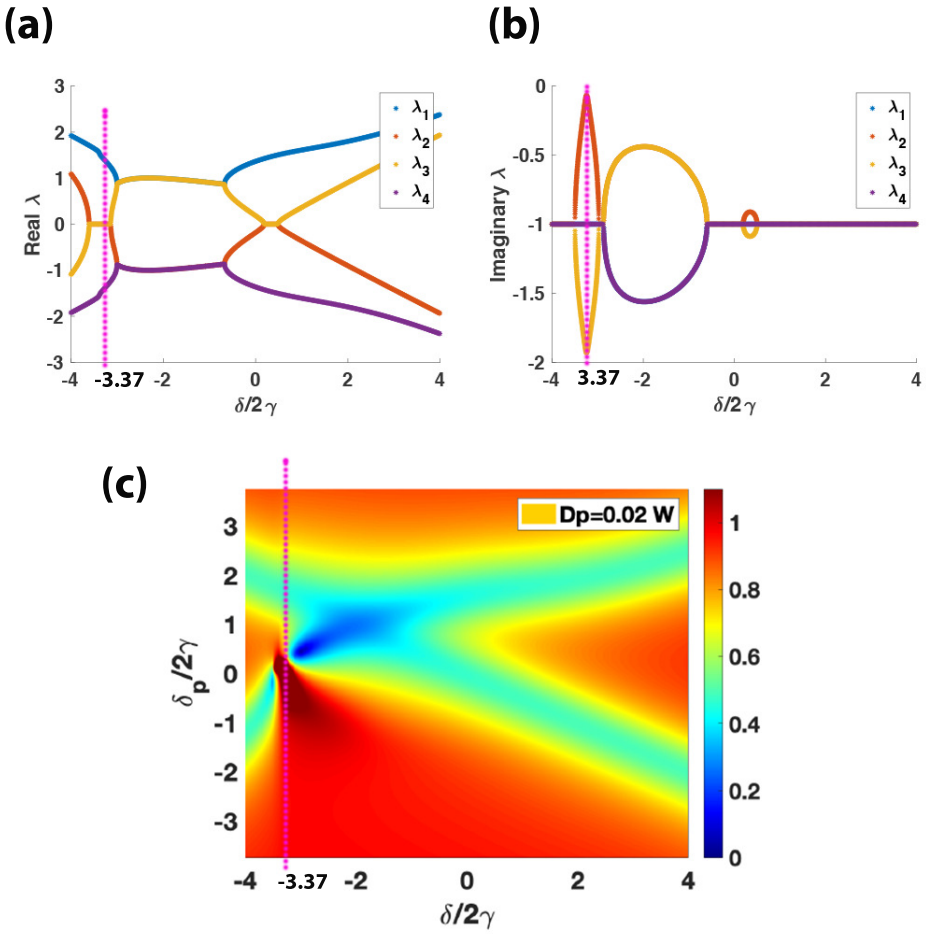

Figure 7.7: (a) Real parts and (b) Imaginary parts of the eigenvalues of $\mathscr{H}_{NL}$ plotted against δ at $Dp = 0.02$ W. (c) $|t|$ is plotted against δ_p and δ at the same pump power. The vertical lines in (a), (b) and (c), all at $\delta/2\gamma = -3.37$, identify the exceptionally long-lived mode with extreme linewidth suppression. Other parameters are identical to Fig. 7.5.

harmonic resonances of the system are tied to the eigenmodes of $\mathscr{H}_{NL}$. Any exotic properties of eigenmodes would, therefore, be translated to observable anomalies in the transmission signal. The eigenfrequencies denoted as λ_i's, with i running from 1 through 4, manifest characteristics attributable to level attraction. This is portrayed, for $D_p = 0.02$ W and $\mathscr{U}/2\pi = 42.1$ nHz in Fig. 7.7(a), (b). Since the effective dimensionality of the Hilbert space is augmented by the introduction of anharmonicity, a major impact of $\mathscr{U}$ is to bring in new coherent phenomena in the transmission across the hybridized cavity-magnon system. As Figs. 7.7(c) and Fig. 7.8(a)-(d) reveal, the nonlinear coupling categorically skews the transmission lineshapes by introducing asymmetry. However, the case of negative magnon detunings turns out to be particularly intriguing, as a new transparency window crops up, which owes its origin to a long-lived mode of the system. With a significant Rabi frequency ($D_p \sim 0.02$ W), the enhanced pumping rate is brought to bear on the linewidths and one of them shrinks close to nought, leading to a region of highly elevated transmission levels. This is highlighted by a dark red smeared out streak shown in Fig. 7.7(c), and also illustrated for better clarity in Figs. 7.8(a), (b) where the transmission is plotted for a pair of fixed values of delta. The near-perfect transmission comes to light most prominently around $\delta/2\gamma = -2.1$, for the chosen set of system parameters. In fact, at this precise magnitude of the detuning, the waveguide photon gets transmitted unimpeded, demonstrating perfect transparency. Equally interesting is the collateral emergence of a strongly reflecting polariton minimum. Such fundamentally conflicting behaviors transpire in a narrow neighborhood around $\delta_p = 0$ across which the device flips between a state of unidirectional reflection $\left(\left|t^{(NL)}\right| \ll 1\right)$ to complete transparency $\left(\left|t^{(NL)}\right| \approx 1\right)$. This conspicuous result suggests practical advantages in engineering driven systems for implementing nonlinearity-assisted strong signal switching.

However, as evidenced by Fig. 7.7(c), although the switching effect seems to be further amplified as δ becomes more strongly negative, we find an obtrusive region of pump-induced gain that makes the transmission surge past unity. Fig. 7.8(c) depicts an extraordinarily high transmission peak around $\delta/2\gamma = -3.37$, at which the imaginary part of one of the poles (marked by yellow in 7(a), (b)) moves tantalizingly close to zero while the corresponding eigenfrequency remains

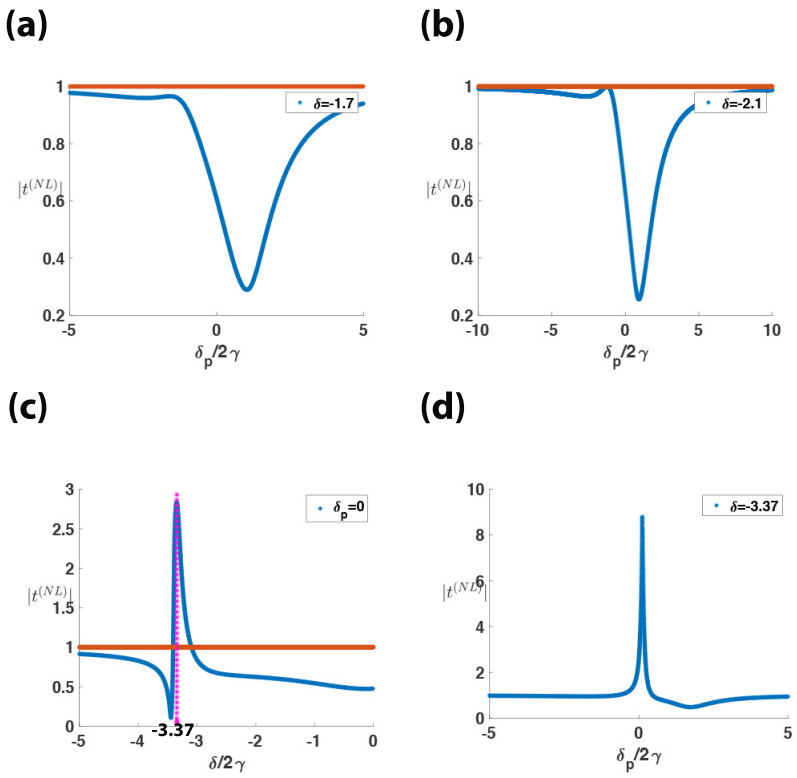

Figure 7.8: Figures (a), (b) represent the transmission spectra against the probe detuning δ_p at two different values of δ, portraying the asymmetry and the transition from unidirectional reflection to perfect transmission. (c) Transmission spectra against δ with $\delta_p = 0$, highlighting a region of significant gain around $\delta/2\gamma = -3.7$. (d) Transmission plot demonstrating pronounced sensitivity around $\delta_p = 0$. Other parameters are identical to Fig. 7.5. Scaling factor for detunings $S = 2\pi \times 20$ MHz.

approximately zero. This is why the signal dramatically shoots up around $\delta_p = 0$. Additionally, it demonstrates a sharp sensitivity to the probe frequency, which is also responsible for the signal flipping effect. The spectacular sensitivity in the signal can be accredited to the existence of a second-order pole at $\delta_p \approx 0$, $\delta/2\gamma \approx -3.37$ in the derivative of the transmitted signal, i.e.

$$\frac{\partial t^{(NL)}}{\partial \delta_p} = 2i\Gamma \sum_{r,s=1}^{2} \{\mathscr{M}^{-2}\}_{rs}. \tag{7.15}$$

The above relation follows from the consideration that $\mathscr{M}^{-1}(\delta_p + \eta) - \mathscr{M}^{-1}(\delta_p) = i\eta\mathscr{M}^{-1}(\delta_p + \eta)\mathscr{M}^{-1}(\delta_p)$ and subsequently taking the limit $\eta \to 0$. One should, in practice, exercise caution by avoiding excessive gain, as any unduly long-lived mode with negligible width augurs a breakdown in the validity of linearized approximations to the steady state and requires a nonlinear treatment of the probe. Nonetheless, even if one avoids this unstable terrain of extraordinary transmission, one could carefully configure the detuning δ to enable transparent behavior and strong signal sensitivity near to $\delta_p = 0$ as discernible from Fig. 7.8(d). In this connection, we also note that sensitivity in dissipatively coupled systems has been studied in the context of linear perturbations [180], and more recently, for the detection of weak anharmonicities in an optomagnonic model [80].

7.5 Summary

To summarize, our foray into the nonlinear domain of dissipatively coupled models sheds light on two fundamental anharmonic signatures of driven systems: optical bistability and anharmonicity-induced coherences. Directly coupled nonlinear systems, such as a YIG sphere in a cavity, are already known to generate bistability. Our formulation demonstrates that dissipatively coupled models, like the one we study here, accords a lower pumping threshold for observing bistable states. In the context of an optomagnonic system, the frequency shifts in the polariton minima bring out the essential hallmarks of bistability, in lockstep with the cavity response. With the anharmonicity factored in, the increased dimensionality of an intricate but predominantly stable eigensystem imparts higher-order coherences to the hybridized polaritons, the significance of which is accentuated by an enhanced pumping rate. Simulation of the transmission across the waveguide reveals a

parameter regime of pump-induced gain, where external energy is funneled into the fiber causing a coherent buildup of the output signal. The anharmonic gain is hardly an adventitious effect, but, rather, an upshot of intense linewidth inhibition in one of the resonances. This long-lived mode is also responsible for extreme sensitivity in the signal to the probe frequency. Fortuitously, the existence of a transmission window, flanking a polariton minimum, extends well into the stable regime. In this regime, the system demonstrates a stark duality in signal transport, marked by the possibility of achieving both transparency and opacity, for the same set of system parameters. The greater signal sensitivity and control incorporated by the anharmonicity could be harnessed for the design of photonic devices with optical switching properties.

8. CAVITY-MEDITATED LEVEL ATTRACTION AND REPULSION BETWEEN MAGNONS[1]

The expedient control of coherent magnon-photon coupling in hybrid cavity-spintronic systems has laid bare a plethora of new avenues for magnon-based quantum information transfer [1, 20–34, 38, 39, 81]. The collective spin-wave excitations called magnons in magnetic systems can efficiently interface with microwave photons, thereby consolidating the strength of dispersive interaction to produce well-separated hybridized states demonstrating level repulsion and Rabi oscillations [181, 182]. Complementary to the phenomenon of coherent magnon-photon coupling in a cavity, there exists a paradigm of dissipative coupling wherein the magnon mode interacts with the modes of a waveguide [66, 73]. In contrast to the mode anticrossing in dispersively coupled systems, dissipative coupling induces level attraction characterized by the coalescence of the polariton modes at the exceptional points (EPs) as demonstrated in recent experiments [67–70, 72]. Note that general perspectives on EPs and diabolic points have been widely explored [183, 184]. Considering the ubiquity of both coherent and dissipative couplings in cavity-magnonics as well as the wide disparity in the resulting physics, the competing effects of these couplings have evoked significant interest of late. Consequently, cavity-magnonics has emerged as a premier platform to translate some of the foremost ideas of non-Hermitian optics into scalable quantum technologies with novel, multitasking capabilities. By exploiting strongly coupled magnon-photon systems, a plenitude of exotic effects have been brought to the fore, some of which include single-spin detection [185] and manipulation of spin current [23, 186], polaritonic dark modes [24, 187] and magnonic quintuplets [188], observation of coherent perfect absorption and exceptional point [30], multistability [1, 38], squeezing [31] and entanglement [32, 33, 39], sensing of anharmonicities [80], and bidirectional microwave-to-optical transduction [35, 189, 190].

Owing to its potential applications in topological energy transfer [135, 191, 192] and quantum

[1]A major part of this chapter is reprinted with permission from *Cavity-mediated level attraction and repulsion between magnons* by J. M. P. Nair, D. Mukhopadhyay and G. S. Agarwal, Phys. Rev. B **105**, 214418 (2022), published by the American Physical Society. Collaboration with D. Mukhopadhyay is acknowledged.

sensing [137, 141, 143, 180, 193, 194], there has been a proliferation of efforts within the optics and condensed matter community to realize level attraction in hybrid non-Hermitian systems. So far, this effect has been successfully showcased in cavity-optomechanical systems [173], and cavity-magnonic configurations integrated with waveguides [76] and split-ring resonators [67, 68]. It is well known that two coherently coupled harmonic systems naturally exhibit level repulsion while dissipatively coupled systems are characterized by level attraction. Therefore, a customary technique to implement level crossing lies in mitigating the effect of dispersive interaction relative to its dissipative counterpart. Both dispersive and dissipative couplings naturally occur in qubits interacting with electromagnetic vacuum or with the modes of a poor cavity [126].

In the context of magnonics, magnon-photon level repulsion and level attraction have both been experimentally realized [66–70, 72, 73]. In this work, we explore the distinctive qualities of magnon-magnon hybridization in a system of two non-interacting magnetic systems coherently coupled to a microwave cavity. We show that the mediating effect of the intracavity field brings to bear the dual possibilities of effecting both level anticrossing and level crossing in two distinct parameter regimes. Much to our anticipation, strong magnon-photon couplings result in well-separated polaritonic states, or normal modes, characterizing level repulsion. Curiously, however, we observe that the central peak is washed out when the frequencies of the bare modes are matched to resonance and the magnons are symmetrically coupled to the cavity mode. As the symmetry is broken and the magnons are antisymmetrically detuned relative to the cavity mode, the dark polariton gets reexcited on account of energy transfer from the bright modes. The contrary feature of level attraction transpires when the cavity leakage rate strongly dominates the dynamics, i.e., the magnon-photon couplings as well as the magnonic damping rates are much weaker than the cavity relaxation rate. In the same parameter regime, on examining the spectral properties of the hybrid system, we unveil a narrow transmission window, with the possibility of transparent behavior in the limit of negligible magnon dissipation. Both these features, i.e., the inception of level crossing and the appearance of transparency, are borne out by a purely dissipative form of interaction that ensues between the magnons when the cavity field is adiabatically eliminated. In

fact, the adiabatic limit reproduces the characteristic dynamics of two spatially separated systems coupled through an interceding reservoir, thereby unveiling an equivalence with waveguide QED. It should be noted that qubits get coherently coupled with each other in a dispersive cavity [195]. In a cavity-magnonic setup, such a coupling has been experimentally realized in the dispersive limit, demonstrating level repulsion between the magnons [187]. In contrast, the level repulsion discussed in our paper makes no reference to the dispersive regime, and the magnons could well be on resonance with cavity mode.

This chapter is organized as follows. In section 8.1, we spell out the theoretical model describing a pair of magnetic systems coupled to a microwave cavity and highlight the two disparate regimes in which level splitting and level crossing could be observed. Following this, we study the induced magnetization in response to a cavity drive in section 8.2, to reaffirm the contrasting spectral signatures to both these behaviours. In section 8.3, we address the emergence of a dark polaritonic state and furnish the physical mechanism governing the excitation of this mode. Finally, in section 8.4, we illustrate the generation of a transmission window as a consequence of dissipative coupling between the two magnons. The results are summarized in section 8.5.

8.1 Level repulsion and attraction between magnons

Our model comprises a hybrid cavity-magnonic system, in which two macroscopic yttrium iron garnet (YIG) samples are placed inside a microwave cavity, as illustrated in Fig. 8.1. The YIG is a high-spin-density magnetic material, and the low lying excitations of the collective angular momentum of these spins in such magnetically ordered systems gives rise to quasi-particles, namely magnons. In our model, we consider a spatially uniform Kittel mode of either YIG as being dispersively coupled to the intracavity photons of a neighboring frequency. Therefore, in essence, the magnetization associated with the YIG sphere can simply be written as the magnetization of a ferromagnet with a single large spin $\mathbf{S}$, i.e., $\mathbf{M} = \gamma_e \mathbf{S}/V$, where $\gamma_e = e/m_e c$ is the gyromagnetic ratio for electron spin and $\mathbf{S}$ denotes the collective spin operator, and V the volume of the YIG sphere. The Hamiltonian of the hybrid magnon-cavity system as discussed in Chapter 2 is then

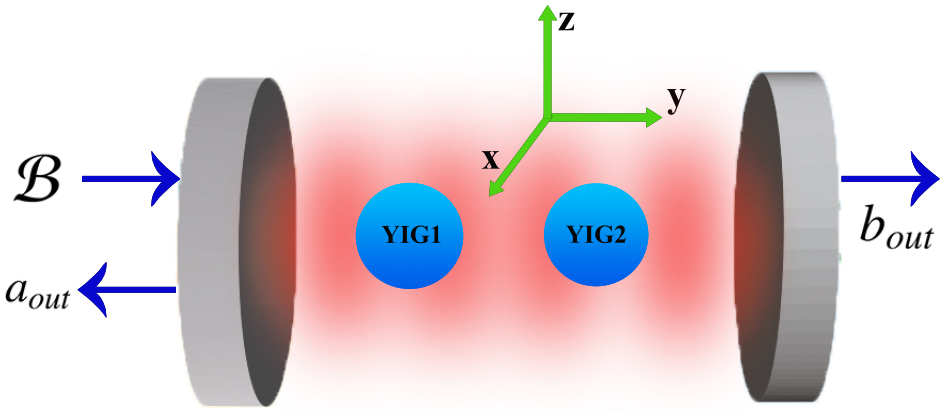

Figure 8.1: Schematic of two YIGs coherently coupled to a single-mode microwave cavity. The static magnetic fields exciting the Kittel mode in both the YIGs are aligned along the z-axis. The intracavity field mode is propagating along the y-axis, with the corresponding magnetic field directed along the x-axis.

provided by

$$H/\hbar = -\gamma_e \sum_{i=1}^{2} B_{0,i} S_{i,z} + \omega_a a^\dagger a - \gamma_e \sum_{i=1}^{2} S_{i,x} B_{i,x}, \tag{8.1}$$

where $\mathbf{B}_{0,i}$'s are the applied bias magnetic fields along the z direction, $S_{i,x}$ ($S_{i,z}$) denotes the x- (z-) component of the collective spin $\mathbf{S}$ of the i^{th} YIG, ω_a is the cavity resonance frequency, and a ($a^\dagger$) represents the annihilation (creation) operator of the cavity field. The magnetic field of the cavity field ($B_{n,x}$) is assumed to be along the x direction. A typical YIG sample having diameter $d = 1$ mm and an approximate spin density $\rho = 4.22 \times 10^{27}$ m^{-3} leads to the total number of spins $N \approx 10^{18}$. In the limit of a high spin density, we invoke the Holstein-Primakoff transformation to recast the raising and lowering operators as $S_i^+ = \sqrt{2S_i} m_i$, $S_i^- = \sqrt{2S_i} m_i^\dagger$, with $i = 1, 2$ labeling the two YIGs) and m_i ($m_i^\dagger$) operators satisfying the Bosonic algebra. With such simplifications, we can now tailor the Hamiltonian in Eq. (8.1) into its corresponding operator representation as

$$H/\hbar = \omega_a a^\dagger a + \sum_{i=1}^{2} \left[\omega_i m_i^\dagger m_i + g_i (m_i^\dagger a + m_i a^\dagger) \right] \tag{8.2}$$

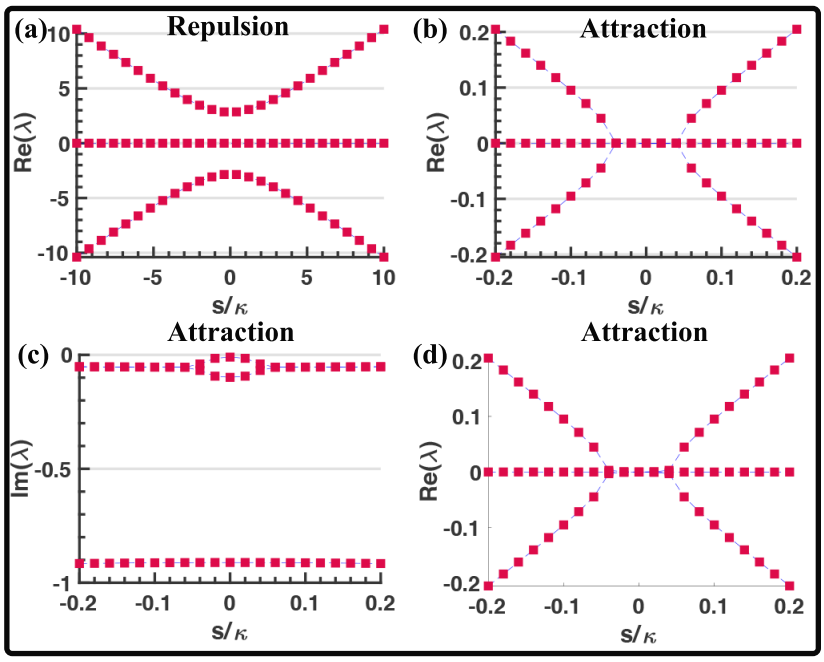

Figure 8.2: Level anticrossing and level crossing in two different regimes of cavity QED; (a) Eigenfrequencies of the cavity-magnon system for $g = 2$ and $\gamma_i = 1$ exhibiting level splitting; (b) Eigenfrequencies and (c) Linewidths in the case of $g = 0.2$ and $\gamma_i = 0.01$, with the features of level crossing; (d) Eigenfrequencies in the case of asymmetric decay rates $\gamma_1 = 0.01$, $\gamma_2 = 0.012$ and $g = 0.2$ demonstrating level attraction. All the parameters are chosen in units of κ.

where the frequency of Kittel mode $\omega_i = \gamma_e B_{0,i}$ with $\gamma_e/2\pi = 28$ GHz/T. The parameter $g_i = \frac{\sqrt{5}}{2}\gamma_e \sqrt{N} B_{\text{vac}}$ quantifies the coherent magnon-cavity coupling, with $B_{\text{vac}} = \sqrt{2\pi\hbar\omega_c/\text{V}}$ denoting the magnetic field of vacuum.

In the frame rotating at frequency ω_a, the Heisenberg equations of motion can be cast in the form $\dot{X} = -i\mathscr{H}X$, where $X^T = [\langle a\rangle \quad \langle m_1\rangle \quad \langle m_2\rangle]$, and the effective non-Hermitian Hamiltonian describing the system dynamics is provided by

$$\mathscr{H} = \begin{pmatrix} -i\kappa & g_1 & g_2 \\ g_1 & s - i\gamma_1 & 0 \\ g_2 & 0 & -s - i\gamma_2 \end{pmatrix}. \tag{8.3}$$

Here, we have set $\omega_a = (\omega_{m_1} + \omega_{m_2})/2$ (thus, the magnons are antisymmetrically detuned relative to the cavity frequency) and defined $s = (\omega_{m_1} - \omega_{m_2})/2$. The parameters κ and γ_i denote the rates

of dissipation appearing in the master equation. In what follows, we suppress the notation $\langle . \rangle$ in the mode amplitudes, as we are interested in a semiclassical description of the system. The three complex eigenvalues of $\mathscr{H}$, resulting from the characteristic polynomial equation

$$(\lambda + i\kappa)(\lambda + s + i\gamma_1)(\lambda - s + i\gamma_2) - g_1^2(\lambda + s + i\gamma_2) \\ -g_2^2(\lambda - s + i\gamma_1) = 0, \tag{8.4}$$

identify the normal modes of the hybridized system, also referred to as the polaritons. Here, we present two distinct parametric regimes: (i) where $g \gg \kappa, \gamma_i$ with the features of level repulsion and (ii), the weak coupling regime $g, \gamma_i \ll \kappa$ where the eigenvalues relevant to the system demonstrate level attraction. We demonstrate in Fig. 8.2, the solutions of the characteristic equation (8.4) in the two aforementioned parameter regimes where level repulsion and level attraction come to light. Specifically, in case (ii), when the cavity is weakly coupled to the magnon modes and the photons decay over a much shorter time scale than the magnons, we can observe signatures of level crossing between the magnon-like polaritons. The contrasting features in Fig. 8.2(a, b) can be analytically understood by inspecting the normal modes in these special regimes, as spelled out below.

For $\kappa = \gamma_1 = \gamma_2$ and $g_1 = g_2 = g$, the three eigenvalues of $\mathscr{H}$ are given by $\lambda_0 = -i\kappa$, $\lambda_\pm = -i\kappa \pm \sqrt{s^2 + 2g^2}$. The imaginary parts of the eigenvalues, which quantify the corresponding linewidths, are all identical and insensitive to the variations in s. The real parts of these eigenvalues are plotted against s in Fig. 8.2(a), where the minimum frequency gap between λ_+ and λ_-, equaling $2\sqrt{2}g$, is a manifestation of level repulsion in the system. Note that the minimum separation must be larger than the linewidth κ to observe level repulsion. However, in the limit $\kappa \gg \gamma_i$ and $\kappa \gg g_i$, level crossing is introduced over a small band of frequency detunings s, as portrayed in Fig. 8.2(b, c). We have assumed that $\gamma_1 = \gamma_2 = \gamma$ and $g_1 = g_2 = g$. It is, therefore, imperative to design a cavity with low quality factor to observe this effect. Neglecting the effect of γ, which is weak in

reference to κ, leads to the characteristic equation

$$(\lambda + i\kappa)(\lambda^2 - s^2) - 2g^2\lambda = 0. \tag{8.5}$$

Since the eigenvalues in the absence of g equal $\lambda_0 = -i\kappa$, and $\lambda_\pm = \pm s$, it can be argued that the perturbative correction to each of them for sufficiently small g would go as $\mathcal{O}(g^2)$. This consideration pins down the approximate form of λ_0 to be $-i\kappa[1 - 2g^2/(s^2 + \kappa^2)]$. Next, in view of the fact that both s and g^2 are small compared to κ, we approximate $\lambda_\pm + i\kappa \approx i\kappa$, which permits the reduction of the cubic equation into a quadratic one $\lambda_\pm^2 + 2\Gamma\lambda_\pm i - s^2 \approx 0$, where $\Gamma = g^2/\kappa$. This yields the remaining eigenvalues

$$\lambda_\pm = -i\Gamma \pm i\sqrt{\Gamma^2 - s^2}. \tag{8.6}$$

The forms of $\lambda_\pm$ make apparent the level crossing between them, with EPs located at $s = \Gamma$. The plots in Fig. 8.2(b, c) are found to be in remarkable agreement with the expressions obtained above where we have used identical decay rates for the magnon samples and they couple to the cavity field with equal strength. In Fig. 8.2(d), we have plotted the eigenfrequencies of the cavity-magnon system for asymmetric decay rates of the magnon samples where $\gamma_2 - \gamma_1 = 0.2\gamma_1$. We observe that the features of level attraction persist, thereby exhibiting robustness against small deviations around the symmetrical choice of system parameters.

In the following section, we extract spectroscopic information about the system of magnons coupled to a cavity by applying an external probe, which renders an empirical tool to observe level crossing and level anticrossing [196].

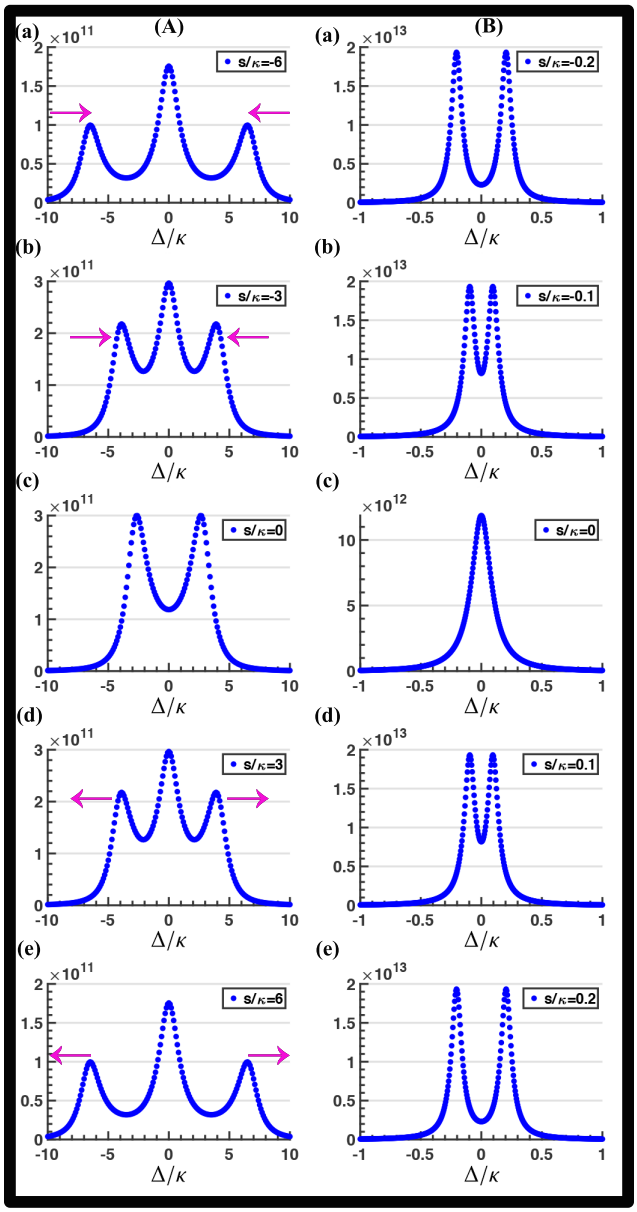

Figure 8.3: (Panel A; a-e) Sumtotal of the spincurrent response $|m_1|^2 + |m_2|^2$ plotted as functions of Δ_a in the case of strong magnon-photon coupling $g = 2$ and equal relaxation rates $\gamma_i = 1$ (similar to Fig. 8.2(a)). Note the conspicuous extinction of the central resonance in (A; c). (Panel B; a-e) Profiles for the case of $g = 0.2$, $\gamma_i = 0.01$ (similar to Fig. 8.2(b,c)). Only two peaks appear in this scenario. Drive power $P = 1$ mW. Other parameters are given in the text.

8.2 Spin currents under the conditions of level attraction and repulsion

In the presence of an external electromagnetic field at frequency ω_d driving the cavity, the Hamiltonian in Eq. (8.2) is superseded by

$$\begin{aligned} H/\hbar = \omega_a a^\dagger a + \sum_{i=1}^{2} \left[\omega_i m_i^\dagger m_i + g_i (m_i^\dagger a + m_i a^\dagger)\right] \\ + i\sqrt{\kappa}\mathscr{B}[a^\dagger e^{-i\omega_d t} - a e^{i\omega_d t}] \end{aligned} \tag{8.7}$$

with $\mathscr{B} = \sqrt{\frac{P}{\hbar\omega_d}}$ being the strength of external drive and P the driving power.By switching to the rotating frame of the drive, we deduce the mean-field equations for the cavity-magnon dynamics to be

$$\dot{X} = -i(\mathscr{H} - \Delta)X + F, \tag{8.8}$$

where we have separated out the cavity detuning $\Delta = \omega_d - \omega_a$, and $F^T = \sqrt{\kappa}[\mathscr{B}\ 0\ 0]$. Recall that $\mathscr{H}$ was defined in Eq. (8.3). The solution to the steady state can, therefore, be expressed as

$$X(\Delta) = -i(\mathscr{H} - \Delta)^{-1} F, \tag{8.9}$$

With the poles of this expression being accorded by the eigenvalues of $\mathscr{H}$, key information regarding the polaritonic properties would be encoded in the empirically observable response, such as the steady-state spincurrents $|m_1|^2$ and $|m_2|^2$. The steady-state response functions are given by

$$m_j = -i\sqrt{\kappa}\mathscr{B}[(\mathscr{H} - \Delta)^{-1}]_{j1}, \tag{8.10}$$

where $j = 1$ or 2 labels the magnon. Substituting the expression for $\mathscr{H}$, we obtain,

$$m_1 = \frac{-i\sqrt{\kappa}\mathscr{B}g_1(s + \Delta + i\gamma_1)}{D},$$
$$m_2 = \frac{i\sqrt{\kappa}\mathscr{B}g_2(s - \Delta - i\gamma_1)}{D}, \tag{8.11}$$

where $D = \det(\mathscr{H} - \Delta)$ has the expression

$$D = (\Delta + i\kappa)(s - \Delta - i\gamma_1)(s + \Delta + i\gamma_2) + g_1^2(s + \Delta + i\gamma_2)$$
$$-g_2^2(s - \Delta - i\gamma_1).$$

We now provide a numerical solution to the spectral features by scanning the probe frequency, and assuming, for simplicity, $g_1 = g_2 = g$.

In Fig. 8.3, on either of the panels (A) and (B), we plot the sum of the spincurrents from the individual magnon modes, i.e., $|m_1|^2 + |m_2|^2$ as a function of Δ for five different values around $s = 0$. The left panel (A) refers to the barely strong-coupling regime, i.e., $g_i > \kappa, \gamma_i$, and $\kappa = \gamma_i$. The total spincurrent, for $s \neq 0$, exhibits three distinct peaks corresponding to the resonant frequencies of the system. The central peak at $\Delta = 0$ is flanked on either side by two symmetrical polaritonic peaks. The disappearance of the central peak at $s = 0$ is symbolic of a dark polariton. We however remark that the modality of driving is crucial to the detection of the dark mode. If instead of the cavity, we drive one of the magnons, this mode will show up in the response function. We note that dark polaritons have been extensively discussed in the context of molecules interacting with cavities [104]. The underlying physics of this dark mode would be discussed at length in the subsequent section. From the figures (a) to (e) in the panel (A), it is evident that the two magnon-like polaritons move closer as $s \to 0$, leaving a minimum frequency gap between the two levels at $s = 0$. Since the levels never intersect, it is referred to as mode anticrossing. However, this picture incurs a dramatic inversion as we transition into the domain of weaker couplings and higher relaxation rates of the cavity photons. Figure 8.3, panel (B), displays the sumtotal of the spincurrents as a function of Δ in the limit $\kappa \gg \gamma_i$ and $\kappa \gg g_i$, for five different values of s. In

this scenario, around $s = 0$, the magnon-like polaritons coalesce together into a single peak. Note that the cavity-like central resonance remains strongly quenched on account of its large linewidth. The onset of level crossing points to a hidden dissipative interaction between the magnon modes. In Appendix B, we establish parity with these numerical results by uncovering this dissipative magnon-magnon coupling through the adiabatic elimination of the cavity mode. The parameters used for the numerical results were taken from recent experiments [1, 76]. The cavity and magnon resonance frequencies, as well as the driving frequency ω_d fall in the microwave domain, and we have used frequencies ranging from 9 GHz to 10 GHz. The cavity damping rate $\kappa/2\pi$ is taken to be 10 MHz.

8.3 Excitation of dark polariton via symmetry-breaking

As evidenced by the numerical illustration in Fig. 8.1, panel (A), when the magnon-photon coupling is adequately strong, the tripartite cavity-magnon system is endowed with three distinct spectral peaks characterizing the polaritonic modes of the hybrid composite. The two peripheral peaks are pushed inward as s becomes smaller, settling for a minimum separation at resonance. This limiting behavior is marked simultaneously by the complete extinction of the central peak, laying bare a characteristic dark mode when the conditions conform to perfect symmetry, i.e., when all three modes have identical detunings, and the magnons are symmetrically coupled to the intracavity field. We can delineate a physical argument supporting this observation by simply inspecting the normal modes of the undamped system. In the rotating frame of the cavity field, the Hamiltonian is given by

$$H = g[a^{\dagger}(m_1 + m_2) + h.c]. \tag{8.12}$$

For this Hermitian system, the polaritonic modes turn out to be $A = \dfrac{m_1 - m_2}{\sqrt{2}}$, $B = \dfrac{1}{\sqrt{2}}\Big[a + \dfrac{m_1 + m_2}{\sqrt{2}}\Big]$, and $C = \dfrac{1}{\sqrt{2}}\Big[a - \dfrac{m_1 + m_2}{\sqrt{2}}\Big]$, corresponding respectively to the eigenfrequencies $\lambda_0 = 0$,

$\lambda_+ = \sqrt{2}g$, and $\lambda_- = -\sqrt{2}g$, which recasts the Hamiltonian into the form

$$H = \sqrt{2}g[B^\dagger B - C^\dagger C]. \tag{8.13}$$

Thus, B and C appear as two counteroscillating normal modes of the symmetric system, with the frequency-splitting determined by the coupling strength g. Note, however, the conspicuous absence of the mode A in Eq. (8.13). This mode, therefore, represents a dark polariton, whereas B and C identify the bright polaritons with detectable spectral signatures. This is what is manifested in Fig. 8.3 (A; c). The picture obviously changes if we begin to steer away from the symmetry, which are exemplified by the other subfigures in the same panel. For non-zero value of s, the Hamiltonian transforms into $s(m_1^\dagger m_1 - m_2^\dagger m_2) + g[a^\dagger(m_1 + m_2) + h.c]$. This can be expressed in the original polaritonic representation as

$$H = \sqrt{2}g[B^\dagger B - C^\dagger C] + \frac{s}{\sqrt{2}}(A^\dagger B + AB^\dagger) - \frac{s}{\sqrt{2}}(A^\dagger C + AC^\dagger). \tag{8.14}$$

The additional terms in the new Hamiltonian, originating from the frequency discord between the magnons, are clearly indicative of energy transitions from B and C to A and vice versa. These new channels for energy exchange foreshadow how a mismatch in the magnon detunings would be instrumental to the illumination of the non-radiative polariton. The stimulating effect of symmetry-breaking can be experimentally observed via the spectroscopic properties of the system when it is irradiated by a probe field. Note that the brightening of dark modes by the introduction of strong nonlinearities has been reported earlier using a full quantum mechanical treatment beyond the mean-field approximation [197]. However, we have showcased here the simplest method of illuminating the dark state which works even within the mean-field description.

To analytically clarify the polaritonic suppression at resonance, let us examine the spectral signature of a real dissipative system, underpinned by the Hamiltonian $\mathscr{H}$. In the event of symmetrical detunings ($s = 0$) and equal damping rates ($\kappa = \gamma_1 = \gamma_2$), the eigenvalues of $\mathscr{H}$ go as

$\lambda_0 = -i\kappa$, $\lambda_\pm = \pm\sqrt{2}g - i\kappa$. The common expression for the spincurrents then reduces to

$$m_j = \frac{i\sqrt{\kappa}g\mathscr{B}}{(\Delta + \sqrt{2}g + i\kappa)(\Delta - \sqrt{2}g + i\kappa)}, \tag{8.15}$$

for $j = 1, 2$. Clearly, the contribution from the pole at λ_0 remains suppressed when the modes are on resonance and the magnon-photon couplings are perfectly symmetrical. Given the equality of the two spincurrents, it is no coincidence that the normal mode $A = \dfrac{m_1 - m_2}{\sqrt{2}}$ remains unpopulated in the steady state. On the other hand, if a small asymmetry is introduced in the frequencies by letting s become non-zero, the eigenvalues get modified into $\lambda_0 = -i\kappa$ and $\lambda_\pm = \pm\sqrt{s^2 + 2g^2} - i\kappa$. In this case, the pole at λ_0 leaves a detectable signature as underscored by the corresponding spincurrents

$$\begin{aligned} m_1 &= \frac{i\sqrt{\kappa}g\mathscr{B}(\Delta + s + i\kappa)}{(\Delta + i\kappa)(\Delta + \sqrt{s^2 + 2g^2} + i\kappa)(\Delta - \sqrt{s^2 + 2g^2} + i\kappa)}, \\ m_2 &= \frac{i\sqrt{\kappa}g\mathscr{B}(\Delta - s + i\kappa)}{(\Delta + i\kappa)(\Delta + \sqrt{s^2 + 2g^2} + i\kappa)(\Delta - \sqrt{s^2 + 2g^2} + i\kappa)}, \end{aligned} \tag{8.16}$$

which also remain unequal insofar as $s \neq 0$. This explains the emergence of the central peak in Fig. 8.3 as a signature of population transfer to the mode A. The corresponding peak height is provided by the expression

$$|m_1|^2 + |m_2|^2 = \frac{2g^2\mathscr{B}^2(s^2 + \kappa^2)}{\kappa(s^2 + 2g^2 + \kappa^2)}. \tag{8.17}$$

Clearly, the height reduces to a minimum at $s = 0$.

8.4 Dissipative-coupling-induced transparency

Having explored some of the distinctive regimes of cavity QED, which uncovered the contrasting features of level splitting and level crossing, it is worthwhile to study the transmission characteristics of the cavity-magnon system. For this purpose, we restrict our analysis to the regime where $\kappa \gg \gamma_i$ and $\kappa \gg g_i$, and shed light on the possibility of effecting transparent behaviour. Note that this is precisely the parameter domain that elicits level attraction.

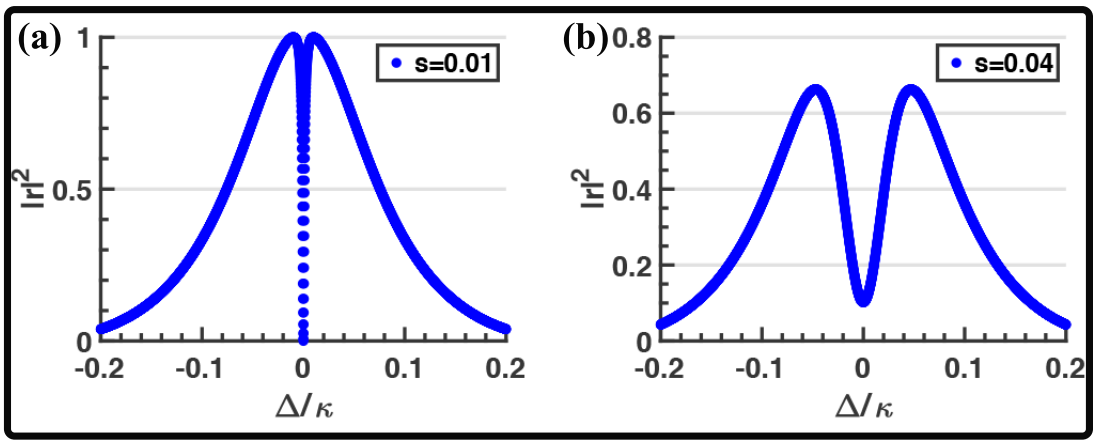

Figure 8.4: Reflection spectra for (a) $s = 0.01$ with $\gamma_i = 0$, and (b) $s = 0.04$ with $\gamma_i = 0.01$. Other parameters are $g = 0.2$ and $\kappa = 1$, which yields $\Gamma = g^2/\kappa = 0.04$.

For the cavity-driven system described by Eq. (8.7), we can obtain the reflected and transmitted output fields from the input-output formalism, with the relevant input-output relations being

$$\begin{aligned} b_{out} &= \sqrt{\kappa} a, \\ a_{out} + \mathscr{B} &= \sqrt{\kappa} a, \end{aligned} \tag{8.18}$$

where $a = -i\sqrt{\kappa}[(\mathscr{H} - \Delta)^{-1}]_{11}\mathscr{B}$ is the steady-state intracavity field obtained by setting $\dot{X} = 0$ in Eq. (8.8). Substituting this into the aforementioned relations, we extract the transmission and reflection coefficients to be

$$\begin{aligned} t &= \frac{i\kappa(\Delta - s + i\gamma)(\Delta + s + i\gamma)}{(\Delta + i\kappa)(\Delta - s + i\gamma)(\Delta + s + i\gamma) - 2g^2(\Delta + i\gamma)}, \\ r &= -1 + \frac{i\kappa(\Delta - s + i\gamma)(\Delta + s + i\gamma)}{(\Delta + i\kappa)(\Delta - s + i\gamma)(\Delta + s + i\gamma) - 2g^2(\Delta + i\gamma)}, \end{aligned} \tag{8.19}$$

At $\Delta = 0$, these expressions reduce to

$$\begin{aligned} t &= \frac{s^2 + \gamma^2}{s^2 + \gamma^2 + 2\gamma\Gamma}, \\ r &= -\frac{2\gamma\Gamma}{s^2 + \gamma^2 + 2\gamma\Gamma}, \end{aligned} \tag{8.20}$$

where $\Gamma = g^2/\kappa$. As long as $\gamma\Gamma \ll s^2$, the approximate behavior would be given by $t \approx 1 - \mathcal{O}(2\gamma\Gamma/s^2)$ and $r \approx \mathcal{O}(2\gamma\Gamma/s^2)$. In Figs. 8.4(a, b), we sketch the reflection profiles for a couple of values of s, vindicating the existence of a transmission window. As $\gamma/\kappa \to 0$, perfect transparency is observed at $\Delta = 0$. We note that this transparency effect is distinct from the well-known phenomenon of Electromagnetically Induced Transparency (EIT) [198, 199] in which two oscillators are coupled dispersively, i.e., through a Hermitian term in the Hamiltonian. In contrast, the transparency we report owes its origin to a dissipative form of magnon-magnon coupling surfacing in the limit of negligible magnon dissipation. The details on this origin are elaborated in Appendix B.

As s becomes smaller, in the limit $\gamma/\kappa \approx 0$, the EIT-like window gets progressively narrower leading to a sharpening of the central dip. This can be understood from the behavior of the eigenvalues derived earlier in Sec. II. Through pertinent approximations, we had obtained them to be $\lambda_0 = -i\kappa[1 - 2g^2/(s^2 + \kappa^2)]$ and $\lambda_\pm = -i\Gamma \pm i\sqrt{\Gamma^2 - s^2}$. While λ_0 had rather pedestrian features, the other two normal modes $\lambda_\pm \approx \lambda_\pm = -i\Gamma \pm i\sqrt{\Gamma^2 - s^2}$ were the source of level attraction. In the same vein, the unfolding of the sharp, precipitous dip in the reflection lineshapes can be traced down to the linewidths of the modes $\lambda_\pm$. Apropos of our parameter choices, when s/Γ is tiny compared to 1, as is the case in Fig. 8.4(a), they can be further approximated as

$$\begin{aligned} \lambda_+ &\approx -\frac{is^2}{2\Gamma}, \\ \lambda_- &\approx -2i\Gamma. \end{aligned} \tag{8.21}$$

While both of them have zero real parts, $\mathrm{Im}(\lambda_+)$ pales in comparison to $\mathrm{Im}(\lambda_-)$. In fact, the pole at λ_+ has a vanishingly small linewidth, which explains the sharp and narrow trough in the reflection spectrum. The effect of λ_-, on the other hand, is embodied in the Lorentzian envelope circumscribing both the peaks flanking the central minimum.

8.5 Summary

In conclusion, we have discussed the feasibility of engineering both level repulsion and level attraction between two magnons coupled to a single-mode cavity, by manipulating the relaxation rates and the magnon-photon coupling strengths. In the weak-coupling regime, when the cavity mode relaxes considerably faster than the magnon modes, an effective dissipative interaction is engendered between the two magnons, which is directly responsible for the unfolding of level attraction as well as a narrow transmission window. The level crossing is manifested as the coalescence of polaritonic peaks in the spincurrent response of the hybridized system. On the contrary, the strong-coupling regime, for comparable relaxation rates, results in distinguishable polaritonic peaks with the earmarks of level repulsion. Interestingly, when the magnons are tuned in resonance to the cavity together with symmetrical couplings, the spectral response is characterized by the appearance of a dark polaritonic state. The central dip designating the dark polariton transitions into a peak as we deviate from resonance, indicating the transfer of population into the dark mode. It could be noted that the bulk of the precursive literature on level attraction in cavity-magnonics was grounded in the study of magnon-photon coupling and the resulting polariton characteristics. On the other hand, the level attraction highlighted in our paper, is rooted in an effective magnon-magnon coupling infused via the photonic interaction with the individual magnon modes.

9. QUANTUM ENTANGLEMENT BETWEEN MACROSCOPIC FERRITE SAMPLES[1]

Quantum entanglement continues to attract considerable attention since it is a central resource for many quantum protocols and quantum information tasks. A question of prime importance is the existence of quantum effects at macroscopic scales. The earliest discussion started with the thought experiment of the Schrodinger's cat paradox. Since then, considerable progress has been made in the demonstration of possible quantum effects at macroscopic scales, especially by using atomic ensembles. For atomic ensembles, both long lived [200] and heralded entanglement [201–203] have been demonstrated. Given the success with atomic ensembles, several other systems have been studied- for example optomechanical systems have been used to demonstrate the entanglement between two mechanical mirrors. A recent work [204] reports heralded entanglement between two photonic crystal resonators containing mechanical elements; whereas Ockeloen-Korppi *et al* [205] report deterministic entanglement between two micromechanical drum oscillators in a superconducting resonator. In addition, entanglement between the cavity field and mechanical motion has been reported [206]. Given the overwhelming interest in entangling macroscopic systems, it is worthwhile to examine the possibility of a different class of systems, especially the ones involving magnetic excitations. We show that a ferrimagnetic system like YIG provides another platform to create and use quantum effects at macroscopic scale. The Kittel mode in YIG possesses unique properties including rich magnonic nonlinearities [37] and a low damping rate [22], and further, a high spin density in YIG allows strong coupling between magnons and microwave cavity photons, giving rise to quasiparticles, namely the cavity-magnon polaritons [21, 22, 97, 207]. Strong coupling between the YIG sphere and the cavity photons have been observed both at cryogenic and room temperatures [21]. Aided by these superior properties, YIG is reckoned to be the key ingredient in future quantum information networks [34], especially those with hybrid systems [174]. However, most of recent literature on the coupling of YIG spheres with the cavity field deal with

[1] A major part of this chapter is reproduced from *Deterministic quantum entanglement between macroscopic ferrite samples* by J. M. P. Nair and G. S. Agarwal, Appl. Phys. Lett. **117**, 084001 (2020), with the permission of AIP Publishing.

the observation of effects which belong to the semiclassical domain and can be explained in terms of the mean field description. These include the observation of bistability [1], cavity spintronics [29], level attraction for cavity magnon-polaritons [66], magnon dark modes, exceptional points, magnon induced transparency and magnetically controllable slow light. There are much fewer studies demonstrating the strictly quantum effects with YIG spheres. Cavity mediated interactions have been employed to demonstrate the coupling of a superconducting qubit to magnons and for the creation of a Fock state for the magnons. The earlier room temperature study of magnon-photon-phonon interactions [27] has been used to generate a tripartite entangled state [32] and squeezed states [31] in a hybrid magnon-photon-phonon system at mK temperatures i.e., under the condition $\hbar\omega_m/k_BT >> 1$. We note that previously phonon-phonon interactions and second order Raman scattering were used to produce phonon squeezing [208–212].

It is thus important to examine the possibility of quantum entanglement at macroscopic scale using two magnetic systems like YIG spheres. The YIG sphere consists of a macroscopic number of spins with value $s = 5/2$. Since the total number of spins in a sphere of size 250-μm is about $N \approx 3.5 \times 10^{16}$, the excitations in the sphere can be modelled in terms of an oscillator. Thus, the entanglement between two YIG spheres can be thought of as the entanglement between two macroscopic oscillators characterized by the bosonic operators m_1, m_2 ($m_1^\dagger$, $m_2^\dagger$). In order to produce entanglement between the two oscillators, we need an effective interaction of the type $(m_1^\dagger m_2^\dagger + c.c.)$, which usually comes from considerations of parametric [77] or Kerr nonlinearities [213]. However the interaction of the type $(m_1 m_2^\dagger + c.c.)$ is easy to produce, for example, by putting the YIG spheres in a high quality cavity where the exchange of cavity photon can strongly couple the two YIG spheres. The Kerr nonlinearities for the YIG spheres are very weak and require strong driving powers [1]. It is better if the weak nonlinearity of the YIG spheres is avoided, although these nonlinearities have been used to produce entanglement between two magnon modes in a magnon-cavity system [33, 91].

Here we present a scheme to generate an entangled pair of YIG spheres without using any nonlinearities, thus, overcoming the problem of weak nonlinearities and use of strong drives. We show

how driving fields with strictly quantum properties can produce remarkable macroscopic entanglement. As a byproduct of our work, we are able to generate the quantized states of the coupled system of two YIG spheres. Our calculations are based on the following physical picture: we place two YIG spheres in a high quality cavity and drive the cavity with a quantum field. Specifically, we choose the field produced by a flux-driven Josephson parametric amplifier (JPA) for the quantum field which generates the microwave field with strong squeezing properties. In addition, we work in the parameter domain wherein the squeezing of the quantum drive is transferred to the cavity. Since the cavity is strongly coupled to the two YIG spheres, the squeezed cavity field results in the bipartite entanglement of the two macroscopic magnetic samples. Based on experimentally available parameters, we show that significant bipartite entanglement can be generated between the YIG samples. We also demonstrate that the entanglement is robust against temperature. Our results can be extended to other sample sizes and other kind of modes of the ferrimagnetic spheres [97]. Further, the method that we propose is quite generic and can be used for other macroscopic systems.

This chapter is organized as follows. In section 9.1, we obtain the quantum Langevin equations describing the dynamics of the cavity-magnon system with quantum drive. Subsequently, in section 9.2, we calculate Logarithmic negativity as a measure of quantum entanglement revealing optimum conditions for the quantum correlations. In section 9.3, we provide two experimentally realizable tests for entanglement, corroborating our results in section 9.2. As a byproduct of our research, we observe squeezing in the collective magnon variables and explicate the details in section section 9.4. The chapter is summarized in section section 9.5.

9.1 Quantum Langevin equations of the system

We consider the cavity-magnon system [27, 32] which consists of cavity microwave photons and magnons, as shown in Fig. 9.1. The magnons are quasiparticles, a collective excitation of a large number of spins each with spin value $5/2$ in a YIG sphere. They are coupled to the cavity photons via the magnetic dipole interaction. The Hamiltonian of the system reads

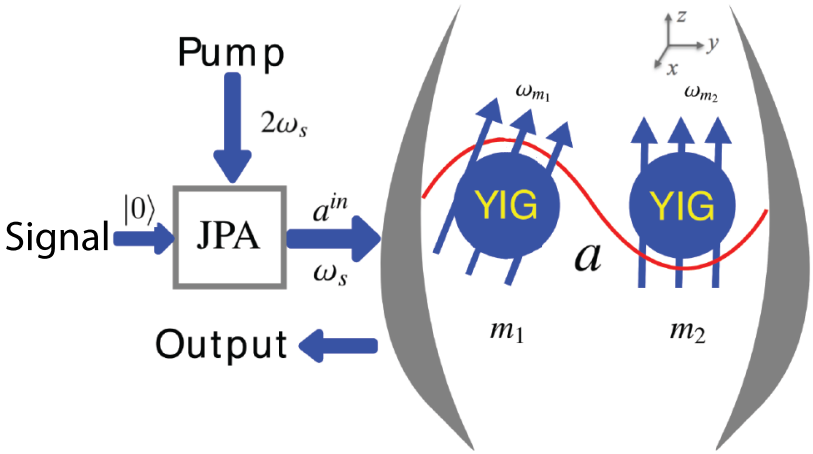

Figure 9.1: Two YIG spheres are placed inside a microwave cavity near the maximum magnetic field of the cavity mode, and simultaneously in a uniform bias magnetic field. The cavity is driven by a weak squeezed vacuum field generated by a flux-driven JPA. The magnetic field of the cavity mode is in the x direction and the bias magnetic field is applied along the z direction.

$$\mathscr{H}/\hbar = \omega_a a^\dagger a + \omega_{m_1} m_1^\dagger m_1 + \omega_{m_2} m_2^\dagger m_2$$
$$+g_{m_1 a}(a + a^\dagger)(m_1 + m_1^\dagger) + g_{m_2 a}(a + a^\dagger)(m_2 + m_2^\dagger), \tag{9.1}$$

where a ($a^\dagger$) are the annihilation (creation) operators of cavity mode, m_1, m_2 ($m_1^\dagger$, $m_2^\dagger$) are the annihilation (creation) operators of the two magnon modes, and they represent the collective motion of spins via the Holstein-Primakoff transformation in terms of Bosons. The parameters ω_a, ω_{m_i} (i=1,2) are the resonance frequencies of the cavity and the magnon modes. Hereafter, wherever we use a subscript 'i' it can take values from 1 to 2. The magnon frequency is given by the expression $\omega_{m_i} = \gamma H_i$, where $\gamma/2\pi = 28$ GHz/T is the gyromagnetic ratio and H_i are the external bias magnetic fields. The $g_{m_1 a} = g_{m_2 a} = \eta\sqrt{5\mu_0\hbar\omega N/V}\gamma/2$ in Eq. (9.1) are the linear photon-magnon coupling strengths where μ_0 is the permeability of vacuum and SI units are used throughout. Here, N is the net number of spins in the YIG sample which determine the total magnetic moment, V is the volume of the cavity and η describes the spatial overlap between the microwave field and magnon mode. We emphasize that our model Hamiltonian (9.1) has no nonlinearities. This is different from the entanglement in the context of optomechanical systems which are based on

the nonlinearity of the optomechanical interactions [205]. The cavity is driven by a weak squeezed vacuum field generated by a flux driven JPA. JPAs can, in principle, amplify a single signal quadrature without adding any extra noise. The squeezed vacuum is generated by degenerate parametric down-conversion using the nonlinear inductance of Josephson junctions [40–51], and a squeezing down to 10% of the vacuum variance has been produced. The operation of generating squeezed vacuum is depicted in Fig. 9.1. Vacuum fluctuations are at the signal port and the pump field is applied at frequency $2\omega_s$. The pump photon splits into a signal and an idler photon. Strong quantum correlations between the degenerate signal and idler photons are generated which result in squeezing. The output is at the frequency ω_s [43]. The mathematical procedure is standard and we give minimum of mathematical details so that we can focus on results. We use standard quantum Langevin formalism [214] to model the system and the equations describing the evolution of the system operators will contain the input drive terms. Applying the rotating-wave approximation, $g_{m_i a}(a + a^\dagger)(m_i + m_i^\dagger)$ becomes $g_{m_i a}(a m_i^\dagger + a^\dagger m_i)$ [21, 22, 27, 207]. In the rotating frame at the frequency ω_s of the squeezed vacuum field, the quantum Langevin equations (QLEs) describing the system can be written as follows

$$\begin{aligned}
\dot{a} &= -(i\Delta_a + k_a)a - ig_{m_1 a}m_1 - ig_{m_2 a}m_2 + \sqrt{2k_a}a^{in}, \\
\dot{m}_1 &= -(i\Delta_{m_1} + k_{m_1})m_1 - ig_{m_1 a}a + \sqrt{2k_{m_1}}m_1^{in}, \\
\dot{m}_2 &= -(i\Delta_{m_2} + k_{m_2})m_2 - ig_{m_2 a}a + \sqrt{2k_{m_2}}m_2^{in},
\end{aligned} \tag{9.2}$$

where $\Delta_a = \omega_a - \omega_s$, $\Delta_{m_i} = \omega_{m_i} - \omega_s$, k_a is the dissipation rate of the cavity, k_{m_i} are the dissipation rates of the magnon modes, and a^{in}, m_i^{in} are the input noise operators of the cavity and magnon modes, respectively. These input operators take into account the driving of the cavity by a quantum field. They are characterized by zero mean and the following correlation relations [215], $\langle a^{in}(t)a^{in\dagger}(t')\rangle = (\mathcal{N}+1)\delta(t-t')$, $\langle a^{in\dagger}(t)a^{in}(t')\rangle = \mathcal{N}\delta(t-t')$, $\langle a^{in}(t)a^{in}(t')\rangle = \mathcal{M}\delta(t-t')$, $\langle a^{in\dagger}(t)a^{in\dagger}(t')\rangle = \mathcal{M}^*\delta(t-t')$, where $\mathcal{N}=\sinh^2 r + N_a(\omega_a)(\sinh^2 r + \cosh^2 r)$, $\mathcal{M}=e^{i\theta}\sinh r \cosh r(1+2N_a(\omega_a))$, with r and θ being the squeezing parameter and the phase of the input squeezed vacuum

field, respectively. The thermal photon number $N_a(\omega_a) = [\exp(\frac{\hbar\omega_a}{k_BT}) - 1]^{-1}$. We assume that the coupling losses are inconsequential to avoid the degradation of squeezing properties of the input field. The parameter $\mathscr{M}$ is the most significant parameter for generating macroscopic entanglement. We assume that the bandwidth of the squeezed radiation is much bigger than k_a. The case of finite bandwidth requires non-markovian framework and is a subject of separate investigation. Without loss of generality, we set $\theta = 0$ for most of the discussion below. We have the other input correlations for the magnon as $\langle m_i^{in}(t) m_i^{in\dagger}(t')\rangle = [N_{m_i}(\omega_{m_i}) + 1]\delta(t - t')$, $\langle m_i^{in\dagger}(t) m_i^{in}(t')\rangle = N_{m_i}(\omega_{m_i})\delta(t - t')$, where $N_{m_i}(\omega_{m_i}) = [\exp(\frac{\hbar\omega_{m_i}}{k_BT}) - 1]^{-1}$.

9.2 Logarithmic negativity as a measure of quantum entanglement

We now show that the YIG spheres can be entangled by resonantly driving the cavity with a squeezed vacuum field. The quadratures of the cavity field and the two magnon modes are defined as $X = (a + a^\dagger)/\sqrt{2}$, $Y = i(a^\dagger - a)/\sqrt{2}$, $x_i = (m_i + m_i^\dagger)/\sqrt{2}$ and $y_i = i(m_i^\dagger - m_i)\sqrt{2}$, and similarly for the input noise operators. The QLEs describing the quadrature fluctuations $(X, Y, x_1, y_1, x_2, y_2)$ can be written as

$$\dot{u}(t) = Au(t) + n(t), \tag{9.3}$$

where $u(t) = [X(t), Y(t), x_1(t), y_1(t), x_2(t), y_2(t)]^T$, $n(t) = [\sqrt{2k_a}X^{in}, \sqrt{2k_a}Y^{in}, \sqrt{2k_{m_1}}x_1^{in}, \sqrt{2k_{m_1}}y_1^{in}, \sqrt{2k_{m_2}}x_2^{in}, \sqrt{2k_{m_2}}y_2^{in}]^T$ and

$$A = \begin{bmatrix} -k_a & \Delta_a & 0 & g_{m_1a} & 0 & g_{m_2a} \\ -\Delta_a & -k_a & -g_{m_1a} & 0 & -g_{m_2a} & 0 \\ 0 & g_{m_1a} & -k_{m_1} & \Delta_{m_1} & 0 & 0 \\ -g_{m_1a} & 0 & -\Delta_{m_1} & -k_{m_1} & 0 & 0 \\ 0 & g_{m_2a} & 0 & 0 & -k_{m_2} & \Delta_{m_2} \\ -g_{m_2a} & 0 & 0 & 0 & -\Delta_{m_2} & -k_{m_2} \end{bmatrix}.$$

The system is a continuous variable (CV) three- mode Gaussian state, and it can be completely described by a 6×6 covariance matrix (CM) V defined as $V_{ij}(t) = \frac{1}{2}\langle u_i(t)u_j(t) + u_j(t)u_i(t)\rangle$, $(i, j = 1,$

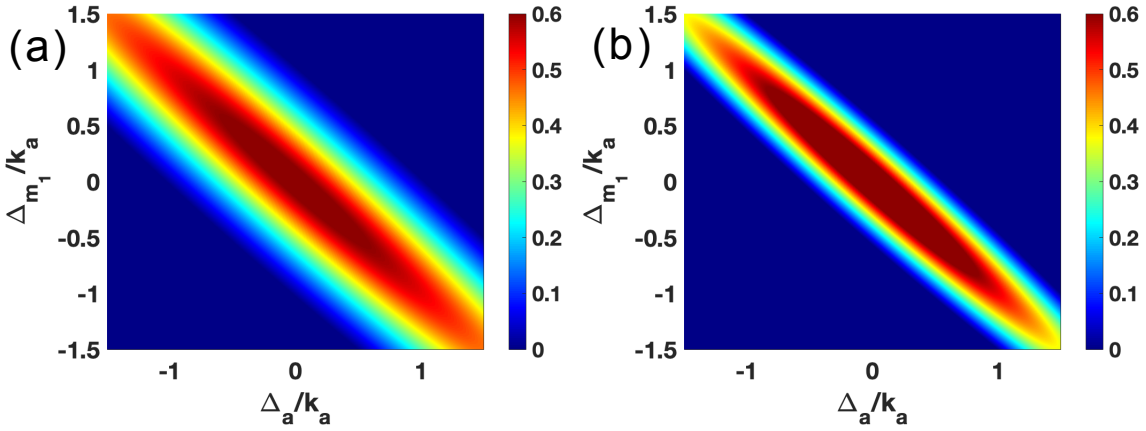

Figure 9.2: Density plot of bipartite entanglement $E_{m_1m_2}$ between the two magnon modes versus Δ_a and Δ_{m_1} (a) with $\Delta_{m_2} = \Delta_{m_1}$, $r = 1$, $T = 20$ mK, (b) with $\Delta_{m_2} = \Delta_{m_1}$, $r = 1.5$, $T = 20$ mK. Other parameters are given in the text.

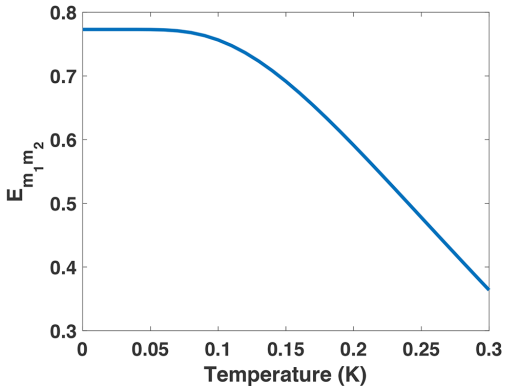

Figure 9.3: Plot of bipartite entanglement $E_{m_1m_2}$ between the two magnon modes against temperature with $\Delta_a = \Delta_{m_1} = \Delta_{m_2} = 0$ and $r = 1.5$.

2....6) which has symmetrized product of operators as the quadratures do not necessarily commute. The steady state CM V can be obtained by solving the Lyapunov equation [216]

$$AV + VA^T = -D, \tag{9.4}$$

where D is the diffusion matrix defined as $\langle n_i(t)n_j(t') + n_j(t')n_i(t)\rangle/2 = D_{ij}\delta(t - t')$. Once we obtain the six dimensional covariance matrix V, we find the covariance matrix $\widetilde{V}$ between the

two magnon modes by writing $\widetilde{V} = V_{ij}$ where i, j runs from 3 to 6. We use logarithmic negativity [217, 218] as the quantitative measure to investigate the bipartite entanglement $E_{m_1m_2}$ between the two magnon modes. It can be obtained from $E_{m_1m_2} = max[0, -ln(2\nu_-)]$ where $\nu_- = min[eigenvalue(i\Omega P_{12}\widetilde{V}P_{12})]$, $\Omega = i\sigma_y \bigoplus i\sigma_y$, $P_{12} = 1 \bigoplus \sigma_z$ and σ_y, σ_z are the Pauli matrices [219]. The symbol $\bigoplus$ means the direct sum of operators on either side of the symbol. Figure 9.2(a)-(b) shows the bipartite entanglement between the two magnon modes at two different squeezing parameters. We use a set of experimentally feasible parameters [27]: $k_a/2\pi = 5k_{m_i}/2\pi =$ 5 MHz, and $T = 20$ mK, $N_{m_1} = N_{m_2} \approx 0$ at 20 mK. The YIG sphere has a diameter 250-μm and the number of spins $N \approx 3.5 \times 10^{16}$. For a cavity of dimensions $22 \times 18 \times 3$ mm and resonance frequency $\omega_a/2\pi = 10$ GHz [21], the coupling constant g_{m_ia} given in section 2 becomes 40 MHz with a spacial overlap of 1. Therefore, we take $g_{m_ia} = 4k_a$, a reasonable estimate for the coupling constants. We have adopted the parameters so that the two magnon modes are identical. We observe that $\Delta_a = \Delta_{m_1} = \Delta_{m_2} = 0$, in other words $\omega_a = \omega_s$, $\omega_{m_i} = \omega_s$ are optimal for the entanglement between the two YIG samples. At resonance we observe the maximum amount of entanglement and it increases with the increase in the squeezing parameter. Figure 9.3 shows that the bipartite entanglement is quite robust against temperature. We observe significant amount of entanglement even at T =0.3 K which turns out to be better than the schemes based on nonlinearities [33, 91]. We have chosen identical coupling between photon and the two magnon modes. In the case of unequal coupling the entanglement goes down. Although we have chosen two identical YIG spheres, one can have two cuboidal YIG samples, as in [29], with an angle θ between the external magnetic field and the local microwave magnetic field at one YIG sample. This makes the resonance frequencies of the two samples different. Figure 9.4 displays the bipartite entanglement between the magnon modes with unequal resonance frequencies. We observe that small difference of the order of k_a in resonance frequencies does not produce significant change in the amount of entanglement generated.

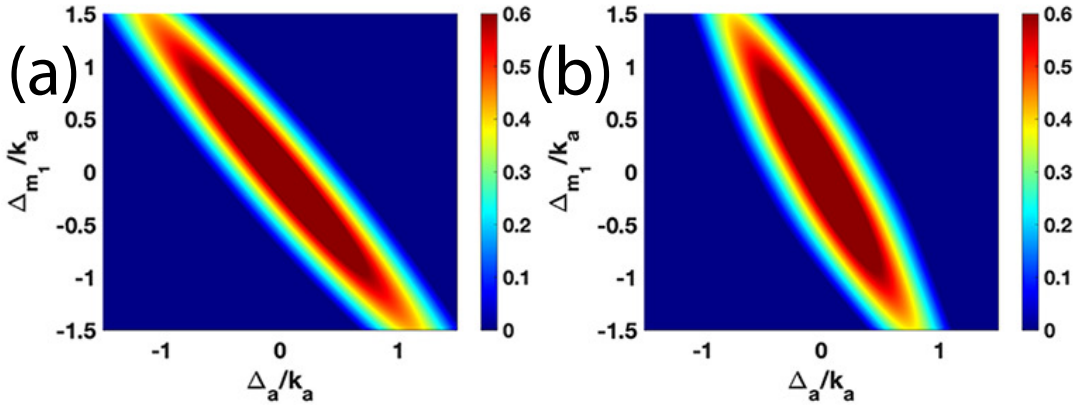

Figure 9.4: Density plot of bipartite entanglement $E_{m_1m_2}$ between the two magnon modes versus Δ_a and Δ_{m_1} (a) with $\Delta_{m_2} = \Delta_{m_1}/2$, $r = 1.5$, $T = 20$ mK. (b) with $\Delta_{m_2} = 0$, $r = 1.5$, $T = 20$ mK.

9.3 Experimentally realizable tests for entanglement

Next we discuss two different criteria for entanglement in a two mode CV system. The advantage of these criteria over logarithmic negativity is that the former can be easily examined through experiments [204, 205], though in a qualitative way. The first inseparability condition proposed by Simon [219] and Duan *et al.* [220] is the sufficient condition for entanglement in a two-mode CV system. We define a set of operators $M = (m_1 + m_2)/\sqrt{2}$, $m = (m_1 - m_2)/\sqrt{2}$. The criterion suggests that if the two modes are separable then they should satisfy the following inequality

$$\langle M_x^2 \rangle + \langle m_y^2 \rangle \geq 1, \tag{9.5}$$

where M_x and m_y are defined as $M_x = (M + M^\dagger)/\sqrt{2}$, $m_y = i(m^\dagger - m)/\sqrt{2}$. In other words, violation of the inequality in Eq. (9.5) means the existance of entanglement between the two YIG samples. Figure 9.5(a) shows that there is region around $\Delta_a = 0$ and $\Delta_{m_1} = 0$ (resonance) in which $\langle M_x^2 \rangle + \langle m_y^2 \rangle$ is less than one and it is a clear manifestation of the entanglement present between the YIG samples.

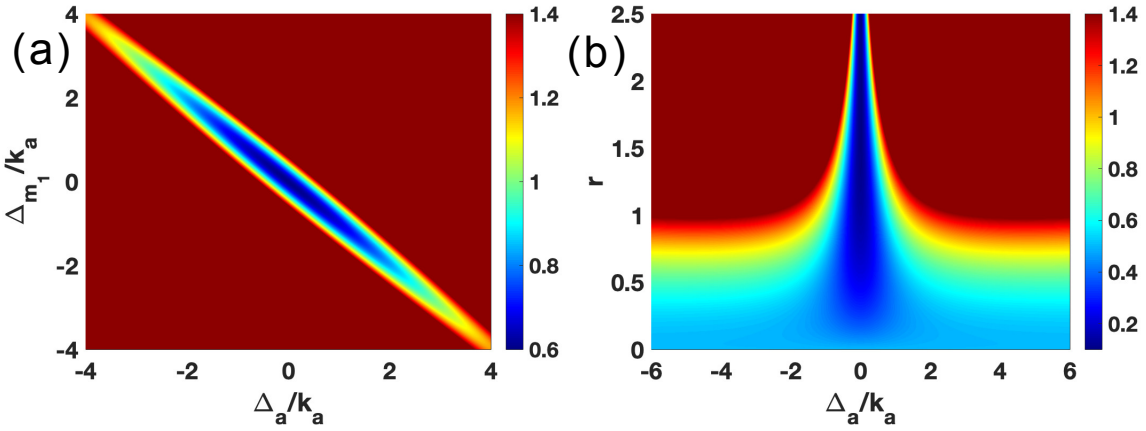

Figure 9.5: (a) $\langle M_x^2 \rangle + \langle m_y^2 \rangle$ against Δ_a and Δ_{m_1} with $\Delta_{m_2} = \Delta_{m_1}$, $r = 1.5$, $T = 20$ mK. (b) $\langle M_x^2 \rangle$ against Δ_a and squeezing parameter r with $\Delta_{m_1} = \Delta_{m_2} = 0$, T=20 mK.

We next present a test of entanglement based on the inequality of Mancini *et al* [221]

$$\langle M_x^2 \rangle \langle m_y^2 \rangle \geq 1/4, \tag{9.6}$$

with the violation of Eq. (9.6) implying that the YIG samples are entangled. We use identical coupling strengths between the cavity and the two YIG samples. Therefore, when $\Delta_{m_1} = \Delta_{m_2} = 0$ the Hamiltonian of the system in the rotating frame of the drive can be written as

$$\mathscr{H}/\hbar \;\; = \Delta_a a^\dagger a + \sqrt{2} g_{m_1 a}(a + a^\dagger)(M + M^\dagger). \tag{9.7}$$

The Hamiltonian does not contain a term involving m and $m^\dagger$. Hence the fluctuations in m will be equal to the fluctuations at time $t = 0$. Since m at $t = 0$ is in the vacuum state (at low temperature 20 mK), we have $\langle m_y^2 \rangle = 1/2$. Figure 9.5(b) shows that there is a region close to resonance where the quantity $\langle M_x^2 \rangle$ is less than $1/2$. This violates the inequality in equation (9.6) and hence the two YIG samples are entangled. This further corroborates our results. Thus the generated quantum entanglement can be monitored by examining the fluctuations in the collective variable M which would radiate a field at the microwave frequency ω_s. The quantum features like squeezing

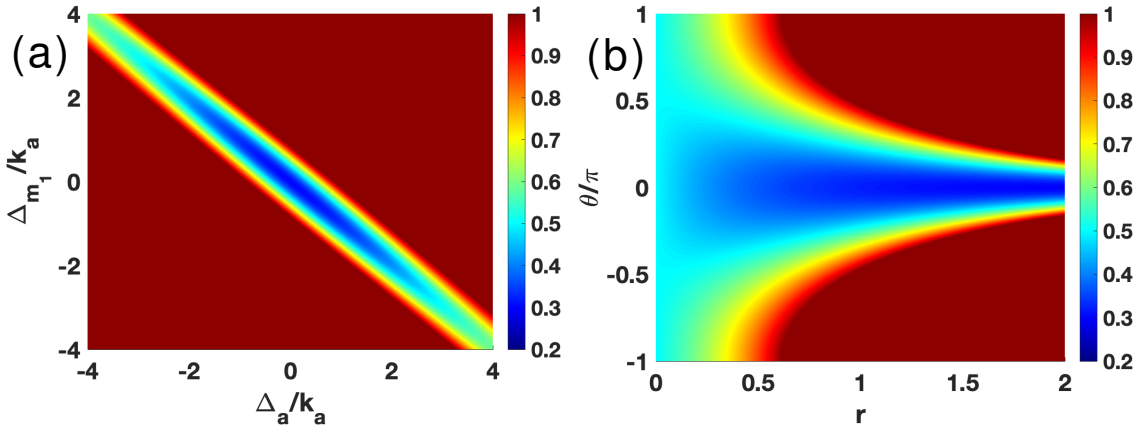

Figure 9.6: (a) Variance of the first magnon quadrature $\langle x_1(t)^2\rangle$ versus Δ_a and Δ_{m_1}. (b) Variance of the first magnon quadrature against squeezing parameter r and phase θ. The other parameters in (a) are $r = 1.5$, $\Delta_{m_1} = \Delta_{m_2}$, T =20 mK. Other parameters in (b) are $\Delta_a = \Delta_{m_1} = \Delta_{m_2} = 0$ and T =20 mK. $\langle x_2(t)^2\rangle$ is identical to $\langle x_1(t)^2\rangle$.

can, in principle be detected by using methods based on mixing the radiated field with a local oscillator [222]. These quantum features can be traced back to the entanglement of the spheres as demonstrated by the discussion based on the inequalities (9.5) and (9.6).

9.4 Squeezed magnon states

As a byproduct of our results we investigate the squeezing of the two magnon modes and show that it can be acheived by resonantly driving the cavity with a squeezed vacuum field. We note that the previous work [31] examined the squeezing of magnons in a single YIG sphere, whereas, here we consider two YIG spheres in the cavity. We are interested in the variances of the cavity and magnon mode quadratures and they are given by diagonal elements of the time-dependent CM $V(t)$ as defined previously. As discussed in [31], when the cavity and the two magnon modes are decoupled, the cavity field is squeezed as a result of the squeezed driving field and the magnon modes possesses vacuum fluctuations. As we increase the coupling strength, squeezing is partially transffered to the two identical YIG samples. The blue region in Fig. 9.6(a)-(b) represents the region of squeezing. We observed a squeezing of about 2.17 dB for each of the two magnon modes at resonance with T =20 mK. Note that Fig. 9.5 give the magnon quadrature when both the YIG

samples are present. At resonance we also find a squeezing of about 6.72 dB for the M_x quadrature of the collective variable M. This is comparable to the results when one had only one YIG sample present.

9.5 Summary

To summarize, we have presented a scheme to generate an entangled pair of YIG samples in a cavity-magnon system. Entanglement of magnon modes can be generated through resonantly driving the cavity by a squeezed vacuum field and it can be realized using experimentally attainable parameters. The entanglement produced is robust against temperature. Our scheme for entangling YIG samples does not require any nonlinearities and hence goes against the conventional wisdom of producing entanglement. This provides a different method for entangling macroscopic systems, which can be used in other macroscopic systems as well.

10. SUMMARY AND OUTLOOK

In summary, we investigated some of the semiclassical and quantum phenomena ensuing from waveguide and cavity-integrated magnonic systems involving ferromagnetic Yttrium iron garnets. They have attracted enormous interest of late as a new platform to observe quantum effects at the macroscopic scales. More specifically, we studied the ramifications of anti-$\hat{PT}$ symmetry in dissipatively coupled two-mode anharmonic systems, demonstrating, for example, the generation of a BIC, which can be exploited for sensing perturbations, especially those of anharmonic nature. IN the context of coherently coupled cavity-magnonic systems, Bai *et al.* reported an experiment on the cavity-mediated transfer of spin current between two ferrite samples implemented in the linear domain [29]. However, these magnetic systems are intrinsically anharmonic. Inspired by this, we developed a theory for the spin current [38] in the nonlinear domain via the incorporation of a strong external drive, wherein the Kerr anharmonicities of the ferrites were also factored in. This leads to the emergence of nonlinear cavity-magnon polaritons and we could observe both bistable and multistable characteristics of the spin current. Further, we developed a model for the spectroscopic detection of nonlinear spin currents, revealing some of the key properties of the nonlinear polaritons. The transmission of a weak probe field was used to obtain quantitative information on the multistable behaviour of the spin current. Recently, our results were confirmed by experimental data [223]. Recently, in the domain of weak external pumping, we explicated how the application of a two-photon parametric drive could result in a strong amplification in the energy transfer between two magnetic samples interacting via a cavity [52]. The spectacular amplification of spin-current transfer at the resonance condition stems from a parametrically produced long-lived mode in the system.

In the course of investigating different quantum optical platforms, we got interested in waveguide integrated systems where experimental interest has flourished in the recent past. We proposed a new scheme in the context of dissipatively coupled anti-$\hat{PT}$ symmetric systems for the sensing of weak anharmonic perturbations [80]. We considered the case of two Bosonic modes interact-

ing via a common reservoir, which can introduce a non-Hermitian form of coupling between the interacting subsystems. The linear response of the system becomes highly sensitive to nonlinear perturbations in the system, which owes its origin to an especially long-lived eigenmode. We demonstrated the remarkable sensing capabilities of this scheme in a system involving a weakly anharmonic YIG sample interacting with a cavity via a tapered fiber waveguide. As a natural continuation of this work, we subsequently investigated the properties of strongly driven dissipatively coupled nonlinear systems [81]. We theoretically illustrated the remote transfer of bistability between two systems interacting via a waveguide and revealed the significantly lower threshold for bistability in such systems when compared to their coherently coupled counterparts. It was found, in fact, that the dissipatively coupled systems offered a nearly five-fold advantage over the latter. Further, we spectroscopically investigated the hysteresis by applying a probe through the waveguide, and the shift in polariton peaks of the transmission replicated the nonlinear response, while also uncovering a region of anomalous transmission analogous to the Mollow gain effect. A recent experiment by Dr. Hu's group at the University of Manitoba confirmed our theoretical predictions [224].

Extending our work on coherently coupled systems, we illustrated two disparate parameter domains in the magnon-magnon interaction mediated by a cavity and foregrounds the possibility of both level attraction and repulsion [83]. Aside from that, for antisymmetric detunings to the magnon modes, a transmission window was found to emerge, exhibiting transparency in the limit of negligible magnon dissipation rates. In addition, we provided a new scheme to entangle two YIGs placed inside a microwave cavity, without using intrinsic nonlinearities in the system. The cavity is driven externally by a flux-driven Josephson parametric amplifier (JPA) which produces a microwave field with strong squeezing properties. We used logarithmic negativity as a measure of entanglement while also investigating various testable inequalities for continuous variable (CV) entanglement which are easily accessible in the experiments. For experimentally attainable parameters of the system, we demonstrated strong CV entanglement between magnetic samples that can survive even at 300 mK. Prior to this research, we had noticed

Although demonstrated in the context of magnonic systems, our results are generic, and applicable to a large class of systems, for example, atomic ensembles, quantum dots, superconducting qubits and many more. It is also worth noting that anti-$\hat{PT}$ symmetric systems with dissipative coupling are the most naturally occurring when compared with their $\hat{PT}$ symmetric counterparts, where the latter require the incorporation of gain. The physics of such systems, in particular, those involving condensed matter architectures have opened up a new avenue in the study of collective quantum phenomena. In the future, we would like to extend our analysis of dissipatively coupled systems to multi-dimensions and their topological properties.

In the future, we would like to extend our research into topological insulators and topological effects in non-Hermitian systems. The lion's share of already existing research on non-Hermitian systems involves lattices with coherently coupled subsystems. Some of the interesting topics to explore include a one-dimensional SSH model with an array of dissipatively coupled Bosonic modes. The system, under anti-$\hat{PT}$ symmetry, may lead to full and partial topological phases, and we could possibly illustrate its rich topology in an experimentally realizable system, for instance, an array of split ring resonators. The resonators can be coupled dissipatively via a mediating cavity in the dissipative domain. Further, a circuit model may be used to enunciate the physical origin of the topology and we could advance a protocol for the experimental observation of winding numbers. In addition, we would also like to develop an exact theoretical model for the nonlinear modifications to SSH models.

REFERENCES

[1] Yi-Pu Wang, Guo-Qiang Zhang, Dengke Zhang, Tie-Fu Li, C.-M. Hu, and J. Q. You. Bistability of cavity magnon polaritons. *Phys. Rev. Lett.*, 120:057202, Jan 2018.

[2] Charles H Bennett and David P DiVincenzo. Quantum information and computation. *nature*, 404(6775):247–255, 2000.

[3] H Jeff Kimble. The quantum internet. *Nature*, 453(7198):1023–1030, 2008.

[4] Margareta Wallquist, Klemens Hammerer, Peter Rabl, Mikhail Lukin, and Peter Zoller. Hybrid quantum devices and quantum engineering. *Physica Scripta*, 2009(T137):014001, 2009.

[5] JQ You and Franco Nori. Atomic physics and quantum optics using superconducting circuits. *Nature*, 474(7353):589–597, 2011.

[6] R. Hanson, L. P. Kouwenhoven, J. R. Petta, S. Tarucha, and L. M. K. Vandersypen. Spins in few-electron quantum dots. *Rev. Mod. Phys.*, 79:1217–1265, Oct 2007.

[7] Ze-Liang Xiang, Sahel Ashhab, JQ You, and Franco Nori. Hybrid quantum circuits: Superconducting circuits interacting with other quantum systems. *Reviews of Modern Physics*, 85(2):623, 2013.

[8] Philipp Treutlein, Claudiu Genes, Klemens Hammerer, Martino Poggio, and Peter Rabl. Hybrid mechanical systems. In *Cavity Optomechanics*, pages 327–351. Springer, 2014.

[9] Markus Aspelmeyer, Tobias J. Kippenberg, and Florian Marquardt. Cavity optomechanics. *Rev. Mod. Phys.*, 86:1391–1452, Dec 2014.

[10] Immanuel Bloch, Jean Dalibard, and Sylvain Nascimbene. Quantum simulations with ultracold quantum gases. *Nature Physics*, 8(4):267–276, 2012.

[11] Rainer Blatt and David Wineland. Entangled states of trapped atomic ions. *Nature*, 453(7198):1008–1015, 2008.

[12] Philip Krantz, Morten Kjaergaard, Fei Yan, Terry P Orlando, Simon Gustavsson, and William D Oliver. A quantum engineer's guide to superconducting qubits. *Applied physics*

reviews, 6(2), 2019.

[13] Michael A Nielsen and Isaac Chuang. Quantum computation and quantum information, 2002.

[14] Richard P Feynman. Quantum mechanical computers. *Optics news*, 11(2):11–20, 1985.

[15] Thaddeus D Ladd, Fedor Jelezko, Raymond Laflamme, Yasunobu Nakamura, Christopher Monroe, and Jeremy Lloyd O'Brien. Quantum computers. *nature*, 464(7285):45–53, 2010.

[16] Nicolas Gisin, Grégoire Ribordy, Wolfgang Tittel, and Hugo Zbinden. Quantum cryptography. *Rev. Mod. Phys.*, 74:145–195, Mar 2002.

[17] L-M Duan, Mikhail D Lukin, J Ignacio Cirac, and Peter Zoller. Long-distance quantum communication with atomic ensembles and linear optics. *Nature*, 414(6862):413–418, 2001.

[18] Christian L Degen, Friedemann Reinhard, and Paola Cappellaro. Quantum sensing. *Reviews of modern physics*, 89(3):035002, 2017.

[19] Vittorio Giovannetti, Seth Lloyd, and Lorenzo Maccone. Advances in quantum metrology. *Nature photonics*, 5(4):222–229, 2011.

[20] Hans Huebl, Christoph W. Zollitsch, Johannes Lotze, Fredrik Hocke, Moritz Greifenstein, Achim Marx, Rudolf Gross, and Sebastian T. B. Goennenwein. High cooperativity in coupled microwave resonator ferrimagnetic insulator hybrids. *Phys. Rev. Lett.*, 111:127003, Sep 2013.

[21] Yutaka Tabuchi, Seiichiro Ishino, Toyofumi Ishikawa, Rekishu Yamazaki, Koji Usami, and Yasunobu Nakamura. Hybridizing ferromagnetic magnons and microwave photons in the quantum limit. *Phys. Rev. Lett.*, 113:083603, Aug 2014.

[22] Xufeng Zhang, Chang-Ling Zou, Liang Jiang, and Hong X. Tang. Strongly coupled magnons and cavity microwave photons. *Phys. Rev. Lett.*, 113:156401, Oct 2014.

[23] Lihui Bai, M. Harder, Y. P. Chen, X. Fan, J. Q. Xiao, and C.-M. Hu. Spin pumping in electrodynamically coupled magnon-photon systems. *Phys. Rev. Lett.*, 114:227201, Jun 2015.

[24] Xufeng Zhang, Chang-Ling Zou, Na Zhu, Florian Marquardt, Liang Jiang, and Hong X

Tang. Magnon dark modes and gradient memory. *Nature communications*, 6(1):1–7, 2015.

[25] Yutaka Tabuchi, Seiichiro Ishino, Atsushi Noguchi, Toyofumi Ishikawa, Rekishu Yamazaki, Koji Usami, and Yasunobu Nakamura. Coherent coupling between a ferromagnetic magnon and a superconducting qubit. *Science*, 349(6246):405–408, 2015.

[26] Andrii V Chumak, Vitaliy I Vasyuchka, Alexander A Serga, and Burkard Hillebrands. Magnon spintronics. *Nature Physics*, 11(6):453–461, 2015.

[27] Xufeng Zhang, Chang-Ling Zou, Liang Jiang, and Hong X Tang. Cavity magnomechanics. *Science advances*, 2(3):e1501286, 2016.

[28] A. Osada, R. Hisatomi, A. Noguchi, Y. Tabuchi, R. Yamazaki, K. Usami, M. Sadgrove, R. Yalla, M. Nomura, and Y. Nakamura. Cavity optomagnonics with spin-orbit coupled photons. *Phys. Rev. Lett.*, 116:223601, Jun 2016.

[29] Lihui Bai, Michael Harder, Paul Hyde, Zhaohui Zhang, Can-Ming Hu, Y. P. Chen, and John Q. Xiao. Cavity mediated manipulation of distant spin currents using a cavity-magnon-polariton. *Phys. Rev. Lett.*, 118:217201, May 2017.

[30] Dengke Zhang, Xiao-Qing Luo, Yi-Pu Wang, Tie-Fu Li, and JQ You. Observation of the exceptional point in cavity magnon-polaritons. *Nature communications*, 8(1):1–6, 2017.

[31] Jie Li, Shi-Yao Zhu, and G. S. Agarwal. Squeezed states of magnons and phonons in cavity magnomechanics. *Phys. Rev. A*, 99:021801, Feb 2019.

[32] Jie Li, Shi-Yao Zhu, and G. S. Agarwal. Magnon-photon-phonon entanglement in cavity magnomechanics. *Phys. Rev. Lett.*, 121:203601, Nov 2018.

[33] Zhedong Zhang, Marlan O. Scully, and Girish S. Agarwal. Quantum entanglement between two magnon modes via kerr nonlinearity driven far from equilibrium. *Phys. Rev. Research*, 1:023021, Sep 2019.

[34] Dany Lachance-Quirion, Yutaka Tabuchi, Arnaud Gloppe, Koji Usami, and Yasunobu Nakamura. Hybrid quantum systems based on magnonics. *Applied Physics Express*, 12(7):070101, 2019.

[35] R. Hisatomi, A. Osada, Y. Tabuchi, T. Ishikawa, A. Noguchi, R. Yamazaki, K. Usami, and

Y. Nakamura. Bidirectional conversion between microwave and light via ferromagnetic magnons. *Phys. Rev. B*, 93:174427, May 2016.

[36] Herbert Walther, Benjamin TH Varcoe, Berthold-Georg Englert, and Thomas Becker. Cavity quantum electrodynamics. *Reports on Progress in Physics*, 69(5):1325, 2006.

[37] Yi-Pu Wang, Guo-Qiang Zhang, Dengke Zhang, Xiao-Qing Luo, Wei Xiong, Shuai-Peng Wang, Tie-Fu Li, C.-M. Hu, and J. Q. You. Magnon kerr effect in a strongly coupled cavity-magnon system. *Phys. Rev. B*, 94:224410, Dec 2016.

[38] Jayakrishnan M. P. Nair, Zhedong Zhang, Marlan O. Scully, and Girish S. Agarwal. Nonlinear spin currents. *Phys. Rev. B*, 102:104415, Sep 2020.

[39] Jayakrishnan M. P. Nair and GS Agarwal. Deterministic quantum entanglement between macroscopic ferrite samples. *Applied Physics Letters*, 117(8):084001, 2020.

[40] Bernard Yurke. Squeezed-state generation using a josephson parametric amplifier. *JOSA B*, 4(10):1551–1557, 1987.

[41] B Yurke, PG Kaminsky, RE Miller, EA Whittaker, AD Smith, AH Silver, and RW Simon. Observation of 4.2-k equilibrium-noise squeezing via a josephson-parametric amplifier. *Physical review letters*, 60(9):764, 1988.

[42] Bernard Yurke, LR Corruccini, PG Kaminsky, LW Rupp, AD Smith, AH Silver, RW Simon, and EA Whittaker. Observation of parametric amplification and deamplification in a josephson parametric amplifier. *Physical Review A*, 39(5):2519, 1989.

[43] Tsuyoshi Yamamoto, K Inomata, M Watanabe, K Matsuba, T Miyazaki, William D Oliver, Yasunobu Nakamura, and JS Tsai. Flux-driven josephson parametric amplifier. *Applied Physics Letters*, 93(4):042510, 2008.

[44] Xuedong Hu. *Quantum fluctuations in condensed matter systems: squeezed states in phonons and josephson junctions*. University of Michigan, 1996.

[45] Fei Xue, Yu-xi Liu, CP Sun, and Franco Nori. Two-mode squeezed states and entangled states of two mechanical resonators. *Physical Review B*, 76(6):064305, 2007.

[46] AM Zagoskin, E Il'Ichev, MW McCutcheon, Jeff F Young, and Franco Nori. Controlled

generation of squeezed states of microwave radiation in a superconducting resonant circuit. *Physical review letters*, 101(25):253602, 2008.

[47] F Mallet, MA Castellanos-Beltran, HS Ku, S Glancy, E Knill, KD Irwin, GC Hilton, LR Vale, and KW Lehnert. Quantum state tomography of an itinerant squeezed microwave field. *Physical Review Letters*, 106(22):220502, 2011.

[48] L Zhong, EP Menzel, R Di Candia, P Eder, M Ihmig, A Baust, M Haeberlein, E Hoffmann, K Inomata, T Yamamoto, et al. Squeezing with a flux-driven josephson parametric amplifier. *New Journal of Physics*, 15(12):125013, 2013.

[49] Kirill G Fedorov, L Zhong, S Pogorzalek, P Eder, M Fischer, J Goetz, E Xie, F Wulschner, K Inomata, T Yamamoto, et al. Displacement of propagating squeezed microwave states. *Physical review letters*, 117(2):020502, 2016.

[50] A Bienfait, P Campagne-Ibarcq, AH Kiilerich, X Zhou, S Probst, JJ Pla, T Schenkel, D Vion, Daniel Estève, JJL Morton, et al. Magnetic resonance with squeezed microwaves. *Physical Review X*, 7(4):041011, 2017.

[51] M Malnou, DA Palken, Leila R Vale, Gene C Hilton, and KW Lehnert. Optimal operation of a josephson parametric amplifier for vacuum squeezing. *Physical Review Applied*, 9(4):044023, 2018.

[52] Debsuvra Mukhopadhyay, Jayakrishnan M. P. Nair, and G. S. Agarwal. Quantum amplification of spin currents in cavity magnonics by a parametric drive induced long-lived mode. *Phys. Rev. B*, 106:184426, Nov 2022.

[53] Robert W Boyd. *Nonlinear optics*. Academic press, 2020.

[54] Sumei Huang and GS Agarwal. Enhancement of cavity cooling of a micromechanical mirror using parametric interactions. *Physical Review A*, 79(1):013821, 2009.

[55] C. Leroux, L. C. G. Govia, and A. A. Clerk. Enhancing cavity quantum electrodynamics via antisqueezing: Synthetic ultrastrong coupling. *Phys. Rev. Lett.*, 120:093602, Mar 2018.

[56] Wei Qin, Adam Miranowicz, Peng-Bo Li, Xin-You Lü, J. Q. You, and Franco Nori. Exponentially enhanced light-matter interaction, cooperativities, and steady-state entanglement

using parametric amplification. *Phys. Rev. Lett.*, 120:093601, Mar 2018.

[57] Peng-Bo Li, Yuan Zhou, Wei-Bo Gao, and Franco Nori. Enhancing spin-phonon and spin-spin interactions using linear resources in a hybrid quantum system. *Phys. Rev. Lett.*, 125:153602, Oct 2020.

[58] CJ Zhu, LL Ping, YP Yang, and Girish S Agarwal. Squeezed light induced symmetry breaking superradiant phase transition. *Physical Review Letters*, 124(7):073602, 2020.

[59] Shaun C Burd, Raghavendra Srinivas, Hannah M Knaack, Wenchao Ge, Andrew C Wilson, David J Wineland, Dietrich Leibfried, John J Bollinger, DTC Allcock, and DH Slichter. Quantum amplification of boson-mediated interactions. *Nature Physics*, 17(8):898–902, 2021.

[60] SC Burd, R Srinivas, JJ Bollinger, AC Wilson, DJ Wineland, D Leibfried, DH Slichter, and DTC Allcock. Quantum amplification of mechanical oscillator motion. *Science*, 364(6446):1163–1165, 2019.

[61] Chia Wei Hsu, Bo Zhen, A Douglas Stone, John D Joannopoulos, and Marin Soljačić. Bound states in the continuum. *Nature Reviews Materials*, 1(9):1–13, 2016.

[62] J Von Neumann and E Wigner. On some peculiar discrete eigenvalues. *Phys. Z*, 30:465–467, 1929.

[63] Frank H. Stillinger and David R. Herrick. Bound states in the continuum. *Phys. Rev. A*, 11:446–454, Feb 1975.

[64] Federico Capasso, Carlo Sirtori, Jerome Faist, Deborah L Sivco, Sung-Nee G Chu, and Alfred Y Cho. Observation of an electronic bound state above a potential well. *Nature*, 358(6387):565–567, 1992.

[65] Asaf Albo, Dan Fekete, and Gad Bahir. Electronic bound states in the continuum above (ga,in)(as,n)/(al,ga)as quantum wells. *Phys. Rev. B*, 85:115307, Mar 2012.

[66] M. Harder, Y. Yang, B. M. Yao, C. H. Yu, J. W. Rao, Y. S. Gui, R. L. Stamps, and C.-M. Hu. Level attraction due to dissipative magnon-photon coupling. *Phys. Rev. Lett.*, 121:137203, Sep 2018.

[67] Biswanath Bhoi, Bosung Kim, Seung-Hun Jang, Junhoe Kim, Jaehak Yang, Young-Jun Cho, and Sang-Koog Kim. Abnormal anticrossing effect in photon-magnon coupling. *Phys. Rev. B*, 99:134426, Apr 2019.

[68] Y. Yang, J.W. Rao, Y.S. Gui, B.M. Yao, W. Lu, and C.-M. Hu. Control of the magnon-photon level attraction in a planar cavity. *Phys. Rev. Appl.*, 11:054023, May 2019.

[69] JW Rao, CH Yu, YT Zhao, YS Gui, XL Fan, DS Xue, and CM Hu. Level attraction and level repulsion of magnon coupled with a cavity anti-resonance. *New Journal of Physics*, 21(6):065001, 2019.

[70] Peng-Chao Xu, J. W. Rao, Y. S. Gui, Xiaofeng Jin, and C.-M. Hu. Cavity-mediated dissipative coupling of distant magnetic moments: Theory and experiment. *Phys. Rev. B*, 100:094415, Sep 2019.

[71] Vahram L. Grigoryan and Ke Xia. Cavity-mediated dissipative spin-spin coupling. *Phys. Rev. B*, 100:014415, Jul 2019.

[72] Yi-Pu Wang, J. W. Rao, Y. Yang, Peng-Chao Xu, Y. S. Gui, B. M. Yao, J. Q. You, and C.-M. Hu. Nonreciprocity and unidirectional invisibility in cavity magnonics. *Phys. Rev. Lett.*, 123:127202, Sep 2019.

[73] Bimu Yao, Tao Yu, Xiang Zhang, Wei Lu, Yongsheng Gui, Can-Ming Hu, and Yaroslav M. Blanter. The microscopic origin of magnon-photon level attraction by traveling waves: Theory and experiment. *Phys. Rev. B*, 100:214426, Dec 2019.

[74] Weichao Yu, Jiongjie Wang, H. Y. Yuan, and Jiang Xiao. Prediction of attractive level crossing via a dissipative mode. *Phys. Rev. Lett.*, 123:227201, Nov 2019.

[75] Jie Zhao, Yulong Liu, Longhao Wu, Chang-Kui Duan, Yu-xi Liu, and Jiangfeng Du. Observation of anti-$\mathscr{P}\mathscr{T}$-symmetry phase transition in the magnon-cavity-magnon coupled system. *Phys. Rev. Appl.*, 13:014053, Jan 2020.

[76] Y. Yang, Yi-Pu Wang, J. W. Rao, Y. S. Gui, B. M. Yao, W. Lu, and C.-M. Hu. Unconventional singularity in anti-parity-time symmetric cavity magnonics. *Phys. Rev. Lett.*, 125:147202, Oct 2020.

[77] Girish S Agarwal. *Quantum optics*. Cambridge University Press, 2012.

[78] Li Ge and Hakan E. Türeci. Antisymmetric $\mathscr{P}\mathscr{T}$-photonic structures with balanced positive- and negative-index materials. *Phys. Rev. A*, 88:053810, Nov 2013.

[79] Peng Peng, Wanxia Cao, Ce Shen, Weizhi Qu, Jianming Wen, Liang Jiang, and Yanhong Xiao. Anti-parity–time symmetry with flying atoms. *Nature Physics*, 12(12):1139–1145, 2016.

[80] Jayakrishnan M. P. Nair, Debsuvra Mukhopadhyay, and G. S. Agarwal. Enhanced sensing of weak anharmonicities through coherences in dissipatively coupled anti-pt symmetric systems. *Phys. Rev. Lett.*, 126:180401, May 2021.

[81] Jayakrishnan M. P. Nair, Debsuvra Mukhopadhyay, and Girish S. Agarwal. Ultralow threshold bistability and generation of long-lived mode in a dissipatively coupled nonlinear system: Application to magnonics. *Phys. Rev. B*, 103:224401, Jun 2021.

[82] Debsuvra Mukhopadhyay, Jayakrishnan M. P. Nair, and Girish S. Agarwal. Anti-$\mathscr{P}\mathscr{T}$ symmetry enhanced interconversion between microwave and optical fields. *Phys. Rev. B*, 105:064405, Feb 2022.

[83] Jayakrishnan M. P. Nair, Debsuvra Mukhopadhyay, and Girish S. Agarwal. Cavity-mediated level attraction and repulsion between magnons. *Phys. Rev. B*, 105:214418, Jun 2022.

[84] Felix Bloch. On the theory of ferromagnetism. *journal for physics*, 61(3-4):206–219, 1930.

[85] T. Holstein and H. Primakoff. Field dependence of the intrinsic domain magnetization of a ferromagnet. *Phys. Rev.*, 58:1098–1113, Dec 1940.

[86] Freeman J Dyson. Thermodynamic behavior of an ideal ferromagnet. *Physical Review*, 102(5):1230, 1956.

[87] Daniel D Stancil and Anil Prabhakar. *Spin waves*, volume 5. Springer, 2009.

[88] Charles Kittel and Ching-yao Fong. *Quantum theory of solids*. Wiley, 1987.

[89] J. Bourhill, N. Kostylev, M. Goryachev, D. L. Creedon, and M. E. Tobar. Ultrahigh cooperativity interactions between magnons and resonant photons in a yig sphere. *Phys. Rev. B*, 93:144420, Apr 2016.

[90] Rui-Chang Shen, Yi-Pu Wang, Jie Li, Shi-Yao Zhu, G. S. Agarwal, and J. Q. You. Long-time memory and ternary logic gate using a multistable cavity magnonic system. *Phys. Rev. Lett.*, 127:183202, Oct 2021.

[91] Jie Li and Shi-Yao Zhu. Entangling two magnon modes via magnetostrictive interaction. *New Journal of Physics*, 21(8):085001, 2019.

[92] C. W. Gardiner and M. J. Collett. Input and output in damped quantum systems: Quantum stochastic differential equations and the master equation. *Phys. Rev. A*, 31:3761–3774, Jun 1985.

[93] C Cohen-Tannoudji, J Dupont-Roc, and G Grynberg. Photons and atoms introduction to quantum electrodynamics. photons et atomes. introduction a l'electrodynamique quantique. 1987.

[94] Serge Haroche and J-M Raimond. *Exploring the quantum: atoms, cavities, and photons*. Oxford university press, 2006.

[95] Chao Song, Kai Xu, Hekang Li, Yu-Ran Zhang, Xu Zhang, Wuxin Liu, Qiujiang Guo, Zhen Wang, Wenhui Ren, Jie Hao, et al. Generation of multicomponent atomic schrödinger cat states of up to 20 qubits. *Science*, 365(6453):574–577, 2019.

[96] Charles Kittel. On the theory of ferromagnetic resonance absorption. *Phys. Rev.*, 73:155–161, Jan 1948.

[97] Dengke Zhang, Xin-Ming Wang, Tie-Fu Li, Xiao-Qing Luo, Weidong Wu, Franco Nori, and JQ You. Cavity quantum electrodynamics with ferromagnetic magnons in a small yttrium-iron-garnet sphere. *npj Quantum Information*, 1(1):1–6, 2015.

[98] L. M. Narducci, R. Gilmore, D. H. Feng, and G. S. Agarwal. Absorption spectrum of optically bistable systems. *Phys. Rev. A*, 20:545–549, Aug 1979.

[99] Th Förster. Intermolecular energy migration and fluorescence. *Annals of Physics*, 437(1-2):55–75, 1948.

[100] Garth A Jones and David S Bradshaw. Resonance energy transfer: from fundamental theory to recent applications. *Frontiers in Physics*, 7:100, 2019.

[101] David P DiVincenzo. Quantum computation. *Science*, 270(5234):255–261, 1995.

[102] Christian Schäfer, Michael Ruggenthaler, Heiko Appel, and Angel Rubio. Modification of excitation and charge transfer in cavity quantum-electrodynamical chemistry. *Proceedings of the National Academy of Sciences*, 116(11):4883–4892, 2019.

[103] David M Coles, Niccolo Somaschi, Paolo Michetti, Caspar Clark, Pavlos G Lagoudakis, Pavlos G Savvidis, and David G Lidzey. Polariton-mediated energy transfer between organic dyes in a strongly coupled optical microcavity. *Nature materials*, 13(7):712–719, 2014.

[104] Joel Yuen-Zhou and Vinod M Menon. Polariton chemistry: Thinking inside the (photon) box. *Proceedings of the National Academy of Sciences*, 116(12):5214–5216, 2019.

[105] Carlton M. Caves. Quantum-mechanical noise in an interferometer. *Phys. Rev. D*, 23:1693–1708, Apr 1981.

[106] William G Unruh. Quantum noise in the interferometer detector. In *Quantum Optics, Experimental Gravity, and Measurement Theory*, pages 647–660. Springer, 1983.

[107] Benjamin J Lawrie, Paul D Lett, Alberto M Marino, and Raphael C Pooser. Quantum sensing with squeezed light. *Acs Photonics*, 6(6):1307–1318, 2019.

[108] G. S. Agarwal and L. Davidovich. Quantifying quantum-amplified metrology via fisher information. *Phys. Rev. Research*, 4:L012014, Feb 2022.

[109] Michael A Taylor and Warwick P Bowen. Quantum metrology and its application in biology. *Physics Reports*, 615:1–59, 2016.

[110] Nikita Kostylev, Maxim Goryachev, and Michael E Tobar. Superstrong coupling of a microwave cavity to yttrium iron garnet magnons. *Applied Physics Letters*, 108(6):062402, 2016.

[111] Wei Xiong, Miao Tian, Guo-Qiang Zhang, and J. Q. You. Strong long-range spin-spin coupling via a kerr magnon interface. *Phys. Rev. B*, 105:245310, Jun 2022.

[112] R. Movshovich, B. Yurke, P. G. Kaminsky, A. D. Smith, A. H. Silver, R. W. Simon, and M. V. Schneider. Observation of zero-point noise squeezing via a josephson-parametric amplifier. *Phys. Rev. Lett.*, 65:1419–1422, Sep 1990.

[113] MA Castellanos-Beltran, KD Irwin, GC Hilton, LR Vale, and KW Lehnert. Amplification and squeezing of quantum noise with a tunable josephson metamaterial. *Nature Physics*, 4(12):929–931, 2008.

[114] C. M. Wilson, T. Duty, M. Sandberg, F. Persson, V. Shumeiko, and P. Delsing. Photon generation in an electromagnetic cavity with a time-dependent boundary. *Phys. Rev. Lett.*, 105:233907, Dec 2010.

[115] Jing Zhang, Chenguang Ye, Feng Gao, and Min Xiao. Phase-sensitive manipulations of a squeezed vacuum field in an optical parametric amplifier inside an optical cavity. *Phys. Rev. Lett.*, 101:233602, Dec 2008.

[116] Carl M. Bender and Stefan Boettcher. Real spectra in non-hermitian hamiltonians having *PT* symmetry. *Phys. Rev. Lett.*, 80:5243–5246, Jun 1998.

[117] Xin Wang and Jin-Hui Wu. Optical -symmetry and -antisymmetry in coherently driven atomic lattices. *Optics express*, 24(4):4289–4298, 2016.

[118] You-Lin Chuang, Ray-Kuang Lee, et al. Realization of simultaneously parity-time-symmetric and parity-time-antisymmetric susceptibilities along the longitudinal direction in atomic systems with all optical controls. *Optics express*, 26(17):21969–21978, 2018.

[119] Yue Jiang, Yefeng Mei, Ying Zuo, Yanhua Zhai, Jensen Li, Jianming Wen, and Shengwang Du. Anti-parity-time symmetric optical four-wave mixing in cold atoms. *Phys. Rev. Lett.*, 123:193604, Nov 2019.

[120] Diana A Antonosyan, Alexander S Solntsev, and Andrey A Sukhorukov. Parity-time anti-symmetric parametric amplifier. *Optics letters*, 40(20):4575–4578, 2015.

[121] Fan Yang, Yong-Chun Liu, and Li You. Anti-$\mathscr{P}\mathscr{T}$ symmetry in dissipatively coupled optical systems. *Phys. Rev. A*, 96:053845, Nov 2017.

[122] Vladimir V. Konotop and Dmitry A. Zezyulin. Odd-time reversal $\mathscr{P}\mathscr{T}$ symmetry induced by an anti-$\mathscr{P}\mathscr{T}$-symmetric medium. *Phys. Rev. Lett.*, 120:123902, Mar 2018.

[123] Ying Li, Yu-Gui Peng, Lei Han, Mohammad-Ali Miri, Wei Li, Meng Xiao, Xue-Feng Zhu, Jianlin Zhao, Andrea Alù, Shanhui Fan, et al. Anti–parity-time symmetry in diffusive sys-

tems. *Science*, 364(6436):170–173, 2019.

[124] Jingwei Wen, Guoqing Qin, Chao Zheng, Shijie Wei, Xiangyu Kong, Tao Xin, and Guilu Long. Observation of information flow in the anti--symmetric system with nuclear spins. *npj Quantum Information*, 6(1):28, 2020.

[125] Youngsun Choi, Choloong Hahn, Jae Woong Yoon, and Seok Ho Song. Observation of an anti-pt-symmetric exceptional point and energy-difference conserving dynamics in electrical circuit resonators. *Nature communications*, 9(1):2182, 2018.

[126] Girish S Agarwal. Quantum statistical theories of spontaneous emission and their relation to other approaches. In *Quantum Optics*, pages 1–128. Springer, 1974.

[127] Eduardo Gil-Santos, Daniel Ramos, Javier Martínez, Marta Fernández-Regúlez, Ricardo García, Álvaro San Paulo, Montserrat Calleja, and Javier Tamayo. Nanomechanical mass sensing and stiffness spectrometry based on two-dimensional vibrations of resonant nanowires. *Nature nanotechnology*, 5(9):641–645, 2010.

[128] Jiangang Zhu, Sahin Kaya Ozdemir, Yun-Feng Xiao, Lin Li, Lina He, Da-Ren Chen, and Lan Yang. On-chip single nanoparticle detection and sizing by mode splitting in an ultrahigh-q microresonator. *Nature photonics*, 4(1):46, 2010.

[129] Lina He, Şahin Kaya Özdemir, Jiangang Zhu, Woosung Kim, and Lan Yang. Detecting single viruses and nanoparticles using whispering gallery microlasers. *Nature nanotechnology*, 6(7):428–432, 2011.

[130] Frank Vollmer and Lan Yang. Review label-free detection with high-q microcavities: a review of biosensing mechanisms for integrated devices. *Nanophotonics*, 1(3-4):267–291, 2012.

[131] S. Forstner, S. Prams, J. Knittel, E. D. van Ooijen, J. D. Swaim, G. I. Harris, A. Szorkovszky, W. P. Bowen, and H. Rubinsztein-Dunlop. Cavity optomechanical magnetometer. *Phys. Rev. Lett.*, 108:120801, Mar 2012.

[132] Long Chang, Xiaoshun Jiang, Shiyue Hua, Chao Yang, Jianming Wen, Liang Jiang, Guanyu Li, Guanzhong Wang, and Min Xiao. Parity–time symmetry and variable optical isolation

in active–passive-coupled microresonators. *Nature photonics*, 8(7):524–529, 2014.

[133] Ievgen I. Arkhipov, Adam Miranowicz, Omar Di Stefano, Roberto Stassi, Salvatore Savasta, Franco Nori, and Şahin K. Özdemir. Scully-lamb quantum laser model for parity-time-symmetric whispering-gallery microcavities: Gain saturation effects and nonreciprocity. *Phys. Rev. A*, 99:053806, May 2019.

[134] WD Heiss. The physics of exceptional points. *Journal of Physics A: Mathematical and Theoretical*, 45(44):444016, 2012.

[135] Haitan Xu, David Mason, Luyao Jiang, and JGE Harris. Topological energy transfer in an optomechanical system with exceptional points. *Nature*, 537(7618):80–83, 2016.

[136] Hui Cao and Jan Wiersig. Dielectric microcavities: Model systems for wave chaos and non-hermitian physics. *Rev. Mod. Phys.*, 87:61–111, Jan 2015.

[137] Weijian Chen, Şahin Kaya Özdemir, Guangming Zhao, Jan Wiersig, and Lan Yang. Exceptional points enhance sensing in an optical microcavity. *Nature*, 548(7666):192–196, 2017.

[138] Hossein Hodaei, Absar U Hassan, Steffen Wittek, Hipolito Garcia-Gracia, Ramy El-Ganainy, Demetrios N Christodoulides, and Mercedeh Khajavikhan. Enhanced sensitivity at higher-order exceptional points. *Nature*, 548(7666):187–191, 2017.

[139] Zhicheng Xiao, Huanan Li, Tsampikos Kottos, and Andrea Alù. Enhanced sensing and nondegraded thermal noise performance based on $\mathscr{PT}$-symmetric electronic circuits with a sixth-order exceptional point. *Phys. Rev. Lett.*, 123:213901, Nov 2019.

[140] Zin Lin, Adi Pick, Marko Lončar, and Alejandro W Rodriguez. Enhanced spontaneous emission at third-order dirac exceptional points in inverse-designed photonic crystals. *Physical review letters*, 117(10):107402, 2016.

[141] Jan Wiersig. Enhancing the sensitivity of frequency and energy splitting detection by using exceptional points: Application to microcavity sensors for single-particle detection. *Phys. Rev. Lett.*, 112:203901, May 2014.

[142] Pai-Yen Chen and Jeil Jung. $\mathscr{PT}$ symmetry and singularity-enhanced sensing based on

photoexcited graphene metasurfaces. *Phys. Rev. Applied*, 5:064018, Jun 2016.

[143] Mohammad-Ali Miri and Andrea Alu. Exceptional points in optics and photonics. *Science*, 363(6422), 2019.

[144] Xufeng Zhang, Kun Ding, Xianjing Zhou, Jing Xu, and Dafei Jin. Experimental observation of an exceptional surface in synthetic dimensions with magnon polaritons. *Phys. Rev. Lett.*, 123:237202, Dec 2019.

[145] Chao Zeng, Yong Sun, Guo Li, Yunhui Li, Haitao Jiang, Yaping Yang, and Hong Chen. Enhanced sensitivity at high-order exceptional points in a passive wireless sensing system. *Optics express*, 27(20):27562–27572, 2019.

[146] Jan Wiersig. Sensors operating at exceptional points: General theory. *Phys. Rev. A*, 93:033809, Mar 2016.

[147] Carl M Bender, MV Berry, and Aikaterini Mandilara. Generalized pt symmetry and real spectra. *Journal of Physics A: Mathematical and General*, 35(31):L467, 2002.

[148] Carl M. Bender, Dorje C. Brody, and Hugh F. Jones. Complex extension of quantum mechanics. *Phys. Rev. Lett.*, 89:270401, Dec 2002.

[149] R. El-Ganainy, K. G. Makris, D. N. Christodoulides, and Ziad H. Musslimani. Theory of coupled optical pt-symmetric structures. *Opt. Lett.*, 32(17):2632–2634, Sep 2007.

[150] GS Agarwal. Anisotropic vacuum-induced interference in decay channels. *Physical Review Letters*, 84(24):5500, 2000.

[151] Pankaj K Jha, Xingjie Ni, Chihhui Wu, Yuan Wang, and Xiang Zhang. Metasurface-enabled remote quantum interference. *Physical review letters*, 115(2):025501, 2015.

[152] Emmanuel Lassalle, Philippe Lalanne, Syed Aljunid, Patrice Genevet, Brian Stout, Thomas Durt, and David Wilkowski. Long-lifetime coherence in a quantum emitter induced by a metasurface. *Physical Review A*, 101(1):013837, 2020.

[153] Danil Kornovan, Mihail Petrov, and Ivan Iorsh. Noninverse dynamics of a quantum emitter coupled to a fully anisotropic environment. *Physical Review A*, 100(3):033840, 2019.

[154] Marlan O Scully, Kimberly R Chapin, Konstantin E Dorfman, Moochan Barnabas Kim,

and Anatoly Svidzinsky. Quantum heat engine power can be increased by noise-induced coherence. *Proceedings of the National Academy of Sciences*, 108(37):15097–15100, 2011.

[155] Martin Kiffner, M Macovei, J Evers, and CH Keitel. Vacuum-induced processes in multilevel atoms. In *Progress in Optics*, volume 55, pages 85–197. Elsevier, 2010.

[156] Christoph H Keitel. Narrowing spontaneous emission without intensity reduction. *Physical review letters*, 83(7):1307, 1999.

[157] Peng Zhou and S Swain. Quantum interference in resonance fluorescence for a driven v atom. *Physical Review A*, 56(4):3011, 1997.

[158] E Paspalakis and PL Knight. Phase control of spontaneous emission. *Physical review letters*, 81(2):293, 1998.

[159] Emmanuel Paspalakis, Christoph H Keitel, and Peter L Knight. Fluorescence control through multiple interference mechanisms. *Physical Review A*, 58(6):4868, 1998.

[160] Kilian P Heeg, Hans-Christian Wille, Kai Schlage, Tatyana Guryeva, Daniel Schumacher, Ingo Uschmann, Kai S Schulze, Berit Marx, Tino Kämpfer, Gerhard G Paulus, et al. Vacuum-assisted generation and control of atomic coherences at x-ray energies. *Physical review letters*, 111(7):073601, 2013.

[161] Konstantin E Dorfman, Dmitri V Voronine, Shaul Mukamel, and Marlan O Scully. Photosynthetic reaction center as a quantum heat engine. *Proceedings of the National Academy of Sciences*, 110(8):2746–2751, 2013.

[162] Marlan O. Scully. Quantum photocell: Using quantum coherence to reduce radiative recombination and increase efficiency. *Phys. Rev. Lett.*, 104:207701, May 2010.

[163] Anatoly A. Svidzinsky, Konstantin E. Dorfman, and Marlan O. Scully. Enhancing photovoltaic power by fano-induced coherence. *Phys. Rev. A*, 84:053818, Nov 2011.

[164] Amro Dodin and Paul Brumer. Light-induced processes in nature: Coherences in the establishment of the nonequilibrium steady state in model retinal isomerization. *The Journal of chemical physics*, 150(18):184304, 2019.

[165] J. W. Rao, Y. P. Wang, Y. Yang, T. Yu, Y. S. Gui, X. L. Fan, D. S. Xue, and C.-M. Hu. Inter-

actions between a magnon mode and a cavity photon mode mediated by traveling photons. *Phys. Rev. B*, 101:064404, Feb 2020.

[166] Bimu Yao, Tao Yu, YS Gui, JW Rao, YT Zhao, W Lu, and C-M Hu. Coherent control of magnon radiative damping with local photon states. *Communications Physics*, 2(1):1–8, 2019.

[167] Yi-Pu Wang and Can-Ming Hu. Dissipative couplings in cavity magnonics. *Journal of Applied Physics*, 127(13):130901, 2020.

[168] A. Metelmann and A. A. Clerk. Nonreciprocal photon transmission and amplification via reservoir engineering. *Phys. Rev. X*, 5:021025, Jun 2015.

[169] S. P. Wolski, D. Lachance-Quirion, Y. Tabuchi, S. Kono, A. Noguchi, K. Usami, and Y. Nakamura. Dissipation-based quantum sensing of magnons with a superconducting qubit. *Phys. Rev. Lett.*, 125:117701, Sep 2020.

[170] Hong Wei, Zhipeng Li, Xiaorui Tian, Zhuoxian Wang, Fengzi Cong, Ning Liu, Shunping Zhang, Peter Nordlander, Naomi J Halas, and Hongxing Xu. Quantum dot-based local field imaging reveals plasmon-based interferometric logic in silver nanowire networks. *Nano letters*, 11(2):471–475, 2011.

[171] Jens Koch, Terri M. Yu, Jay Gambetta, A. A. Houck, D. I. Schuster, J. Majer, Alexandre Blais, M. H. Devoret, S. M. Girvin, and R. J. Schoelkopf. Charge-insensitive qubit design derived from the cooper pair box. *Phys. Rev. A*, 76:042319, Oct 2007.

[172] I. Thanopulos, V. Yannopapas, and E. Paspalakis. Non-markovian dynamics in plasmon-induced spontaneous emission interference. *Phys. Rev. B*, 95:075412, Feb 2017.

[173] N. R. Bernier, L. D. Tóth, A. K. Feofanov, and T. J. Kippenberg. Level attraction in a microwave optomechanical circuit. *Phys. Rev. A*, 98:023841, Aug 2018.

[174] Ze-Liang Xiang, Sahel Ashhab, J. Q. You, and Franco Nori. Hybrid quantum circuits: Superconducting circuits interacting with other quantum systems. *Rev. Mod. Phys.*, 85:623–653, Apr 2013.

[175] Osama R Bilal, André Foehr, and Chiara Daraio. Bistable metamaterial for switch-

ing and cascading elastic vibrations. *Proceedings of the National Academy of Sciences*, 114(18):4603–4606, 2017.

[176] Feng Li, Paul Anzel, Jinkyu Yang, Panayotis G Kevrekidis, and Chiara Daraio. Granular acoustic switches and logic elements. *Nature communications*, 5(1):1–6, 2014.

[177] Sahab Babaee, Nicolas Viard, Pai Wang, Nicholas X Fang, and Katia Bertoldi. Harnessing deformation to switch on and off the propagation of sound. *Advanced Materials*, 28(8):1631–1635, 2016.

[178] Viacheslav Kubytskyi, Svend-Age Biehs, and Philippe Ben-Abdallah. Radiative bistability and thermal memory. *Phys. Rev. Lett.*, 113:074301, Aug 2014.

[179] Lei Wang and Baowen Li. Thermal memory: A storage of phononic information. *Phys. Rev. Lett.*, 101:267203, Dec 2008.

[180] Huilai Zhang, Ran Huang, Sheng-Dian Zhang, Ying Li, Cheng-Wei Qiu, Franco Nori, and Hui Jing. Breaking anti-pt symmetry by spinning a resonator. *Nano Letters*, 20(10):7594–7599, 2020.

[181] Galina Khitrova, HM Gibbs, M Kira, Stephan W Koch, and Axel Scherer. Vacuum rabi splitting in semiconductors. *Nature physics*, 2(2):81–90, 2006.

[182] G. S. Agarwal. Vacuum-field rabi splittings in microwave absorption by rydberg atoms in a cavity. *Phys. Rev. Lett.*, 53:1732–1734, Oct 1984.

[183] AP Seyranian, ON Kirillov, and AA Mailybaev. Coupling of eigenvalues of complex matrices at diabolic and exceptional points. *Journal of Physics A: Mathematical and General*, 38(8):1723, 2005.

[184] F Keck, HJ Korsch, and S Mossmann. Unfolding a diabolic point: a generalized crossing scenario. *Journal of Physics A: Mathematical and General*, 36(8):2125, 2003.

[185] Dany Lachance-Quirion, Yutaka Tabuchi, Seiichiro Ishino, Atsushi Noguchi, Toyofumi Ishikawa, Rekishu Yamazaki, and Yasunobu Nakamura. Resolving quanta of collective spin excitations in a millimeter-sized ferromagnet. *Science advances*, 3(7):e1603150, 2017.

[186] H. Maier-Flaig, M. Harder, R. Gross, H. Huebl, and S. T. B. Goennenwein. Spin pumping

in strongly coupled magnon-photon systems. *Phys. Rev. B*, 94:054433, Aug 2016.

[187] N. J. Lambert, J. A. Haigh, S. Langenfeld, A. C. Doherty, and A. J. Ferguson. Cavity-mediated coherent coupling of magnetic moments. *Phys. Rev. A*, 93:021803, Feb 2016.

[188] Bimu Yao, YS Gui, JW Rao, S Kaur, XS Chen, W Lu, Y Xiao, H Guo, K-P Marzlin, and C-M Hu. Cooperative polariton dynamics in feedback-coupled cavities. *Nature communications*, 8(1):1–6, 2017.

[189] Yong Sup Ihn, Su-Yong Lee, Dongkyu Kim, Sin Hyuk Yim, and Zaeill Kim. Coherent multimode conversion from microwave to optical wave via a magnon-cavity hybrid system. *Phys. Rev. B*, 102:064418, Aug 2020.

[190] Debsuvra Mukhopadhyay, Jayakrishnan MP Nair, and Girish S Agarwal. Anti-pt-symmetry-enhanced interconversion between microwave and optical fields. *arXiv preprint arXiv:2111.01335*, 2021.

[191] C Dembowski, H-D Gräf, HL Harney, A Heine, WD Heiss, H Rehfeld, and A Richter. Experimental observation of the topological structure of exceptional points. *Physical review letters*, 86(5):787, 2001.

[192] Jörg Doppler, Alexei A Mailybaev, Julian Böhm, Ulrich Kuhl, Adrian Girschik, Florian Libisch, Thomas J Milburn, Peter Rabl, Nimrod Moiseyev, and Stefan Rotter. Dynamically encircling an exceptional point for asymmetric mode switching. *Nature*, 537(7618):76–79, 2016.

[193] Ramy El-Ganainy, Konstantinos G Makris, Mercedeh Khajavikhan, Ziad H Musslimani, Stefan Rotter, and Demetrios N Christodoulides. Non-hermitian physics and pt symmetry. *Nature Physics*, 14(1):11–19, 2018.

[194] Şahin Kaya Özdemir, Stefan Rotter, Franco Nori, and L Yang. Parity–time symmetry and exceptional points in photonics. *Nature materials*, 18(8):783–798, 2019.

[195] G. S. Agarwal, R. R. Puri, and R. P. Singh. Atomic schrödinger cat states. *Phys. Rev. A*, 56:2249–2254, Sep 1997.

[196] Said Rahimzadeh-Kalaleh Rodriguez. Classical and quantum distinctions between weak

and strong coupling. *European Journal of Physics*, 37(2):025802, 2016.

[197] W Casteels, R Rota, F Storme, and C Ciuti. Probing photon correlations in the dark sites of geometrically frustrated cavity lattices. *Physical Review A*, 93(4):043833, 2016.

[198] K.-J. Boller, A. Imamoğlu, and S. E. Harris. Observation of electromagnetically induced transparency. *Phys. Rev. Lett.*, 66:2593–2596, May 1991.

[199] CL Garrido Alzar, MAG Martinez, and P Nussenzveig. Classical analog of electromagnetically induced transparency. *American Journal of Physics*, 70(1):37–41, 2002.

[200] Brian Julsgaard, Alexander Kozhekin, and Eugene S Polzik. Experimental long-lived entanglement of two macroscopic objects. *Nature*, 413(6854):400–403, 2001.

[201] Chin-Wen Chou, Hugues De Riedmatten, Daniel Felinto, Sergey V Polyakov, Steven J Van Enk, and H Jeff Kimble. Measurement-induced entanglement for excitation stored in remote atomic ensembles. *Nature*, 438(7069):828–832, 2005.

[202] P Zarkeshian, C Deshmukh, N Sinclair, SK Goyal, GH Aguilar, P Lefebvre, M Grimau Puigibert, VB Verma, F Marsili, MD Shaw, et al. Entanglement between more than two hundred macroscopic atomic ensembles in a solid. *Nature communications*, 8(1):906, 2017.

[203] Robert McConnell, Hao Zhang, Jiazhong Hu, Senka Ćuk, and Vladan Vuletić. Entanglement with negative wigner function of almost 3,000 atoms heralded by one photon. *Nature*, 519(7544):439–442, 2015.

[204] Ralf Riedinger, Andreas Wallucks, Igor Marinković, Clemens Löschnauer, Markus Aspelmeyer, Sungkun Hong, and Simon Gröblacher. Remote quantum entanglement between two micromechanical oscillators. *Nature*, 556(7702):473–477, 2018.

[205] CF Ockeloen-Korppi, E Damskägg, J-M Pirkkalainen, M Asjad, AA Clerk, F Massel, MJ Woolley, and MA Sillanpää. Stabilized entanglement of massive mechanical oscillators. *Nature*, 556(7702):478–482, 2018.

[206] TA Palomaki, JD Teufel, RW Simmonds, and Konrad W Lehnert. Entangling mechanical motion with microwave fields. *Science*, 342(6159):710–713, 2013.

[207] Maxim Goryachev, Warrick G. Farr, Daniel L. Creedon, Yaohui Fan, Mikhail Kostylev, and

Michael E. Tobar. High-cooperativity cavity qed with magnons at microwave frequencies. *Phys. Rev. Appl.*, 2:054002, Nov 2014.

[208] Nicim Zagury and Sergio M. Rezende. Theory of macroscopic excitations of magnons. *Phys. Rev. B*, 4:201–209, Jul 1971.

[209] Xuedong Hu and Franco Nori. Squeezed phonon states: Modulating quantum fluctuations of atomic displacements. *Phys. Rev. Lett.*, 76:2294–2297, Mar 1996.

[210] Xuedong Hu and Franco Nori. Phonon squeezed states generated by second-order raman scattering. *Phys. Rev. Lett.*, 79:4605–4608, Dec 1997.

[211] GA Garrett, AG Rojo, AK Sood, JF Whitaker, and R Merlin. Vacuum squeezing of solids: macroscopic quantum states driven by light pulses. *Science*, 275(5306):1638–1640, 1997.

[212] Xuedong Hu and Franco Nori. Phonon squeezed states: quantum noise reduction in solids. *Physica B: Condensed Matter*, 263:16–29, 1999.

[213] Andreas Sizmann and Gerd Leuchs. V the optical kerr effect and quantum optics in fibers. *Progress in optics*, 39:373–469, 1999.

[214] C. Genes, D. Vitali, and P. Tombesi. Emergence of atom-light-mirror entanglement inside an optical cavity. *Phys. Rev. A*, 77:050307, May 2008.

[215] C. W. Gardiner. Inhibition of atomic phase decays by squeezed light: A direct effect of squeezing. *Phys. Rev. Lett.*, 56:1917–1920, May 1986.

[216] Patrick Christopher Parks and Volker Hahn. *Stability theory*. Prentice-Hall, Inc., 1993.

[217] G. Vidal and R. F. Werner. Computable measure of entanglement. *Phys. Rev. A*, 65:032314, Feb 2002.

[218] M. B. Plenio. Logarithmic negativity: A full entanglement monotone that is not convex. *Phys. Rev. Lett.*, 95:090503, Aug 2005.

[219] R. Simon. Peres-horodecki separability criterion for continuous variable systems. *Phys. Rev. Lett.*, 84:2726–2729, Mar 2000.

[220] Lu-Ming Duan, G. Giedke, J. I. Cirac, and P. Zoller. Inseparability criterion for continuous variable systems. *Phys. Rev. Lett.*, 84:2722–2725, Mar 2000.

[221] Stefano Mancini, Vittorio Giovannetti, David Vitali, and Paolo Tombesi. Entangling macroscopic oscillators exploiting radiation pressure. *Phys. Rev. Lett.*, 88:120401, Mar 2002.

[222] C. Eichler, D. Bozyigit, and A. Wallraff. Characterizing quantum microwave radiation and its entanglement with superconducting qubits using linear detectors. *Phys. Rev. A*, 86:032106, Sep 2012.

[223] Rui-Chang Shen, Yi-Pu Wang, Jie Li, Shi-Yao Zhu, GS Agarwal, and JQ You. Long-time memory and ternary logic gate using a multistable cavity magnonic system. *Physical Review Letters*, 127(18):183202, 2021.

[224] H. Pan, Y. Yang, Z. H. An, and C.-M. Hu. Bistability in dissipatively coupled cavity magnonics. *Phys. Rev. B*, 106:054425, Aug 2022.

APPENDIX A

DERIVATION OF THE MASTER EQUATION FOR A CHAIN OF EMITTERS COUPLED TO A WAVEGUIDE

As depicted in Fig. (A1), we consider an N-mode system (S) interacting dissipatively through a shared one-dimensional bath (B) aligned along the x-axis [1]. Keeping the model very basic, we split the net Hamiltonian $\mathscr{H}$ into three contributions given by

$$\begin{aligned}
\mathscr{H}_S &= \hbar \sum_{\lambda=1}^{N} \omega_\lambda c_\lambda^\dagger c_\lambda, \\
\mathscr{H}_B &= \hbar \sum_{k} \omega_k a_k^\dagger a_k, \\
\mathscr{H}_{SB} &= i\hbar \sum_{k} \sum_{\lambda=1}^{2} g_{k\lambda} (a_k e^{ikx_\lambda} - a_k^\dagger e^{-ikx_\lambda})(c_\lambda + c_\lambda^\dagger),
\end{aligned} \tag{A.1}$$

where we assume that the mode c_λ is coupled to the waveguide at the location $x = x_\lambda$. The coupling coefficients $g_{k\lambda}$'s are assumed to be real. Here, $\mathscr{H}_{SB}$ exemplifies a typical two-body interaction among spatially separated modes with electromagnetic field quantized in a one-dimensional

[1]The derivation presented is reprinted with permission from *Anti-$\mathscr{P}\mathscr{T}$ symmetry enhanced interconversion between microwave and optical fields* by D. Mukhopadhyay, J. M. P. Nair and G. S. Agarwal, Phys. Rev. B **105**, 064405 (2022), published by the American Physical Society.

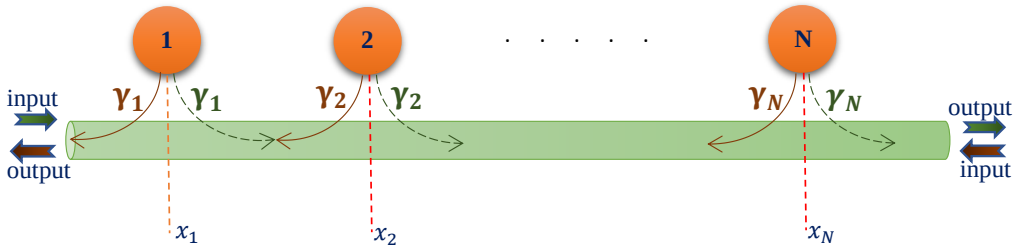

Figure A.1: An array of N single-mode quantum emitters coupled to the evanescent field of a one-dimensional waveguide, with $\gamma_\alpha = \kappa_{\alpha\alpha}$ denoting the individual coupling rates. The waveguide can be adiabatically eliminated to yield the master equation of the emitter chain.

geometry. We can adiabatically eliminate the reservoir degrees of freedom to obtain the master equation under the Markov approximation as

$$\begin{aligned}\dot{\rho}_S(t) = &-\frac{i}{\hbar}[\mathscr{H}_S, \rho_S(t)] \\ &-\frac{1}{\hbar^2}\int_0^\infty \mathrm{d}\tau\, \mathrm{Tr}_B[\mathscr{H}_{SB}, [\mathscr{H}_{SB}(-\tau), \rho_S(t)\rho_B]]\end{aligned} \tag{A.2}$$

where $\mathscr{O}(-\tau) = \exp\Big[-\frac{i}{\hbar}(\mathscr{H}_S + \mathscr{H}_B)\tau\Big]\mathscr{O}\exp\Big[\frac{i}{\hbar}(\mathscr{H}_S + \mathscr{H}_B)\tau\Big]$, and ρ_B is the initial state of the bath [77]. Idealizing the bath to be a thermalized vacuum at zero temperature, the reservoir signatures would encoded as $\langle a_k a_{k'}\rangle = \left\langle a_k^\dagger a_{k'}\right\rangle = 0$ and $\left\langle a_k a_{k'}^\dagger\right\rangle = \delta_{k,k'}$. Substituting these expressions into (21), we obtain $\tau-$integrals which, for the moment, can be expressed in terms of

$$\mathscr{T}_{k\mu}^{(\pm)} = \int_0^\infty \mathrm{d}\tau e^{i(\omega_\mu \pm \omega_k)\tau} = \pi\delta(\omega_\mu \pm \omega_k) + i\mathrm{P}\frac{1}{(\omega_\mu \pm \omega_k)}, \tag{A.3}$$

where $\mathrm{P}(1/x)$ denotes the Cauchy Principal Value of its argument. Since ω_k's are all positive, terms of the form $\delta(\omega_\mu + \omega_k)$ can be stamped out. In light of these simplifications, we can compactify (21) into the form

$$\dot{\rho}_S = -\frac{i}{\hbar}[\mathscr{H}_S, \rho_S] - \frac{1}{\hbar^2}\sum_{\alpha,\beta=1}^{N}(\mathscr{W}_{\alpha\beta} + \mathscr{W}_{\alpha\beta}^\dagger), \tag{A.4}$$

where a typical contribution would appear as

$$\begin{aligned}\mathscr{W}_{\alpha\beta} = \sum_k g_{k\alpha}g_{k\beta}e^{ik(x_\alpha - x_\beta)}\Big[&\mathscr{T}_{k\beta}^{(-)}(c_\alpha^\dagger c_\beta\rho_S - c_\beta\rho_S c_\alpha^\dagger) + \\ &\mathscr{T}_{k\beta}^{(+)}(c_\alpha c_\beta^\dagger\rho_S - c_\beta^\dagger\rho_S c_\alpha)\Big].\end{aligned} \tag{A.5}$$

We have dropped the fast-oscillating terms that go as $c_\alpha c_\beta$ or $c_\alpha^\dagger c_\beta^\dagger$ under the purview of the rotating wave approximation. Using a linearized approximation to the reservoir frequencies by letting $\omega_k \approx v_g|k|$, we take the continuum limit $\sum_k \to \frac{L}{2\pi}\int \mathrm{d}k$ in computing $\mathscr{W}_{\alpha\beta}$ and $\mathscr{W}_{\alpha\beta}^\dagger$. With the identification $\Lambda_\pm = \frac{1}{\pi}\mathrm{P}\int_{-\infty}^{\infty}\mathrm{d}k\frac{e^{ik(x_\alpha - x_\beta)}}{\omega_\beta \pm v_g|k|}$ and the assumption that the coupling to the modes is independent of the

field's propagation direction, the cardinal intermediate relations could be codified as

$$\int_{-\infty}^{\infty} \mathrm{d}k e^{\pm ikx_{\alpha\beta}} \delta(\omega_\beta - v_g|k|) = \frac{2}{v_g} \cos\Big(k_\beta x_{\alpha\beta}\Big),$$
$$\Lambda_+ + \Lambda_- = \frac{2}{v_g} \sin\Big(k_\beta x_{\alpha\beta}\Big), \tag{A.6}$$

where $x_{\alpha\beta} = \Big|x_\alpha - x_\beta\Big|$ and $k_\beta = \omega_\beta / v_g$. Terms like $\mathrm{P}\int_{-\infty}^{\infty} \mathrm{d}k \frac{1}{\omega_\beta \pm v_g|k|}$ get reflected as small frequency shifts in ω_1 and ω_2, which can be neglected. Then, collecting the like terms together in (23) and exploiting the preceding relations in (24) and (25), we obtain the full master equation for the dissipative dynamics of S:

$$\dot{\rho}_S = -\frac{i}{\hbar}[\mathscr{H}_S, \rho_S] - \sum_{\alpha,\beta=1}^{N} \kappa_{\alpha\beta}(c_\alpha^\dagger c_\beta \rho_S - 2c_\beta \rho_S c_\alpha^\dagger + \rho_S c_\alpha^\dagger c_\beta)$$
$$-i \sum_{\alpha \neq \beta} \Omega_{\alpha\beta}[c_\alpha^\dagger c_\beta, \rho_S], \tag{A.7}$$

where the off-diagonal coefficients $\kappa_{\alpha\beta}$, for $\alpha \neq \beta$, signify dissipative couplings, while $\Omega_{\alpha\beta}$ simulate dispersive interactions. The relevant coefficients are given by

$$\kappa_{\alpha\beta} = \frac{g_\alpha^2 L}{v_g} \delta_{\alpha\beta} + \Gamma_{\alpha\beta} \cos\phi_{\alpha\beta}(1 - \delta_{\alpha\beta}),$$
$$\Gamma_{\alpha\beta} = (\kappa_{\alpha\alpha}\kappa_{\beta\beta})^{1/2} = \frac{g_\alpha g_\beta L}{v_g},$$
$$\Omega_{\alpha\beta} = \Gamma_{\alpha\beta} \sin\phi_{\alpha\beta}, \tag{A.8}$$

where, in view of the proximity between the transition frequencies, it is assumed that $k_\lambda \approx k_0 = \omega_0 / v_g \; \forall \lambda \in \{1, N\}$. $g_{k\alpha} \approx g_\alpha$, and $\{k_0, \omega_0\}$ is the central waveguide mode in the vicinity of which the linear dispersion holds valid. The phases $\phi_{\alpha\beta}$ are defined as $\phi_{\alpha\beta} = k_0 x_{\alpha\beta}$, and $g_{k\lambda}$'s are taken to be k-independent. When $\phi_{\alpha\beta}$'s are integral multiples of π, the couplings are purely dissipative. Note that the decay parameter $\kappa_{\alpha\alpha} = \frac{g_\alpha^2 L}{v_g}$ deduced here accounts only for the waveguide's contribution to the dynamics. When other decohering channels are considered in parallel, additional dissipative

effects are tacked onto these terms.

APPENDIX B

ADIABATIC THEORY OF LEVEL ATTRACTION

To explain the physics of cavity-mediated level attraction, in the limit $\kappa \gg \gamma_i$ and $\kappa \gg g_i$, we employ an adiabatic model to advance an effective two-mode description for the magnon modes, since the cavity mode relaxes rapidly into its steady state [1]. This treatment reinforces forthwith the emergence of a dissipative interaction between the magnons in the adiabatic limit, which underpins the phenomenon of level attraction. In the rotating frame of the cavity mode, the mean field equations of the hybrid cavity magnon system are given by

$$\dot{X} = -i\mathscr{H} X, \tag{B.1}$$

In the adiabatic limit, we can eliminate the cavity mode by setting $\dot{a} = 0$, yielding

$$a = \frac{-i(g_1 m_1 + g_2 m_2)}{\kappa}. \tag{B.2}$$

Substituting this into Eq. (B.1), we obtain a coupled system of differential equations encompassing the dynamics of the magnon modes,

$$\dot{Y} = -i\tilde{\mathscr{H}} Y, \tag{B.3}$$

with $Y^T = [m_1\ m_2]$ and

$$\tilde{\mathscr{H}} = \begin{pmatrix} s - i\tilde{\gamma}_1 & \frac{-ig_1 g_2}{\kappa} \\ \frac{-ig_1 g_2}{\kappa} & -s - i\tilde{\gamma}_2 \end{pmatrix}, \tag{B.4}$$

[1] The derivation presented is reprinted with permission from *Cavity-mediated level attraction and repulsion between magnons* by J. M. P. Nair, D. Mukhopadhyay and G. S. Agarwal, Phys. Rev. B **105**, 214418 (2022), published by the American Physical Society.

where $\tilde{\gamma}_i = \gamma_i + \frac{g_i^2}{\kappa}$. For identical couplings $g_1 = g_2 = g$ and magnon relaxation rates $\gamma_1 = \gamma_2 = \gamma$, we can simplify $\tilde{\mathscr{H}}$ further into

$$\tilde{\mathscr{H}} = \begin{pmatrix} s - i(\gamma + \frac{g^2}{\kappa}) & \frac{-ig^2}{\kappa} \\ \frac{-ig^2}{\kappa} & -s - i(\gamma + \frac{g^2}{\kappa}) \end{pmatrix}. \tag{B.5}$$

The eigenvalues of the Hamiltonian are given by

$$\lambda_\pm = -i\left(\gamma + \frac{g^2}{\kappa}\right) \pm \sqrt{s^2 - (g^2/\kappa)^2}, \tag{B.6}$$

which bear the earmarks of level attraction, and also reproduce Eq. (8.6) in the limit of vanishingly small γ. For, $|s| \leq \frac{g^2}{\kappa}$, the real parts remain identical, yielding the phase transition points $s = \pm\frac{g^2}{\kappa}$. So it is no coincidence that we had observed the onset of mode coalescence at this exact same point in the preceding section. Thus, under the purview of the adiabatic approximation, in which the short-lived nature of the intracavity field mode is accounted for, the full tripartite system reduces to an effective two-mode subsystem with conformable properties in the linear response. The above matrix exactly replicates the effective Hamiltonian of a two-mode system with density matrix ρ, coupled through an interposing reservoir, and described by the master equation [77]

$$\frac{\mathrm{d}\rho}{\mathrm{d}t} = -\frac{i}{\hbar}[H, \rho] + \gamma_1 \mathscr{L}(m_1)\rho + \gamma_2 \mathscr{L}(m_2)\rho + 2\Gamma \mathscr{L}(c)\rho, \tag{B.7}$$

with $H = \Delta_1 m_1^\dagger m_1 + \Delta_2 m_2^\dagger m_2$, $\Gamma = g^2/\kappa$, $c = \frac{1}{\sqrt{2}}(m_1 + m_2)$, and the Liouvillian $\mathscr{L}$ is defined by $\mathscr{L}(\sigma)\rho = 2\sigma\rho\sigma^\dagger - \sigma^\dagger\sigma\rho - \rho\sigma^\dagger\sigma$. More precisely, the mean-field equations resulting from the above master equation are identical to Eq. (B.3). To put it into perspective, the cavity, when weakly coupled to the magnons, merely acts as a common reservoir for the magnon modes in the adiabatic limit, thereby precipitating in a dissipative form of interaction between them.